Sustainable New Energy Materials: Design and Discovery of Novel Materials and Architectures for Lithium Ion Batteries and Solar Energy Conversion

by

Qian Cheng

A Dissertation Presented in Partial Fulfillment
of the Requirements for the Degree
Doctor of Philosophy

Approved April 2016 by the
Graduate Supervisory Committee:

Candace K. Chan, Chair
Karl Sieradzki
Peter Crozier
Ximin He

ARIZONA STATE UNIVERSITY

August 2016

ABSTRACT

There is a fundamental attractiveness about harnessing renewable energy in an age when sustainability is an ethical norm. Lithium ion batteries and hydrogen fuels are considered the most promising energy source instead of fossil fuels. This work describes the investigation of new cathode materials and devices architectures for lithium ion batteries, and photocatalysts for their usage in water splitting and waste water treatment.

$LiCoO_2$ and $LiNi_{1/3}Mn_{1/3}Co_{1/3}O_2$ were exfoliated into nanosheets using electrochemical oxidation followed by intercalation of tetraethylammonium cations. The nanosheets were purified using dialysis and electrophoresis. The nanosheets were successfully restacked into functional cathode materials with microwave hydrothermal assistance, indicating that new cathodes can be obtained by reassembling nanosheets. This method can pave the way for the synthesis of materials with novel structures and electrochemical properties, as well as facilitate the fabrication of hybrid and composite structures from different nanosheets as building blocks.

Paper folding techniques are used in order to compact a Li-ion battery and increase its energy per footprint area. Full cells were prepared using $Li_4Ti_5O_{12}$ and $LiCoO_2$ powders deposited onto current collectors consisting of paper coated with carbon nanotubes. Folded cells showed higher areal capacities compared to the planar versions. Origami lithium-ion battery made in this method that can be deformed at an unprecedented high level, including folding, bending and twisting.

Spray pyrolysis was used to prepare films of $AgInS_2$ with and without Sn as an extrinsic dopant. The photoelectrochemical performance of these films was evaluated after annealing under a N_2 or S atmosphere with different amounts of the Sn dopant.

Density Function Theory (DFT) was used to calculate the band structure of $AgInS_2$ and understand the role of Sn doping in the observed properties.

Cr(VI) removal was investigated using multiple oxide photocatalyst and additives. The efficiency for Cr(VI) removal using these photocatalysts was investigated in synthetic neutral and alkaline water, as well as in cooling tower blowdown water. While sulfite alone can chemically reduce Cr(VI), sulfite in combination with a photocatalyst resulted in faster and complete removal of Cr(VI) in 10 min using a SO_3^{2-}/Cr(VI) ratio >35 in pH ~ 8 solutions.

ACKNOWLEDGMENTS

I would like to thank my advisor, Prof. Candace K. Chan, for her nice guidance and selfless help during my Ph.D career. To be honest, I would have struggled if anyone else were my advisor. I admire Candace's meticulousness, independence and endeavors, which were missing from my character before I was a Ph.D. student. It is she who taught me how to be a researcher. Her excellent writing skills have always promoted my manuscripts to a new level and benefited me a lot in improving my English. I feel lucky to be Candace's first Ph.D student. As she is a smart and diligent person, I am sure she will become a leading authority in the battery field.

I would like to thank my dissertation committee members, Prof. Karl Sieradzki, Prof. Peter Crozier, and Prof. Ximin He, for their valuable suggestion for my research and their generous time for my comprehensive exam and dissertation defense.

I would like to thank the Fulton Schools of Engineering, the Salt Research Project (SRP)/ASU Joint Research Program, and Arizona Board of Reagents for funding during my Ph.D. I would like to thank Prof. Xihong Peng for performing the DFT calculations in my $AgInS_2$ project (Part 6.3). I would like to thank Ting Yang for his help with TEM, Chengwei Wang for his help with BET, Man Li for her help with ICP-MS, Chengchen Guo for his help with Raman and Manpuneet Kaur with her help with AFM. I gratefully acknowledge the use of facilities within the LeRoy Eyring Center for Solid State Science, the Goldwater Environmental Laboratory at Arizona State University. I would like to thank Karl Weiss, David Wright, Diana Convey, Timothy Karcher and Kenneth Mossman, for their help with equipment training and sample tests. I would also like to

thank Xiangyu Bi, Kyle Doudrick and Prof. Paul Westerhoff for their help in the Cr(VI) reduction project.

I would like to thank my classmates and group members for their friendship, help, and support. It has been my pleasure to work with my group members: Ting Yang, Chengwei Wang, Ran Zhao, Man Li, and Dr. Ying Li. They helped me a lot on my research and made my time spent in the lab valuable. I would also like to thank my other ASU classmates: Yuanyu Ma, Minglu Liu, Xin Guan, Qiushi Mou, Ruohan Zhang, Chengchen Guo, Qing Chen, Qianlang Liu, Xiying Chen, Ke Geng, Shuoxing Jiang, Jie Ding, Shengke Zhang, Evan Chen, Jia Xu, Hongen Xie, Xinhao Zhao and Jing Lu, who helped me a lot and made my four years at ASU memorable.

Finally, I would like to express my most gratitude to my parents for their love and support. I also want to express my love to Shuwei who was constantly at my side no matter what happened. The best thing that ever happened to me was that I met you during my Ph.D time.

TABLE OF CONTENTS

Page

CHAPTER Page

CHAPTER Page

LIST OF TABLES

Table Page

LIST OF FIGURES

Figure Page

Figure Page

Figure Page

Figure Page

Figure Page

LIST OF PUBLICATIONS

CHAPTER 3

(1) Cheng, Q., Yang, T., Li, Y., Li, M., Chan, C. K. Oxidation–reduction assisted exfoliation of $LiCoO_2$ into nanosheets and reassembly into functional Li-ion battery cathodes, J. Mater. Chem. A 4, 6902-6910 (2016).

CHAPTER 5

(2) Cheng. Q, Song, Z., Ma, T., *et al.* Folding paper-based lithium-ion batteries for higher areal energy densities, Nano Letters. 13, 4969-4974 (2013).

CHAPTER 6

(3) Cheng, Q., Peng, X., Chan, C. K. Structural and photoelectrochemical evaluation of nanotextured Sn-Doped $AgInS_2$ films prepared by spray pyrolysis, ChemSusChem. 6 102-109 (2013).

CHAPTER 7

(4) Cheng, Q., Wang, C., Doudrick, K., Chan, C. K. Hexavalent chromium removal using metal oxide photocatalysts, Appl. Catal., B 176, 740-748 (2015).

1 INTRODUCTION TO THE BACKGROUND OF THE DISSERTATION

Energy is the driving force of human society, and thus the energy industry has the highest output value. We can say whoever controls the energy also controls wealth and power. Energy sources, such as electricity and petroleum, have very mature chains of production, transportation and usage.

Compared with fossil fuels, electricity is much cleaner during transport and usage. If the electricity comes from sustainable sources like solar, water, wind and nuclear power, there will be even fewer pollutants. Electricity is much easier to use but the disadvantage is very obvious: we cannot live off the grid! Nothing will work without a plug. Electricity is hard to be stored, and current chemical batteries are heavy and inefficient. There will be more challenges for batteries if electricity wants to take over the position of fossil fuels: higher capacities and fewer costs. Chapter 2 gives a brief introduction to lithium ion batteries and cathodes, exhibits the bottleneck of chemical batteries; Chapter 3 & 4 describe a new method that uses nanosheets to prepare and design new cathodes for lithium ion battery materials; Chapter 5 describes the preparation of new architectures of lithium ion batteries using to further improve the energy density. These two chapters study the possible methods that can overcome the bottleneck of energy density in lithium ion batteries. Overall, Chapter 3 & 4 study the design of new cathode materials and Chapter 5 provides a new architecture for lithium ion batteries. These three chapters provide a possibility to further improve energy density of lithium ion batteries from materials and structure.

Fossil fuels have been the most important energy sources. Energy is stored in the form of chemical energy in fossil fuels and can be released when the fuels are combusted in oxygen, which is everywhere in the air. Therefore the storage, transport and usage of fossil fuels are very convenient and reliable; most of vehicles rely on fossil fuels. The biggest challenge is the pollutant: the combustion of petroleum releases tons of CO_2 and to the atmosphere. Under the background that global warming has become the hot topic, it is the trend to reduce the burning of fossil fuels. Also, the reserves of fossil fuels are limited; there is an urgent need to find an alternative chemical fuel that is clean and renewable. Hydrogen is the perfect candidate: clean, renewable and high-energy-density:

$$H_2 + O_2 \xrightarrow{Combustion} H_2O \xrightarrow{Decomposition} H_2 + O_2$$

However, most of the industrially produced hydrogen comes out of the decomposition of fossil fuels, which makes the cleanliness of hydrogen meaningless. A clean, cheap and efficient method to make hydrogen out of water is very tempting: for example, photocatalytic water splitting that utilizes solar light to decompose water. Electron / hole pairs can be generated when photocatalyst is shined, and electrons have strong reducing powers that can reduce protons to hydrogen. Besides, photocatalysts can also be used to remove organic species / toxic metal ions in waste water due to their strong oxidizing/reducing powers. In Chapter 6, $AgInS_2$ and Sn-doped $AgInS_2$ were investigated as novel photoelectrodes with excellent visible-light absorbance. Their structural and photoelectrochemical properties were thoroughly studied. In Chapter 7, TiO_2, ZnO, WO_3, and $NaTaO_3$ photocatalysts were studied, and Cr(VI) ions were removed from both synthetic and cooling tower blowdown waters with photocatalysts. These results prove

that photocatalyst can not only be used to generate fuels, but be also used to purify polluted water. Chapter 6 & 7 prove the wide application of photocatalyst on clean energy conversion and environment protection.

From the above, it is very clear that both hydrogen fuels and batteries are important replenishments to existing energy industry and future energy industry. Energy conversion, clean energy and environmental protection will always be important areas and need endeavors from millions of talented people.

2 INTRODUCTION TO BATTERIES

2.1 Introduction to Lithium Ion Batteries

Batteries are devices that can convert chemical energy to electrical energy and have a history of nearly 2000 years. Pb-acid batteries, Ni-Cd batteries, Ni-H batteries and Lithium ion batteries have been commercialized and used in all aspects of human life. Batteries can be classified as primary batteries (disposable batteries) and secondary batteries (rechargeable batteries). The comparison of the energy density of all kinds of batteries on is listed in Figure 2.1. With the rapid development of electronics, lithium ion secondary batteries have already been widely used in mobile devices and electrical cars due to better cycling capability, higher operating voltage and energy density compared to other types of batteries.

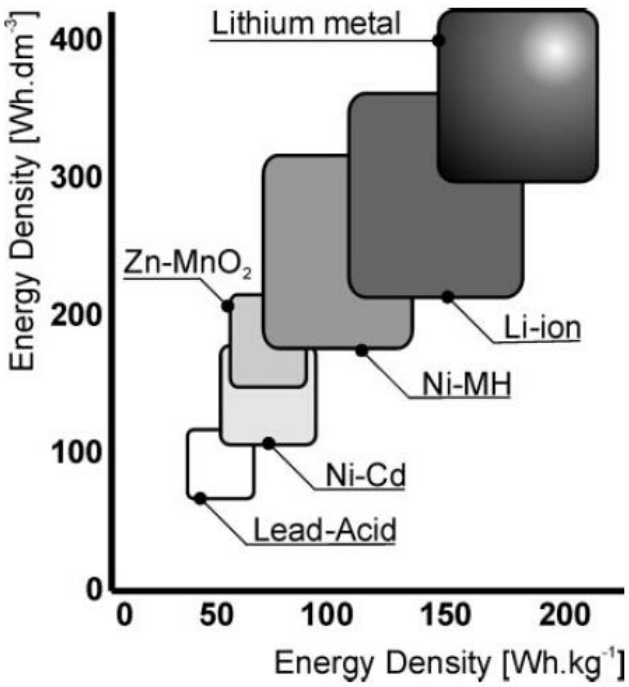

Figure 2.1 Comparison of different batteries on energy density. [1]

Why do lithium ion batteries have these merits over the others? It should be discussed from how to design a battery. A battery has an anode and a cathode, corresponding to reductant and oxidant respectively. The electrons will flow from anode to cathode through outside circuits and the same with cations inside the battery due to the chemical potential. The energy density of a battery depends on the Gibbs free energy changed / total mass or volume during the oxidation-reduction reactions in the battery.[2] Table 2.1 lists all metal elements that can be used as an anode.[3] Lithium is the lightest metal (Atomic Weight 6.94) and strongest reducer (-3.04 V vs NHE).[4] Lithium ions also have a small radius which is beneficial for insertion reactions and display good solubility as salts. These unique properties make lithium the first choice to make a battery.

Table 2.1 Characteristics of common metal anodes.

Metal	Atomic Weight	Standard Potential (V vs NHE)	Density (g/cm^3)	Energy Density (Ah/g)
Li	6.94	-3.04	0.534	3.86
Na	23.0	-2.7	0.97	1.16
Mg	24.3	-2.4	1.74	2.2
Al	26.9	-1.7	2.7	2.98
Ca	40.1	-2.87	1.54	1.34
Fe	55.8	-0.44	7.85	0.96
Zn	65.4	-0.76	7.13	0.82
Cd	112	-0.4	8.65	0.48
Pb	207	-0.13	11.35	0.26

Early batteries that used lithium metal as the anode are called lithium batteries. One of the first lithium batteries used TiS_2 as the cathode. The overall reaction is listed below:[5]

$$xLi + TiS_2 \rightleftharpoons Li_xTiS_2 \tag{2.1}$$

TiS_2 adopts hexagonal close packing and has a layered structure. Each layer comprises Ti-S octahedra with Ti in the center and six sulfur ligands at the apex. Similar with graphite, the atoms in the sheets are bonded with strong covalent bonds; then these sheets are bonded to each other through van der Waals forces.[6] In the electrochemical reaction, lithium intercalates into the interlayer space during charging.[7] The voltage of the battery is around 1-1.5 V vs Li/Li^+. However, lithium batteries failed to be commercialized during the 1960s due to safety issues. The surface of lithium metal was not uniform, the uneven current distributions led to the anisotropic growth of lithium during charging and the formation of lithium dendrites.[8] These dendrites would keep growing during cycling until they broke and lost electrical contact with the current collector, inducing the loss of active lithium ions which means the generation of irreversible capacity. Besides capacity loss, lithium dendrites can also pierce the separator and form a short circuit between the anode and cathode, which resulting in a serious safety issue.[9] Lithium is very reactive with water. Instead of using aqueous electrolyte, the usage of organic electrolyte in lithium batteries is another safety problem.

The study of lithium ion batteries originates from lithium batteries in order to solve these safety problems brought on by use of the lithium metal anode. Since the problem with lithium anodes is the growth of lithium dendrites, it is better to build “hosts” for

lithium ions to avoid its random deposition. Layered materials, such as graphite and TiS_2, are perfect candidates for this purpose. The interlayer space in these materials provides such "hosts", which allow lithium ions to intercalate into designated sites to avoid dendrite formation at the surface of anode. If layered materials are used as both cathode and anode, lithium would exist in the electrode materials in the form of ions rather than its metallic form, which is why this configuration is known as a lithium ion battery.[4] The depiction of a lithium battery and lithium ion battery are shown in Figure 2.2.

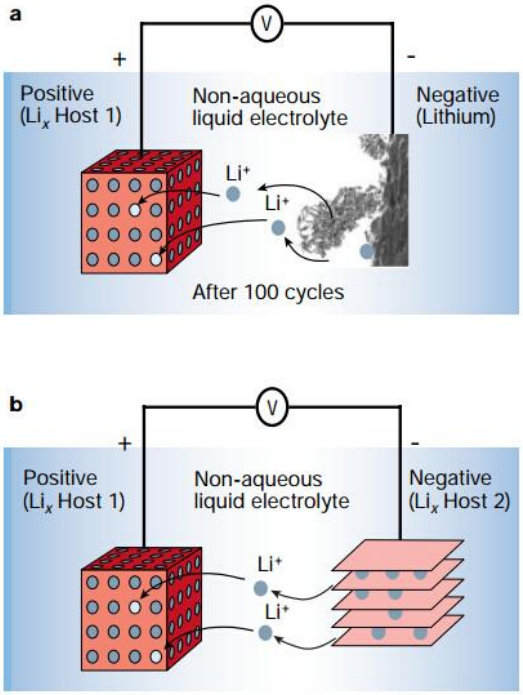

Figure 2.2 Mechanism of (a) lithium battery and (b) lithium ion battery.[4]

In most lithium ion batteries, graphite is utilized to replace Li metal as anode. Graphite has a layered structure and can form intercalation compounds (LiC_6) with lithium to avoid the growth of dendrite.[10] Compared to lithium metal, graphite is cheap, nontoxic, and stable in the air. These advantages can greatly reduce the manufacturing costs of

these batteries. Although the potential plateau of graphite at about 0.5 V vs Li/Li^+ means some loss in voltage, the capacity (372 mAh/g), less reaction with electrolyte, lower costs and better safety enable its wide application instead of lithium metal.[10]

Since graphite cannot provide lithium ions, the cathode must be composed of pre-lithiated materials to provide lithium ions. The cathode also must be a strong oxidant to provide a high voltage. The structure must also be stable to allow the intercalation of lithium ions. Disulfide materials were abandoned because they are incapable of providing enough voltage. According to these requirements, the transition metal oxide $LiCoO_2$ first proposed by Goodenough[11] was used as cathode. $LiCoO_2$ also has a hexagonal close packing structure. The "hosts" are CoO_2 layers and lithium ions can go in and out through 2D tunnels in the interlayer space. The transition metal redox Co^{3+}/Co^{4+} enables its high operating voltage. The battery reactions are:

Positive electrode:

$$LiCoO_2 \underset{Discharging}{\overset{Charging}{\rightleftharpoons}} Li_{1-x}CoO_2 + xLi^+ + xe^- \tag{2.2}$$

Negative electrode:

$$6C + xLi^+ + xe^- \underset{Discharging}{\overset{Charging}{\rightleftharpoons}} Li_xC_6 \tag{2.3}$$

The overall reaction is:

$$6C + LiCoO_2 \underset{Discharging}{\overset{Charging}{\rightleftharpoons}} Li_{1-x}CoO_2 + Li_xC_6 \tag{2.4}$$

For both cathode and anode, lithium can intercalate and de-intercalate into the "hosts". Lithium ions "shuttle" between cathode and anode during charging and discharging. Therefore, lithium ion batteries are also called "rocking chair batteries".

2.2 Introduction to Layered Cathode Materials for Lithium Ion Batteries

2.2.1 Design Criteria of Cathode Materials

Nowadays, anodes for lithium ion batteries have achieved a lot of progress; the development of graphite, [12] silicon nanowires, [13] Sn nanoparticles, [14] and even lithium[15] anodes that have shown high capacity and good cycling capability. Compared to high-performance anodes that have capacity higher than 1000 mAh/g, cathodes, which only display capacities around 150 mAh/g, are becoming the bottleneck of lithium ion batteries. Therefore, chasing higher energy densities for cathodes is the highest priority right now.

Layered transition metal oxides are most widely used in the battery market. As mentioned above, (1) they have "hosts" and "tunnels" into which lithium ions can intercalate and de-intercalate; and (2) they are stable at high operating voltages. Compared with sulfides, metal oxides are more stable due to stronger ionic bonding; (3) they are lighter due to the lower atomic weight of oxygen; (4) the presence of transition metals establishes their strong oxidizing power. During lithiation and delithiation, transition metal ions can acquire and lose electrons respectively to provide electro-neutrality and protect the stability of the structure. The suitable transition metals include V, Fe, Mn, Ni and Co. (5) the utilization of graphite as anode requires the cathode to be prelithiated. In these metal oxides, $LiCoO_2$, $LiMnO_2$ and $LiNiO_2$ have close-packing hexagonal layered structures and can form solid solutions with each other as shown in Figure 2.3.[16] Compared with other cathodes, they have better conductivity, cycling ability and are easy to be synthesized. Therefore they are the most widely studied and used cathode materials.

Table 2.2 The theoretical and actual capacities of common layered cathode materials.

Compound	Theoretical capacity (mAh/g)	Actual capacity (mAh/g)	Operating voltage (V vs. Li/Li^+)
$LiCoO_2$[17]	274	140	2.5-4.2
$LiMnO_2$[18]	286	200	3.4-4.3
$LiNiO_2$[19]	274	152	2.5-4.2
$LiNi_{1/3}Co_{1/3}Mn_{1/3}O_2$[20]	277	150	2.5-4.3

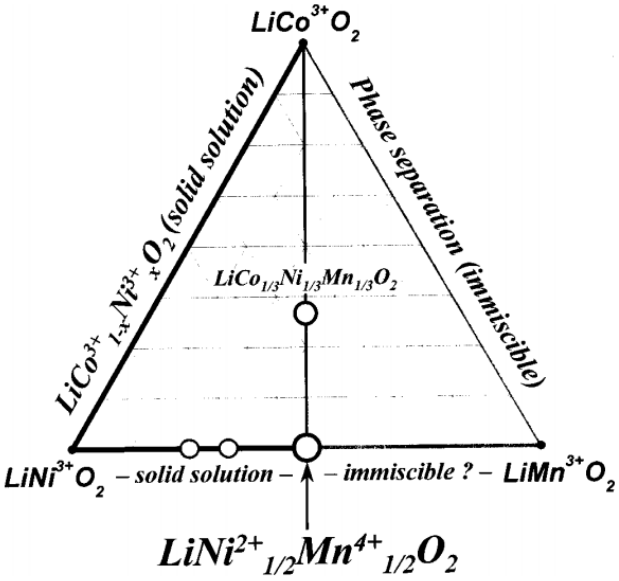

Figure 2.3 Phase triangle of $LiCoO_2$, $LiMnO_2$ and $LiNiO_2$.

Although the theoretical capacities of these layered materials are quite high (Table 2.2, ~274 mAh/g), overcharging (E > 4.3 V) would cause the lattice to collapse and lead to cycling failure. Thus, the actual capacity is limited to only half of the theoretical one. Other cathode materials that do not have layered structures have different issues. Spinel

structure materials such as $LiMn_2O_4$[21] and $LiNi_{0.5}Mn_{1.5}O_4$[22] have limited pre-inserted lithium; therefore their theoretical capacities (140 mAh/g) are only half of the ones of $LiMO_2$; polyanion compounds such as $LiMPO_4$ (M=Co, Fe, Mn, V) can be fully de-intercalated, but have smaller theoretical capacities (160 mAh/g).[23] Their rate performance and particle sizes are limited due to their poor electrical and ionic conductivity.[24] It worth noticing that these materials have limitations on either theoretical capacity or operating voltage, which directly determines the energy density of the battery. Materials with high theoretical capacities and stability at high operating voltage should be the focus of the development of next generation cathodes.

2.2.2 $LiCoO_2$ as Cathode Material

$LiCoO_2$ is one of the earliest cathode materials studied by Goodenough.[11] It has an $R\bar{3}m$ structure with a lattice constant of a = 2.816 Å and c = 14.051 Å.[25] Li, Co and O alternatively occupy the (111) layer of octahedral sites. Li^+ (3a) and Co^{3+} (3b) alternatively arrange on the O facet. The Co^{3+} and O^{2-} have a strong chemical bond and are close to each other; thus they are treated as cobalt oxide octahedral that form layers that are bonded to each other through electrostatic interactions from Li^+ (Figure 2.4). During electrochemical cycling, the cobalt oxide layers function as an intact framework and the lithium ions can intercalate in and out of the 2D interlayer space.[26]

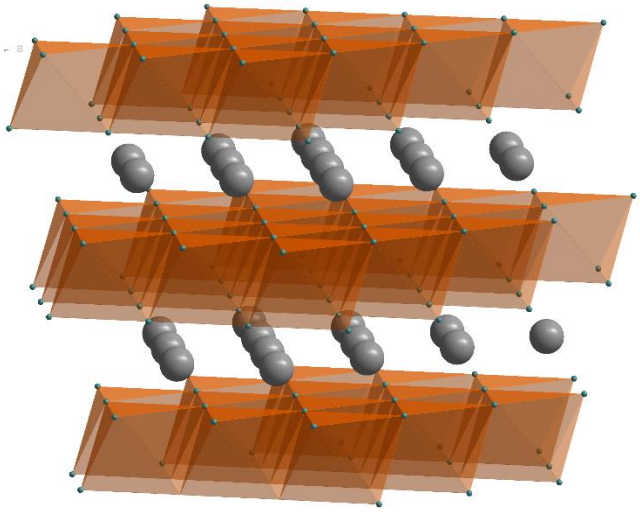

Figure 2.4 Hexagonal structure of $LiCoO_2$.

The reaction of $LiCoO_2$ during electrochemical cycling is:

$$LiCoO_2 \underset{Discharging}{\overset{Charging}{\rightleftharpoons}} Li_{1-x}CoO_2 + xLi^+ + xe^- \qquad (2.2)$$

The theoretical capacity can be calculated as:

$$C_G = \frac{(1000)xF}{(3600)M} = \frac{(1000)(1)(9.6485\ x\ 10^4)}{(3600)(97.87)} = 273.84 \text{ mAh/g}$$

Where x is the number of lithium ions that can be de-intercalated from the structure, F is Faraday's constant, and M is the molecular weight of $LiCoO_2$. In Li_xCoO_2, x is directly related to the charging voltage as shown in Figure 2.5. The end member, CoO_2, is possible when the charging voltage vs. Li/Li^+ reaches 5.2 V, which corresponds to a capacity of 274 mAh/g.[27] However, lithium ions in layered structures are more than just shuttling ions; they are also the pillars that maintain the stability of whole framework. Therefore, $LiCoO_2$ can only have half of the lithium removed to avoid the damage of framework. During charging, the crystalline phase of $LiCoO_2$ changes from hexagonal phase to monoclinic around 4.2 V followed by the expansion of the c-axis. When the

voltage is higher than 4.2V, it will continue to transfer from monoclinic (M1) to hexagonal (H2) and the c-axis spacing starts to decrease. This process is shown in Figure 2.5[1] and Figure 2.6.[27] The phase changes induce the fluctuation of the c-axis interlayer spacing, which is directly related to the loss of cobalt caused by the attack from HF (coming from electrolyte) as shown in Figure 2.7.[28]

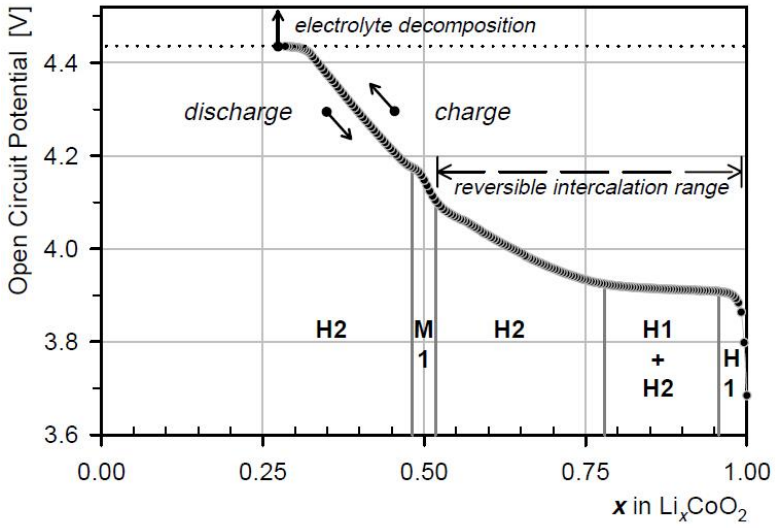

Figure 2.5 Phase transformations of Li_xCoO_2 during electrochemical charging.[1]

The structural changes that occur during the lithiation/delithiation of $LiCoO_2$ induce internal stresses that can lead to the collapse of the active matrix. For metal oxides, the elastic strain must be lower than 0.1%,[29] otherwise fracture can happen. The increased cutoff voltage results in more fluctuation in the c-axis and increase of cobalt loss, which all bring the quick capacity fade during cycling[27, 28]. Therefore, the traditional safe cycling voltage region for $LiCoO_2$ is limited to 2.5 V to 4.3 V vs. Li/Li^+. In this voltage region, the achievable capacity is around 135 mAh/g, which corresponds to x = 0.5. Thus, the actual capacity attained using $LiCoO_2$ is only half of the theoretical one where all of

the Li are removed. The same phenomena also happens in $LiNiO_2$ and $LiMnO_2$ which share same structure with $LiCoO_2$.

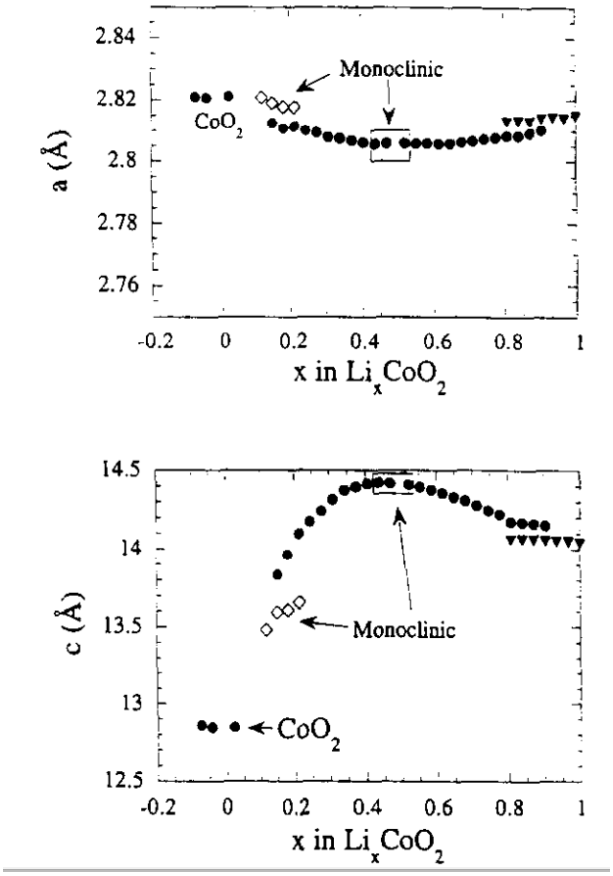

Figure 2.6 The parameter of c-axis changes as the extraction of Li ions from $LiCoO_2$.

From the statements above, it can be clearly seen that $LiCoO_2$ is very sensitive to high voltages. The cutoff voltage determines the fraction of lithium ions that can be extracted. The higher the cutoff voltage, the higher the capacity we can get from $LiCoO_2$. The highest voltage that $LiCoO_2$ can reach without affecting capacity retention is 4.35 V. This highly limits the further improvement of energy density in $LiCoO_2$. To protect the stability of $LiCoO_2$, one of the solutions is to coat stable metal-oxide layers on $LiCoO_2$.

The coating of Al_2O_3 on $LiCoO_2$ can inhibit phase transitions; thus the Al_2O_3-coated $LiCoO_2$ displayed 97% capacity retention after 50 cycles (Figure 2.8); [30]. Other metal oxide coatings such as SnO_2,[31] ZrO_2 and TiO_2[32] have been shown to stabilize $LiCoO_2$ as well. Through coating, Co loss from the attack of HF which comes from decomposition of $LiPF_6$ can be avoided.[32] But these methods cannot solve the problems of $LiCoO_2$ thoroughly. After development for 20 years, $LiCoO_2$ has reached its limits on cathode density. Further improvement should be focused on the inhibition of phase changes at higher voltages. Only higher capacity brought on by higher cutoff voltage can lead to improvements in the energy density of $LiCoO_2$.

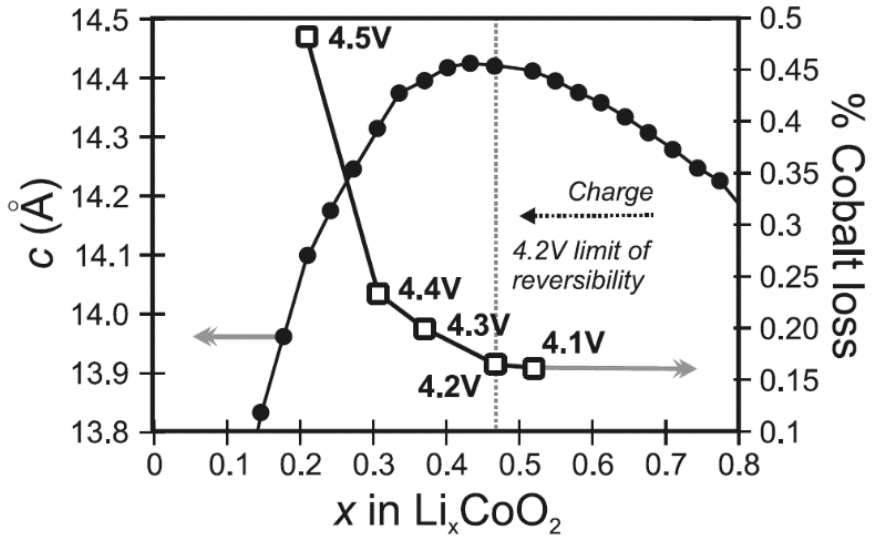

Figure 2.7 The connection between Co loss and cut-off voltage.

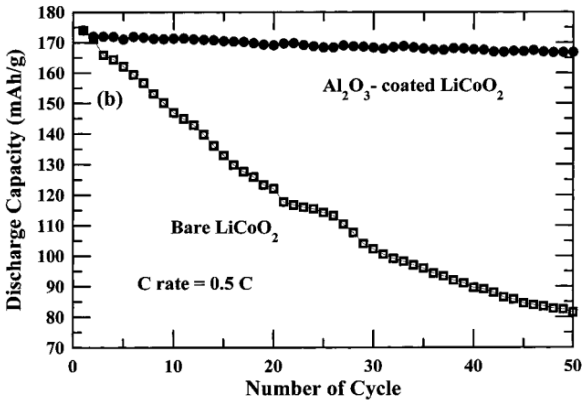

Figure 2.8 Capacity retention of $LiCoO_2$ at voltage cycling window from 2.75 V to 4.4 V.

2.2.3. $LiCo_{1/3}Mn_{1/3}Ni_{1/3}O_2$ as Cathode Material

Although $LiCoO_2$ was the first choice and most widely used cathode for commerical lithium ion batteries, the disadvantages are very obvious. (1) Co is toxic and expensive; (2) $LiCoO_2$ is very sensitive to high voltages (also known as overcharging); (3) its cycling performance is also not ideal. The other two materials, $LiMnO_2$ and $LiNiO_2$, with rock-salt structures have certain problems. In $LiMnO_2$ Mn has a very strong Jahn-teller effect and the structure can very easily change during cycling. Besides that, $LiMnO_2$ is very hard to synthesize. In order to obtain $LiMnO_2$ with rock salt structure, it must be synthesized through ion-exchange from $NaMnO_2$ with lithium salts.[18] For $LiNiO_2$, the similar ionic radius of Li and Ni makes it very hard to get stoichiometric $LiNiO_2$; Ni atoms have a very high probability to exist in the Li layer and Li atoms can also reside in the Ni layers; this is known as Li/Ni cation disorder, which introduces bad cycling performance.[33]

Table 2.3 Unit cell parameters of $LiMO_2$ (M=Co, Mn and Ni)

Material	a / Å
$LiCoO_2$[27]	2.816
$LiMnO_2$[18]	2.809
$LiNiO_2$[19]	2.88

The same $R\bar{3}m$ layered structure and similar unit cell parameters of these three materials (Table 2.3) make it very easy to form solid solutions, $LiNi_xCo_yMn_{1-x-y}O_2$ (Figure 2.9). The replacement of Co with Ni and Mn is very interesting due to its lower costs and toxicity.

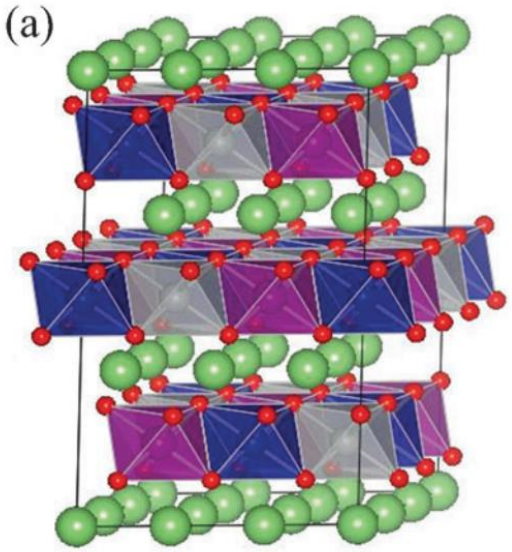

Figure 2.9 The structure of $LiNi_{1/3}Co_{1/3}Mn_{1/3}O_2$, different colors of octahedra show different cations (Mn, Co or Ni).[34]

In $LiNi_xCo_yMn_{1-x-y}O_2$, the valence of Ni, Co and Mn are +2, +3 and +4 respectively; the oxidation state of Co is same with the one in $LiCoO_2$, but the Ni and Mn are very different from what is found in $LiNiO_2$ and $LiMnO_2$;.[35] The Ni^{2+} can be oxidized to Ni^{4+} and the Ni^{2+}/Ni^{4+} redox is the major capacity source of $LiNi_xCo_yMn_{1-x-y}O_2$. Take $Li_aNi_{1/3}Co_{1/3}Mn_{1/3}O_2$ as an example, when $2/3 < a < 1$, $1/3 < a < 2/3$ and $0 < a < 1/3$, the reacting redox in $Li_aNi_{1/3}Co_{1/3}Mn_{1/3}O_2$ are Ni^{2+}/Ni^{3+}, Ni^{3+}/Ni^{4+} and Co^{3+}/Co^{4+} respectively.[35] $Ni^{2+/4+}$ can provide more Lithium sites than $Co^{3+/4+}$. Therefore the increase of Ni ratio would improve the capacity of cathode materials. However, as mentioned above, the Ni^{2+} ion (0.86 Å) has a similar ionic radius with Li^+(0.9 Å). Hence a high ratio of Ni would induce large Li/Ni disorder, which is responsible for the poor cycling ability of high content Ni materials.[35] There have been reports that the presence of Co would inhibit the migration of Ni from the transition metal layers to the Li layers.[36] This means that Co can be used to stabilize the structure by reducing cation disorder, which is good for cycling. The Mn octahedra provide the structural framework. The +4 valence of Mn indicates that Mn would not experience valence change and would be electrochemically inactive. $LiNi_xCo_yMn_{1-x-y}O_2$ materials have different properties depending on the ratio of Ni, Co, Mn. (Figure 2.10) The most common materials are $LiNi_{1/3}Co_{1/3}Mn_{1/3}O_2$ and $LiNi_{0.5}Co_{0.2}Mn_{0.3}O_2$ which are known as 111 and 523 materials, respectively.

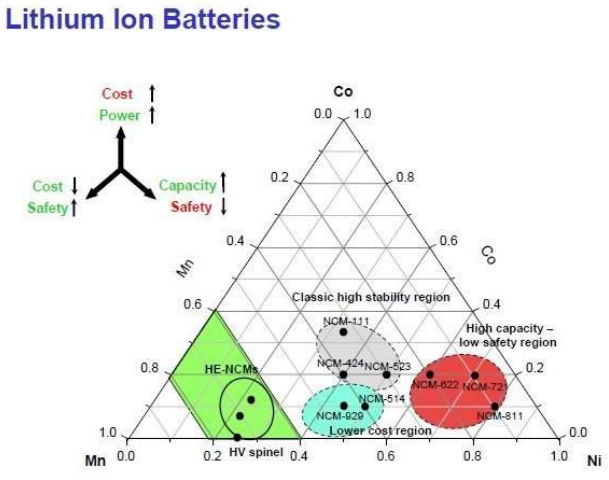

Figure 2.10 The effect of ratio of Ni, Mn and Co in $LiNi_xCo_yMn_{1-x-y}O_2$ solid solution (Source: Argonne National Lab DOE report).

523 materials have higher capacity in the normal cycling region due to the higher content of Ni;[37] 111 materials have better rate and cycling capability due to a more balanced ratio. Its capacity can reach 150 mAh/g in the voltage window from 2.5 to 4.3 V and can cycle at a higher cutoff voltage without phase change (up to 4.5 V).[35] The observed capacity and capacity retention of $LiNi_{1/3}Co_{1/3}Mn_{1/3}O_2$ at different cutoff voltages are shown in Figure 2.11. Compared to pristine $LiCoO_2$ (Figure 2.8), the cycling capability of $LiNi_{1/3}Co_{1/3}Mn_{1/3}O_2$ is greatly improved. However, when the cut-off voltage is higher, the capacity still decays very fast. The reason for this failure is similar to that of $LiCoO_2$, such as phase change, transition metal ion dissolution, and increased surface reactivity of cathode with electrolyte at higher voltage.[38] Coatings such as TiO_2,[39] carbon[40] and AlF_3[38] have been shown to effectively improve the cycling at high cut-off voltages.

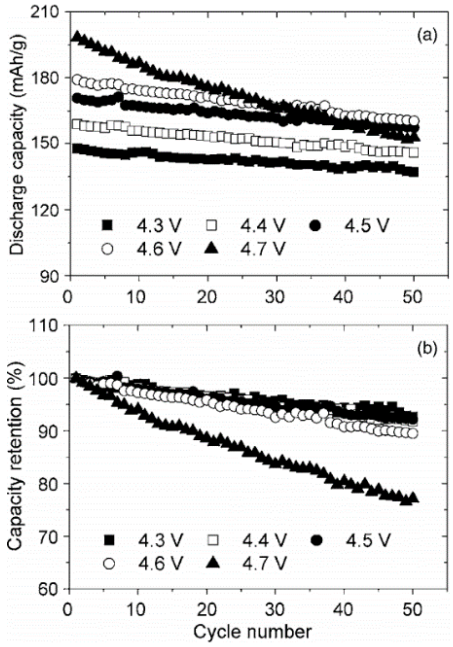

Figure 2.11 The cycling results of $LiNi_{1/3}Co_{1/3}Mn_{1/3}O_2$ under different cut-off voltages. (A) capacities under different cut-off voltages; (B) capacity retention at different cycle number.[34]

In order to make solid solutions of these three oxides, the most common method is co-precipitation of Mn^{2+}, Ni^{2+} and Co^{2+} to get hydroxide/carbonate precipitates of these three elements evenly distributed. Traditional sol-gel synthesis can also be used to prepare the precursor, with $Co(Ac)_2$, $Mn(Ac)_2$ and $Ni(Ac)_2$ as starting materials coordinated with citrate acid.[35] Then these precursors were mixed with $LiOH/Li_2CO_3$ and sintered at 800-900 ^oC.[41]

2.2.4. $xLi_2MnO_3*(1-x)LiCo_{1/3}Mn_{1/3}Ni_{1/3}O_2$ - Li Excess Materials

According to previous statements, there are two methods to improve the energy density of lithium ion battery cathodes: improving its operating voltage or increase its capacity. Development of high voltage materials, also known as 5 V materials, including $LiMPO_4$

(M = Co or Ni), $LiNi_{0.5}Mn_{1.5}O_2$ and $xLi_2MnO_3*(1-x)\ LiCo_{1/3}Mn_{1/3}Ni_{1/3}O_2$ as shown in Figure 2.12[42], is one of the trends for new cathode materials.

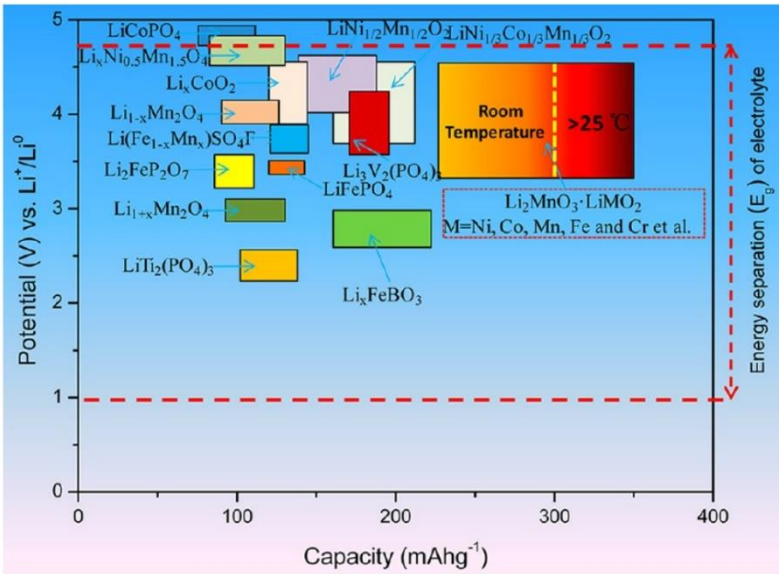

Figure 2.12 Capacities and operating voltages of various cathode materials.

$xLi_2MnO_3*(1-x)LiCo_{1/3}Mn_{1/3}Ni_{1/3}O_2$, also known as a Li excess material, has attracted a lot of attention due to its stability at high voltage and high capacity. $xLi_2MnO_3*(1-x)LiMO_2$ (M = Co, Mn, Ni or their combination) has a very complex structure, but it can be taken as solid solution of Li_2MnO_3 and $LiMO_2$ (M= Co, Mn, or Ni) (Figure 2.13).[43] Li_2MnO_3 also has a rock salt structure and belongs to the C2/m space group.[44] As shown in the figure, Li_2MnO_3 and $LiMO_2$ have a very similar structure. The difference is that in Li_2MnO_3, the M Layer comprises both Li and Mn octahedra which are alternatively arranged. The ratio of Li and Mn is 1:2. Therefore Li_2MnO_3 can also be written as $Li(Li_{1/3}Mn_{2/3})O_2$. Mn has a fixed valence of +4; thus it was first considered to be as inactive component.

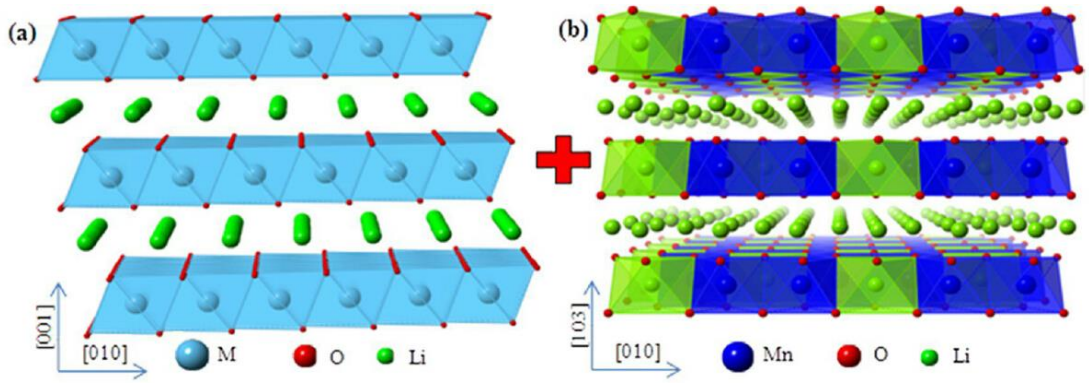

Figure 2.13 Crystal structure of Li_2MnO_3 and $LiMO_2$ (M= Co, Mn, or Ni).

This Li-excess layered materials have a theoretical capacity higher than 300 mAh/g and the actual capacity can reach as high as 300 mAh/g.[42] Therefore, Li-excess materials are considered the next generation of cathode materials. The stability of these materials originate from Li_2MnO_3. In Li_2MnO_3, all of the Mn are +4; therefore the unit cell distortion brought by the Jahn-Teller effect is weakened and the crystal structure can be better maintained. When the charging voltage is below 4.5 V, the Li^+ in $LiMO_2$ de-intercalate first. As the charging voltage increases to 4.5 V, Li ions start to de-intercalate from the Mn layer to the Li layer in Li_2MnO_3 and contribute a large charge plateau until the material transforms to MnO_2. The product at the final voltage (4.8 V) is $xMnO_2*(1-x)MO_2$, which has strong oxidizing ability.[42] From Li_2MnO_3 to MnO_2, there are 2 Li ions and one O lost during the charging process. The O is released in the form of O_2 from the surface of electrode. At the same time, oxygen rearrangement in the material occurs.[45] The release of O_2 can cause pressure buildup in the battery, which causes serious safety issues.

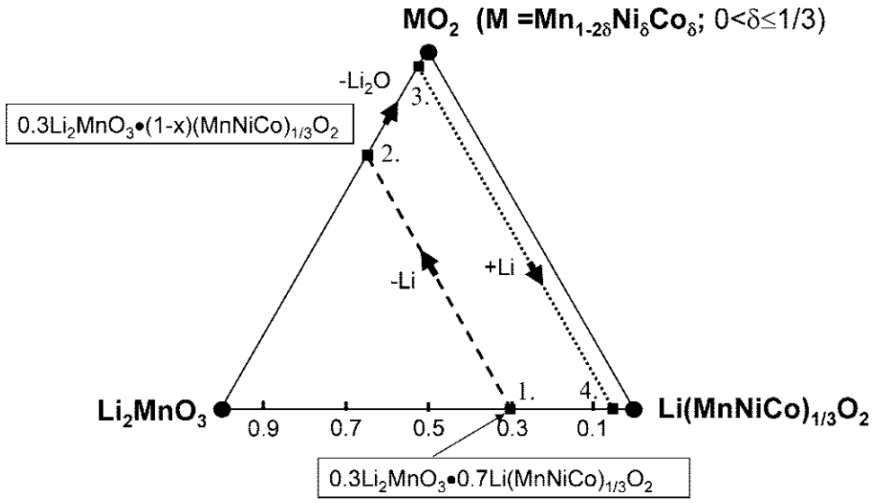

Figure 2.14 Phase diagram of Li_2MnO^3, $LiCo_{1/3}Mn_{1/3}Ni_{1/3}O_2$ and MO_2 (M=Ni, Mn, or Co)[46]

During discharging, only one lithium can be inserted back to the frame. The cycling process is: $xLi_2MnO_3*(1-x)LiMO_2$ →(charging)→ $xMnO_2*(1-x)MO_2$ →(discharging)→ $xLiMnO_2*(1-x)LiMO_2$. The phase diagram of Li_2MnO_3, $LiMn_{1/3}Ni_{1/3}Co_{1/3}O_2$ and MO_2 is shown in Figure 2.14. The major structural rearrangement and O_2 loss leads to the high irreversible capacity in the first cycle.[42] This problem is the intrinsic property of this material, which is hard to overcome. However, recent studies show that coating Li rich materials with TiO_2,[47] Al_2O_3,[47] and AlF_3[48] is effective for improving the Coulombic efficiency of the first cycle and exhibiting higher discharging capacities.

The oxygen release and rearrangement in the first cycle affect the performance of Li excess materials. One strategy is to remove Li_2O from Li_2MnO_3 in advance. There is research showing that Li-excess materials can be pretreated with acid to remove Li_2O to activate Li_2MnO_3; thus it can avoid the large irreversible capacity and release of

oxygen.[49] However, this method introduces H^+ into the structure, which is extremely harmful. The results showed that the cycling of acid-treated materials was much worse than the one without acid treatment. Pre-cycling of Li-excess materials at different voltages is another effective method to improve the cycling.[50]

It was also shown that mixtures of Li_2MnO_3 and $LiCoO_2$ milled in a planetary mill using acetone as solvent can result in the formation of solid solutions of Li_2MnO_3 and $LiCoO_2$ which can cycle up to 4.6 V. TEM characterization showed that there are grains of both Li_2MnO_3 and $LiCoO_2$ grains in the acquired samples, which prove that Li_2MnO_3 can effectively stabilize the layered structure.[51] Therefore, a composite cathode may bring breakthroughs on the capacity retention at higher voltages.

From previous statements, we know that one of the major problems of lithium ion batteries is the low energy density of the cathode. In order to further improve the energy density, it is important to enable the cycling ability of these materials at high operating voltages, but most of cathode materials do not have this property. The appearance of Li-rich materials, $xLi_2MnO_3*(1-x)LiMO_2$, brings hope to solve this problem. Its cycling window can be as large as between 2.0 V and 4.8 V; it also have an actual capacity as high as 300 mAh/g. However, there are still certain problems for this material:

First, Li_2O is released from the Li-rich material in the first charging cycle, which would result in a great amount of irreversible charging capacity. The irreversible capacity of cathode materials may not be a problem in full cell batteries, since anodes always consume Li from the cathode to form solid-electrolyte interface (SEI) films. However, the release of oxygen can cause the reconstruction of oxygen packing in the framework, which can cause structural changes that are harmful for cycling.

Second, the released O_2 would cause pressure build up in battery, which would cause safety problems.

Third, most of the capacity of this material is acquired at low voltages. Due to the high content of Mn, which has two potential plateaus at 3 V (Mn^{2+}/Mn^{3+}) and 3.5 V (Mn^{3+}/Mn^{4+}), the improvement of overall energy density is still limited.

Fourth, the terrible conductivity of Li_2MnO_3 inhibits the further use of Li-rich materials at higher rates.

3 EXFOLIATION AND REASSEMBLY OF $LiCoO_2$ 2D NANOSHEETS

3.1 How to Create New High-Performance Cathode Materials?

Since many conventional Li-ion battery materials have layered structures, they can, in theory, also be exfoliated into 2D nanosheets. The high surface area and short ionic diffusion distances in 2D nanosheets may improve the charging/discharging rates and result in higher capacities for Li^+ insertion.[52] Furthermore, hybrid electrode materials may be possible by reassembling different types of nanosheets, which can open the door to materials with unique voltage-dependent behavior, novel phase transformations, or new Li^+ insertion sites.[53] Such strategies may lead to improvements in cathode charge storage capacities, the major bottleneck in the development of higher energy density Li-ion batteries. However, the synthesis of layered lithium compounds into 2D nanosheet morphologies is challenging due to the strong interlayer electrostatic interactions in these materials. Previous studies have shown that the Li^+ in $LiCoO_2$, a Li-ion battery cathode material, cannot be exchanged directly with tetraalkylammonium cations.[54, 55] Hence, in order to obtain exfoliation through osmotic swelling, the interlayer Li^+ must be first ion-

exchanged with protons. However, the irreversible binding of protons or the formation of hydrated phases can have detrimental effects on the electrochemical properties of the materials when used in Li-ion batteries. This was previously demonstrated in layered cobaltates, whereby the desired cathode material $LiCoO_2$ was not obtained, but rather the protonated forms $HCoO_2$[55] and H_xLiCoO_2[54]. As a result, the obtained discharge capacities were lower than expected. Hydrated phases were also observed in MnO_2,[56] $Li[Mn_{1/3}Co_{1/3}Ni_{1/3}]O_2$,[57] and Na_xCoO_2[58, 59] materials obtained by exfoliation and restacking.

Inspired by the structure of $xLi_2MnO_3*(1-x)LiMO_2$, we want to design a new super lattice structure with different cathode layered materials. These sandwich structures can potentially result in unique synergistic effects and novel redox behavior due to the interactions from different sheets. Our aim is the super lattice structure with alternative $LiCoO_2$ layers and $LiCo_{1/3}Mn_{1/3}Ni_{1/3}O_2$ layers for the following reasons:

First, cobalt is much more stable in an octahedral arrangement than Mn. The electron configurations for Co and Mn are [Ar] $3d^74s^2$ and [Ar] $3d^54s^2$, respectively. For Mn, the 5 d-electron orbitals are divided to 2 separate energies under the effect of ligands; 3 orbitals have lower degenerate energy which is known as t_{2g}, and the other 2 orbitals have higher energy which is known as e_g. When going from Mn^{4+} to Mn^{3+}, the electron configuration go from t_{2g}^3 to $t_{2g}^3e_g^1$, which is the configuration affected most by the Jahn-Teller effect. One of the biggest problems of Li-rich materials is the bad cycling brought on by the phase transformation of MnO_2 from a layered structure to a spinel structure.[60] When going from Co^{4+} to Co^{3+}, the electron configuration changes from $t_{2g}^3e_g^2$ to t_{2g}^6. Therefore,

Co has a much lower Jahn-Teller effect than Mn. Therefore, Co octahedra should be more stable than the one of Mn.

Second, Co has a higher oxidizing power than Mn. The redox couple of Co^{4+}/Co^{3+} is at 3.9 V vs Li/Li^{+}, which means it can deliver more capacity at higher operating voltages, and thus higher energy density.

Third, the restacking of different nanosheets can circumvent the release of Li_2O from Li_2MnO_3, but can still get a structure of $LiCoO_2$ * $LiCo_{1/3}Mn_{1/3}Ni_{1/3}O_2$ which is similar with $xLiMnO_2*(1-x)LiMO_2$ (after 1st cycle).

However, it is hard to get a super-lattice structure with $LiCoO_2$ and $LiCo_{1/3}Mn_{1/3}Ni_{1/3}O_2$ using traditional synthesis methods. With methods such as solid state or sol-gel synthesis, the most likely product would be $LiCo_{2/3}Mn_{1/6}Ni_{1/6}O_2$, not a material with a sandwich structure comprising alternating layers of $LiCoO_2$ and $LiCo_{1/3}Mn_{1/3}Ni_{1/3}O_2$.

3.1.1 2D Nanosheets as Electrode Materials

Exfoliation has emerged as a promising approach for obtaining large quantities of nanosheets by exploiting the expandable interlayer space in layer structured materials. As a result of the strong interlayer (highly covalent) bonding and weak (usually van der Waals) intralayer bonding in graphene and its semiconductor analogs (e.g. h-BN, MoS_2, WSe_2), these materials can be exfoliated using reductive methods. For example, treatment with a chemical reducing agent (e.g. n-BuLi, hydrazine)[61] or electrochemical reduction[62] distributes additional electronic charge onto the layers and increases the interlayer repulsion, allowing for intercalation of cations (e.g. Li^{+}) within the interlayer space,

which further increases the layer stacking distance. The intercalated phase can then be exfoliated into nanosheets with the aid of mechanical agitation such as ultrasonication.

3.1.2 Prior Methods to Exfoliate Layered Lithium Metal Oxides

In contrast to graphene and graphene-like layered materials, layered metal oxides typically contain charged layers separated by oppositely charged ions. In order to exfoliate materials with such strongly electrostatic interlayer bonding, protonated forms of the metal oxide are typically prepared and then exposed to solutions containing bulky tetraalkylammonium cations. Using solutions containing moderate ratios of ammonium cations to exchangeable protons results in the formation of organic intercalate phases with expanded interlayer spacings.[63, 64] The driving force for the process is the neutralization reaction between the acidic proton sites in the metal oxide and the basic amine.[55] In more concentrated solutions, intercalation of large amounts of the sterically large ammonium cations can facilitate solvation of the layers and result in osmotic swelling. This approach has been successfully demonstrated in a number of layered dielectric materials such as titanates, tantalates, and niobates.[65]

3.2 Synthesis and Reassembly of $LiCoO_2$

3.2.1 New Approach to Synthesis of Nanosheets

Here we present a modified exfoliation approach (Figure 3.1) that utilizes electrochemical oxidation to circumvent the proton exchange requirement. As a result, $LiCoO_2$ (LCO) and $LiNi_{1/3}Mn_{1/3}Co_{1/3}O_2$ (NMC) were successfully exfoliated into 2D nanosheets after intercalation with tetraethylammonium (TEA) cations. Purification of the nanosheets using dialysis and electrophoresis was investigated. To confirm the

absence of proton adsorption, the nanosheets were reassembled and electrochemically characterized. The restacked nanosheets demonstrated the expected discharge capacity under galvanostatic cycling. Furthermore, the metastable O2-polytype of LCO was observed in the restacked nanosheets. Our results show that this synthetic methodology enables the synthesis of 2D nanosheets from layered Li cathode materials that can be restacked into novel structures. Our work is a step forward for improving the exfoliation of nanosheets from complex metal oxides and also provides the groundwork for the design and fabrication of high performance hybrid materials for energy storage applications.

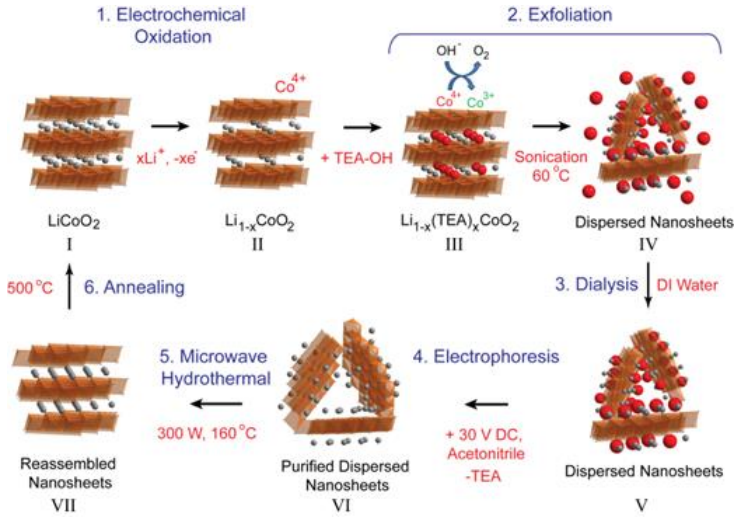

Figure 3.1 Process for the exfoliation of $LiCoO_2$ into nanosheets, purification, and reassembly.

3.2.2 Oxidation and Exfoliation

$LiCoO_2$ powder (I in Figure 3.1) was obtained (Sigma-Aldrich, particle size 2 - 5 μm) and mixed in de-ionized (DI) water with 5 wt% carboxymethyl cellulose (CMC, M_w ~ 250K, Sigma-Aldrich) to serve as binder. The slurry was subsequently coated onto aluminum foil current collectors and the dried electrodes were assembled with lithium metal counter electrodes into pouch cells. The electrolyte was 1 M $LiPF_6$ in EC/DMC/DEC (4:2:4 by vol, MTI Corp) and the separator was monoPE (Celgard). The electrodes were electrochemically oxidized (charged) galvanostatically first at a slow rate (0.05 C) to 4.3 V vs. Li/Li^+. The absence of conductive carbon would make $LiCoO_2$ not fully oxidized. In order to form $Li_{1-x}CoO_2$ (II in Figure 3.1), with a target of x = 0.5, the electrode was further potentially charged at 4.3 V for 1 hour, then rest for 15 minutes to see the open circuit voltage. If the voltage is lower than 4.29 V vs Li/Li^+ after rest, then repeat the potentially charged process until the open circuit voltage after rest is higher than 4.29 V (Figure 3.2A).

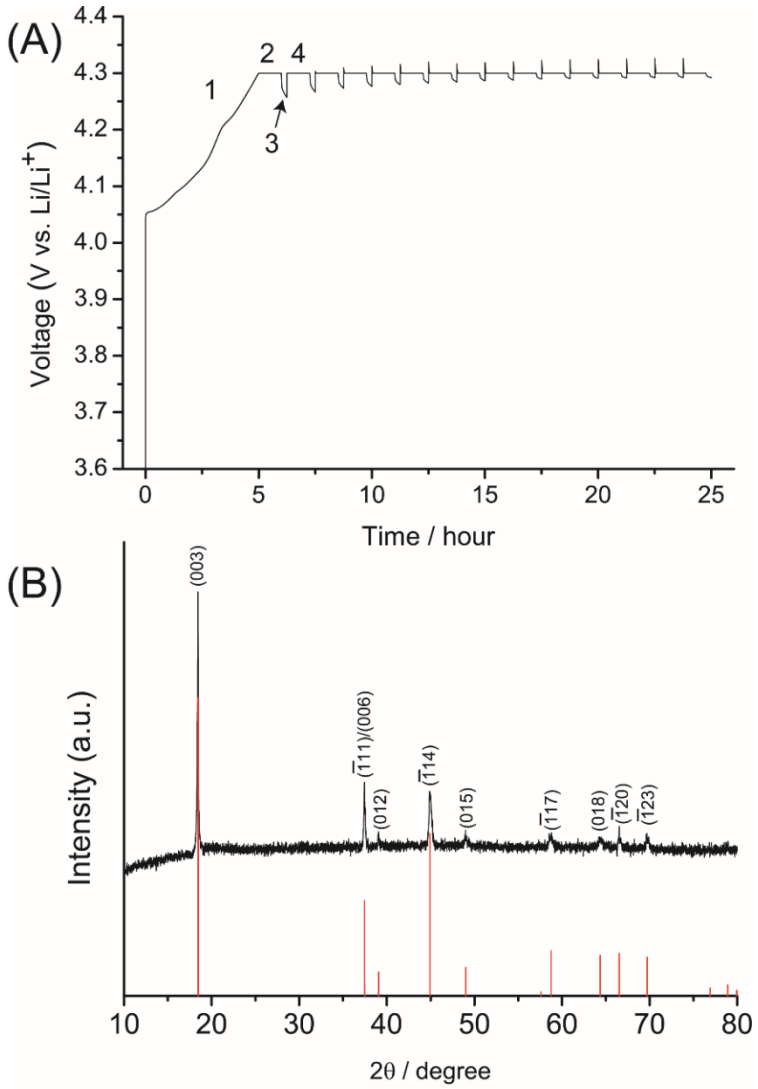

Figure 3.2 (A) Voltage vs. time plot of the charging process used to oxidize $LiCoO_2$. In region 1, the electrode was charged galvanostatically at 0.05 C until 4.3 V vs. Li/Li^+. Then the electrode was held at 4.3 V for 1 hour (region 2), followed by a 15 minute rest at open circuit (region 3) and another 1 hour hold at 4.3 V (region 4) if the open circuit voltage was less than 4.29 V. This was repeated for approximately 1 day until the open circuit was higher than 4.29 V. (B) XRD pattern of delithiated $Li_{0.5}CoO_2$ particles.

After electrochemical oxidation, the $Li_{1-x}CoO_2$ electrode was washed with DI water several times to remove the CMC binder. Previous studies investigating the properties of $LiCoO_2$ as an electrode for aqueous Li-ion batteries showed that it is stable at pH 7 and does not undergo proton intercalation.[66] After removal of CMC, the washed $Li_{1-x}CoO_2$ (0.14 g) was immersed in aqueous solutions (total volume 45 mL) containing different concentrations of tetraethyl-ammonium hydroxide (TEA, ~40% in water, Sigma Aldrich). The ratio of TEA: V_{Li^+} was varied at 0.5, 1, 2, 5, and 10. The concentrations and pH of these solutions are shown in Table 3.1.

Table 3.1 The redox potential for OH^-/O_2 in the different concentrations of TEA-OH solution, showing the feasibility of OH- oxidation by the LCO electrode after it was charged to 4.3 V vs. Li/Li^+.

TEA: V_{Li^+}	Concentration of TEA-OH (mM)	Solution pH	Redox potential of OH^-/O_2	
			V vs. NHE	V vs. Li/Li^+
10	166.2	13.65	0.42	3.46
5	83.1	13.40	0.44	3.48
2	33.2	13.09	0.46	3.50
1	16.6	12.83	0.47	3.51
0.5	8.3	12.55	0.49	3.53

After adding the $Li_{1-x}CoO_2$ into the TEA solutions (III in Figure 3.1), the mixture was sonicated using a tip probe ultrasonicator (CPX 600, 660 W) for 15 minutes to assist with

the intercalation of TEA into the $Li_{1-x}CoO_2$. Afterwards, the mixture was sonicated using a bath sonicator (CPX 1800H, 70 W) at 60 ^oC for two days. The use of elevated temperature during bath sonication was found to improve the yield of exfoliation. The solution was then centrifuged at 5000 rpm for 15 minutes to remove any unexfoliated particles. The unexfoliated particles in the pellet were used for XRD characterization, while the nanosheet dispersions (IV in Figure 3.1) were taken from the decanted phase of the TEA: V_{Li^+} = 1 solution for all other (e.g., ICP-MS, Raman, TEM, SEM, AFM) characterization, as well as further processing with dialysis and electrophoresis and subsequent electrochemical testing.

3.2.3 Dialysis (Purification of Nanosheets)

To remove residual TEA from the nanosheet dispersions, dialysis was employed using a Slide-A-Lyzer Dialysis Cassette (30 mL capacity, Thermo Scientific) with pores that can allow molecules with molecular weight 20K or below to pass through. The nanosheet dispersions (IV in Figure 3.1) were placed inside the dialysis cassette, which was then placed in 1 L of DI water and allowed to sit with slow stirring. The 1 L beaker was replaced with fresh DI water 4 – 6 times until the pH of the water decreased to 7 and the purified nanosheet dispersions (V in Figure 3.1) were removed.

3.2.4 Dialysis (Reassembly of Nanosheets)

Dialysis was also employed to reassemble the nanosheets through the slow exchange of TEA^+ with Li^+. The LCO nanosheet / TEA^+ dispersions (IV in Figure 3.1) obtained from the decanted phase were dialyzed in 1 M $LiNO_3$ solution for 1 day using the same

dialysis cassettes as above. Flocculation was observed due to the insertion of Li^+ in between the nanosheets.

3.2.5 Electrophoresis

Electrophoresis was performed using a DC regulated power supply (Circuit Specialists, CSI 3003X5) to purify the LCO nanosheets and remove adsorbed TEA^+. Fluorine-doped tin oxide (FTO) coated glass (TEC) was used as the substrate for both the cathode and anode. The nanosheet dispersion obtained after dialysis in DI water (V in Figure 3.1) was collected using centrifugation at 14,000 rpm for half an hour and then re-dispersed in acetonitrile. After applying a 30 V DC bias, the anode was coated with a layer of cobalt oxide sheets and the cathode was covered with an insulating white film consisting of TEA.

3.2.6 Microwave Hydrothermal Treatment

After electrophoresis, the nanosheets (VI in Figure 3.1) were collected from the FTO anode and re-dispersed with light sonication into DI water containing 1 M LiOH to reassemble the nanosheets back into LCO powders. Initially, the nanosheets dispersed in the LiOH solution quickly, indicating that there was strong electrical repulsion between the sheets. Within 10 minutes, flocculation was observed, indicating that the Li^+ ions were re-inserted in between the negatively charged $[CoO_2]^-$ layers. The flocculated suspension was then treated in a microwave hydrothermal reactor (Discover-SP, 300 W, 160 ^oC, 300 psi) for 30 minutes (VII in Figure 3.1) to improve the crystallinity of the reassembled particles.

3.2.7 Annealing

The LCO reassembled particles obtained after the microwave treatment (VII in Figure 3.1) were recovered using vacuum filtration, then annealed at 500 ^{o}C for 2 hours in air using an oven (Lindberg M, Thermal Scientific) to remove solvent and any residual organics or carbon as well as improve the crystallinity of the sample.

3.2.8 Atomic Layer Deposition (ALD) Deposition

Al_2O_3 films were deposited on electrodes containing reassembled LCO using ALD (Cambridge Nanotech, Savannah). The weight ratio of LCO active material : graphite : PVDF was 8:1:1. The ALD chamber was heated up to around 180 ^{o}C for the Al_2O_3 deposition. 30 cycles were used and the thickness of Al_2O_3 deposited by each 1 cycle was around 1 Å.

3.2.9 Materials Characterization

Multiple-collector inductively coupled plasma mass spectrometry (iCaP Q ICP-MS, Thermo Scientific) was used to analyze the composition of the LCO after charging (sample II in Figure 3.1), after exfoliation in TEA solution (sample IV), after electrophoresis (sample VI), and after reassembly (sample VII) different LCO samples. To obtain sample IV, the solution containing LCO suspended in TEA was centrifuged at 5000 rpm to remove the unexfoliated LCO particles, followed by vacuum-filteration through a 0.22 μm PVDF filter membrane (Sigma-Aldrich, Durapore) to obtain only nanosheets. All of the samples were digested with 70% nitric acid (trace metal grade) at 160 ^{o}C and 300 psi using a microwave hydrothermal reactor (Discover-SP, 909150).

For Raman spectroscopy, the nanosheets were recovered from the TEA solution using centrifugation (>14,000 rpm for half an hour) and dried at 50 ^{o}C. Raman spectra were collected with a 532 nm laser and a triple-grating monochromator (SpectraPro 300i, Action Research). The laser beam was focused onto the sample through a Mitutoyo M Plan Apo 50X objective with 0.42 N.A. Measuring powers at the samples were 230 μW and 47 μW for bulk LCO and LCO nanosheets respectively, and all spectra were collected with an exposure times of 60 s and 20 scans.

To prepare samples for TEM characterization, the nanosheet dispersion was centrifuged at 5000 rpm to remove the unexfoliated particles first. Then, the LCO nanosheets were separated from the aqueous TEA solutions using centrifugation at 14,000 rpm (Microfuge, I8) and collected from the decanted phase. The recovered LCO nanosheets were re-dispersed in isopropanol (LCO IPA dispersion) by sonicating with a tip probe sonicator (CPX 600, 660W) for 10 min and dropped onto a Cu grid for TEM characterization (JEOL 2010F) under 200 keV.

For AFM characterization, the LCO IPA dispersion was drop cast onto clean silicon substrates using spin coating at 600 rpm. The silicon substrate was sonicated in DI water, ethanol, and acetone for 30 minutes separately to clean the surface. AFM measurements were performed using an Asylum Research (MFP 3D, classic) microscope with tapping mode.

3.2.10 Thermal Gravimetrical Analysis

In this work, the LCO nanosheets recovered from the TEA solution using centrifugation were analyzed using TGA. The sample was dried in air at 105 ^{o}C overnight.

The sample (9.82 mg) was placed in a silicon crucible that was suspended from the arm of a microbalance. The crucible was then heated in a vertical tube furnace (Setaram TG 92) to 1000 ^{o}C with a ramp rate of 0.15 ^{o}C/sec in oxygen and the change in mass was recorded.

3.2.11 Electrochemical Testing

Cyclic voltammetry (CV): The as-prepared TEA-nanosheet dispersion was washed using dialysis in DI water first, then centrifuged at 14000 rpm to separate the nanosheets. This sample was then re-dispersed in *N*-methyl-2-pyrrolidone (NMP, Sigma Aldrich). Nanosheets collected from the anode after electrophoresis were re-dispersed in NMP directly. Polyvinylidene difluoride (PVDF, Sigma Aldrich) and graphite (C-Nergy, KS-6) were added into the nanosheet/NMP slurries with a ratio of 7:2:1 by weight. The slurry was coated onto Al foil using a doctor blade, then heated at 110 ^{o}C for at least 12 hours until completely dry. The acquired electrode was assembled into a pouch cell with Li metal as the counter electrode. 1 M $LiPF_6$ in EC/DMC/DEC (4:2:4) was used as the electrolyte (MTI Corp) and the separator was monoPE from Celgard. The CV measurements were performed using a potentiostat (Biologic MPG2) with a scan rate of 1 mV/s.

Galvanostatic cycling: The LCO active material was mixed with graphite and PVDF with a weight ratio of 8:1:1. The electrode and pouch cells were prepared as described before. Galvanostatic cycling was performed using a 0.2 C rate (25 mA/g) from 4.3 to 3 V vs. Li/Li^{+} (MPG2, Biologic). Differential capacity analysis was performed using the EC-lab software from Biologic.

3.3 Results and Discussion

3.3.1 Exfoliation of Nanosheets

The exfoliation process can be described by Equations (3.1) – (3.5):

$$LiCo^{3+}O_2 \rightarrow xLi^+ + xe^- + Li_{1-x}(V_{Li^+})_x(Co^{3+})_{1-x}(Co^{4+})_xO_2 \quad (3.1)$$

$$TEA\text{-}OH \rightarrow TEA^+ + OH^- \quad (3.2)$$

$$4OH^- \rightarrow 2H_2O + O_2 + 4e^- \quad (3.3)$$

$$Li_{1-x}(V_{Li^+})_x(Co^{3+})_{1-x}(Co^{4+})_xO_2 + xTEA^+ + xe^- \rightarrow Li_{1-x}(TEA^+)_x(Co^{3+})O_2 \quad (3.4)$$

$$Li_{1-x}CoO_2 + xTEA\text{-}OH \rightarrow Li_{1-x}(TEA^+)_xCoO_2 + (x/2)H_2O + (x/4)O_2 \quad (3.5)$$

Equation 3.1 describes the oxidation process in LCO during electrochemical charging, whereby Li^+ extraction results in the formation of Li vacancies, V_{Li^+}. Electrodes prepared from commercial $LiCoO_2$ were charged in Li metal half-cells using a slow rate (0.05 C). During charging, the $LiCoO_2$ *c*-axis distance, which represents the interlayer spacing, steadily increases due to the larger electrostatic repulsion experienced by the negatively charged $[CoO_2]^-$ layers during Li^+ extraction and reaches a maximum at $Li_{0.5}CoO_2$.[67] Upon reaching 4.3 V vs. Li/Li^+, approximately half of the Li^+ can be extracted, with half of the Co^{3+} oxidized to Co^{4+}.[26] At this composition, the vacancies and Li^+ have an ordered arrangement along the *a*-axis,[26] which can potentially promote insertion of TEA cations due to the formation of clear diffusion pathways (Figure 3.1). The XRD of charged LCO particles matches previous results of single crystal $Li_{0.5}CoO_2$ (Figure 3.2B).[68] Inductively coupled plasma – mass spectroscopy (ICP-MS) analysis on the charged Li_xCoO_2 particles showed that Li : Co was 0.58 (Table 3.2), slightly higher than expected, indicating that only 0.421 Li^+ per $LiCoO_2$ were electrochemically extracted.

The expected Li/Co ratio of 0.5 was likely not obtained because the LCO was not fully oxidized. In order to avoid complicating the subsequent nanosheet purification and characterization, conducting carbon was not used in preparing the LCO electrodes, which can have reduced electron transport through the material, leading to the incomplete delithiation of LCO.

Table 3.2 Composition of samples obtained using ICP-MS to determine the Li:Co and TGA to determine that adsorbed TEA. Sample names correspond to the labels in Figure 3.1.

Sample	Composition
II	$Li_{0.58}CoO_2$
IV	$Li_{0.22}(TEA)_{0.09}CoO_2$
VI	CoO_2
VII	$Li_{0.99}CoO_2$

After obtaining the charged Li_xCoO_2 (II in Figure 3.1), the electrode was rinsed with DI water, suspended in TEA-OH solution, and sonicated at 60 ºC. The TEA-OH solutions are highly alkaline and contain free hydroxide ions, as shown in Equation 3.2. Since the LCO was charged to 4.3 V vs. Li/Li^+, it has sufficient oxidation potential (Table 3.1) to oxidize OH^- to O_2 (Equation 3.3) and reduce Co^{4+} back to Co^{3+}. Indeed, when using $LiCoO_2$ as an electrocatalyst for the oxygen evolution reaction (OER), the onset potential for OH^- oxidation is around 0.8 V vs. NHE in pH 13 electrolyte, which is 3.84 V vs. Li/Li^+.[69] With the formation of Co^{3+}, cations in the electrolyte, TEA^+ in this

case, can then be intercalated into the LCO to maintain electroneutrality, as illustrated in Figure 3.3A. This reaction is depicted in Equation 3.4 and represents the analogous discharge process in a Li-ion battery except with the insertion of TEA^+ instead of Li^+ and the use of OH^- as an electron donor to reduce the Co^{4+} back to Co^{3+}. The presence of Li^+ vacancies, the increased interlayer spacing, and the driving force to maintain electroneutrality after charging all promote the insertion of TEA^+ into the LCO structure. Hence, the overall reaction can be written as shown in Equation 3.5. Once the $Li_{1-x}(TEA^+)_xCoO_2$ organic intercalate phase is formed, the expanded interlayer distance can facilitate the exfoliation of the material into nanosheets under mechanical agitation.

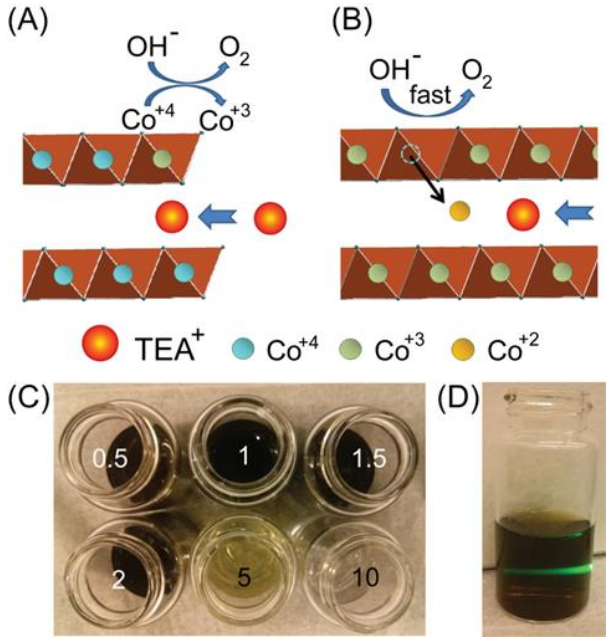

Figure 3.3 Schematic of TEA^+ intercalaction process in (a) low and (b) high concentration TEA^+ solutions. Photographs of (c) nanosheet dispersions obtained after exfoliation and centrifugation in solutions with TEA:V_{Li^+} of 0.5, 1, 1.5, 2, 5, and 10; (d) the Tyndall effect in dispersion with TEA:V_{Li^+} = 1.

The amount of TEA in the exfoliation solution was varied with respect to the molar ratio of Li^+ vacancies in the $Li_{0.5}CoO_2$, with TEA: V_{Li^+} of 0.5, 1, 2, 5 and 10 used. Ultrasonication with a tip probe sonicator for 15 minutes followed by bath sonication for 2 days at 60 ^oC was used to promote the exfoliation of LCO. After centrifugation to remove any unexfoliated particles, clear dispersions dark brown in color that displayed the Tyndall effect were observed for TEA:V_{Li^+} of 0.5 – 2 (Figure 3.3C-D). The lightly colored solutions for TEA:V_{Li^+} > 2 suggested that little exfoliation occurred at these concentrations. ICP-MS analysis of the nanosheets recovered from the TEA: V_{Li^+} = 1 solution using centrifugation (IV in Figure 3.1) showed that Li:Co was 0.22, confirming that Li^+ was still adsorbed onto the nanosheets after exfoliation.

In order to determine the amount of TEA^+ adsorbed on the nanosheets in Sample IV, we performed thermal gravimetric analysis (TGA) in oxygen up to 1000 ^oC on the sample after it was dried at 105 ^oC over night to remove residual solvent. According to previous studies, TEA degrades into ethylene and triethylamine between 200 – 500 ^oC, and is fully combusted to CO_2 by 700 ^oC.[70] Hence, the weight loss observed in our samples between 200 – 800 ^oC was assumed to be due to the removal of the TEA^+ from the nanosheets. At 500 ^oC, the weight loss was 11.2% (Figure 3.4).

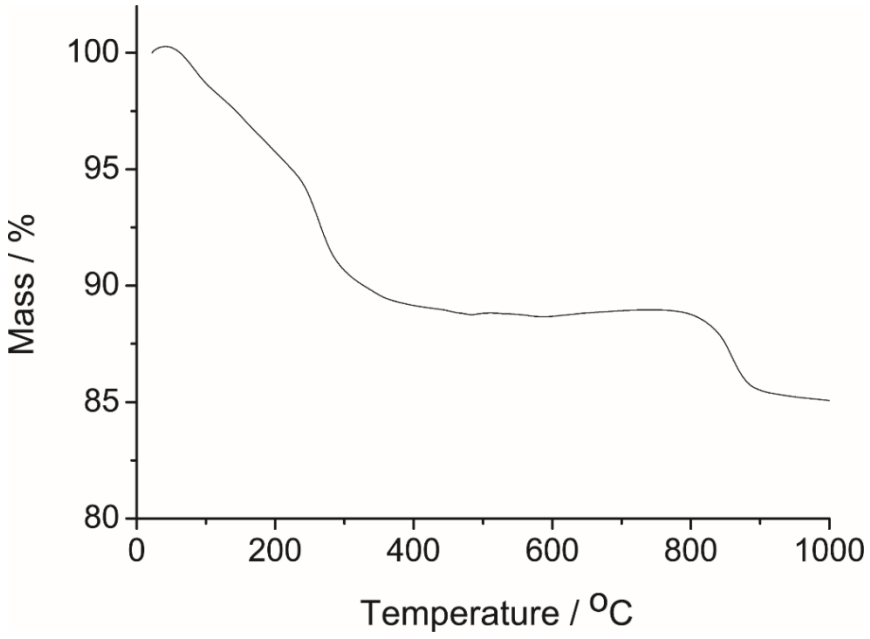

Figure 3.4 Thermal gravimetric analysis of the LCO nanosheets that were recovered from the TEA solution (TEA: V_{Li^+} = 1) using centrifugation. At 500 °C the mass loss was 11.2%.

Using this value and the molecular weight of TEA, along with the Li/Co ratio obtained from ICP-MS, a composition of $Li_{0.22}(TEA)_{0.09}CoO_2$ was calculated for Sample IV (Table 3.2). We note that that there is a large deviation from the expected composition of $Li_{0.5}(TEA)_{0.5}CoO_2$. This can be due to the large size of TEA^+, which causes it to occupy more space on the nanosheet surface. This also suggests that not all of the Li^+ vacancies need to be occupied by TEA^+ for exfoliation to occur.

X-ray diffraction (XRD) was used to characterize the LCO structure during the oxidation and exfoliation processes. The as-obtained powder was in the form of the O3-polytype of LCO (Figure 3.5A). The (003) reflection of the LCO at 18.9° shifted to lower angles after charging (Figure 3.5B), confirming the expansion of the interlayer distance

due to the electrochemical oxidation of LCO and extraction of Li^+. Upon treatment with TEA-OH, the XRD pattern of the unexfoliated LCO powders collected after centrifugation showed new reflections at ~13.1° and 26.3° (Figure 3.5C), which we attribute to the organic intercalate phase consisting of LCO with interlayer TEA^+. At the same time, the (003) reflection characteristic of discharged LCO was also observed, associated with particles that were not intercalated with TEA. As the TEA: V_{Li^+} concentration increased from 0.5 to 2, the amount of the TEA-intercalated phase decreased (Figure 3.6A). The peaks associated with the TEA-intercalated phase were barely observable when TEA: $V_{Li^+} > 5$. This result, along with the lightly colored dispersions (Figure 3.3C), indicated that the insertion of TEA into LCO was not achieved in these solutions.

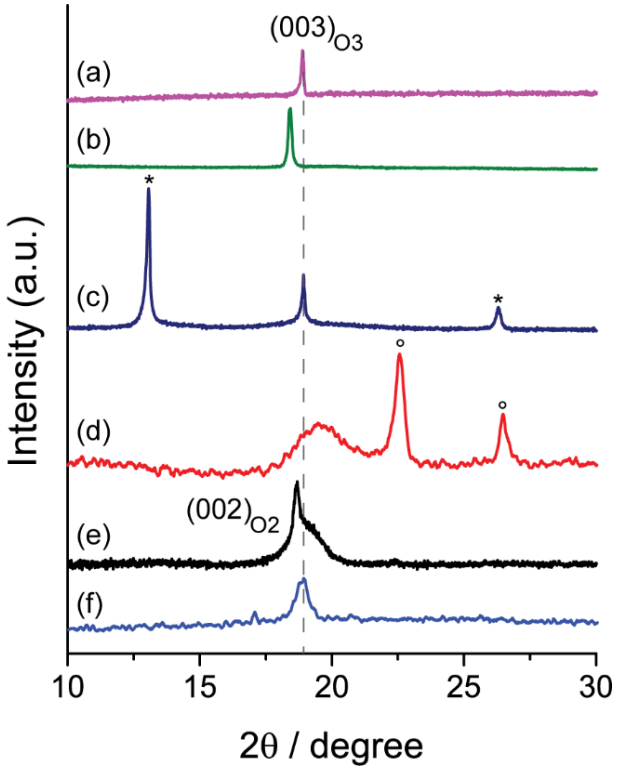

Figure 3.5 XRD patterns of LCO materials after different steps in the exfoliation and reassembly process between $10 < 2\theta < 30$. (a) The pristine, as-obtained powder; (b) electrode after electrochemical oxidation (i.e., $Li_{0.5}CoO_2$); (c) powder after TEA^+ intercalation; (d) nanosheets deposited onto FTO anode after electrophoresis; (e) nanosheets purified using electrophoresis and reassembled in 1 M LiOH with microwave hydrothermal reaction; (f) reassembled $LiCoO_2$ particles after annealing at 500 ^oC for 2 hours. Dotted line at 18.9^o corresponds to the (003) peak of pristine $LiCoO_2$, asterisks correspond to LCO intercalated with TEA, circles are peaks from FTO. (d) and (f) are scaled 3 times for easier comparison.

In the conventional exfoliation approach using proton-exchange, exfoliation is also not observed in solutions containing high concentrations of tetralkylammonium.[54, 57]

However, well-ordered swollen phases with large basal spacings are found in the centrifuged powders, consistent with the intercalation of large amounts of ammonium cations.[54, 57] This shows that the absence of exfoliation is from the enhanced electrostatic interaction between the negatively charged metal oxide layers and ammonium cations inside the interlayer space. In our case, however, the lack of organic intercalate phase indicates a different origin for the absence of exfoliation at higher TEA dosages. As shown in Table 3.1, the higher pH of the solutions with higher concentrations of TEA decreases the redox potential for the OH^- oxidation reaction. This would in turn decrease the overpotential for OH^- oxidation, and hence, increase the rate of reduction of Co^{4+}. However, the intercalation of TEA^+, which is controlled by the solid state diffusion of the bulky cation in between the LCO layers, is not affected by the change in pH and is likely much slower than the Co^{4+} reduction rate in the high TEA concentration solutions. Furthermore, it has been shown that large reduction currents (e.g. during high rate cycling) can cause the Co^{3+} to be reduced to Co^{2+}, which can migrate to the Li sites in the interlayer space[71, 72]. Examination of the XRD patterns between $35^o < 2\theta < 45^o$ revealed a large increase in the (006) peaks relative to the (101) reflections as the TEA concentration increased (Figure 3.6), which is an indication of the aforementioned Li/Co cation site disorder[73,72] . Hence, the little exfoliation observed for the solutions with TEA: $V_{Li^+} > 2$ can be from the formation of Co^{2+}, which can not only prevent exfoliation by blocking the TEA^+ diffusion pathways (Figure 3.3B), but can also increase the attraction between neighboring $[CoO_2]^-$ sheets and hinder intercalation.[71]

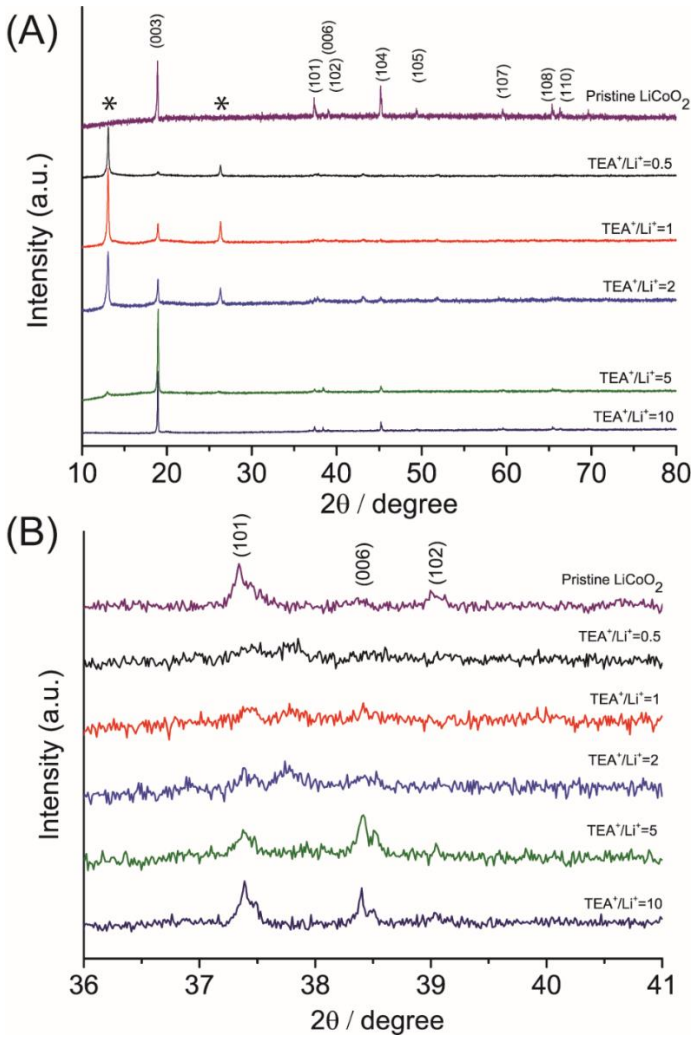

Figure 3.6 (A) XRD of pristine LCO (O3-type) and unexfoliated LCO obtained after sonication and centrifugation in different TEA^+:V_{Li^+} of 0.5, 1, 2, 5, and 10. Planes from O3-LCO are labelled and asterisks indicate peaks for the LCO intercalated with TEA^+; (B) Zoom-in of XRD patterns from $35^o < 2\theta < 40^o$.

In contrast to protonated metal oxides, where more ammonium cations are intercalated in the higher dose solutions, our results show that very little organic intercalate forms in the high TEA solutions using our method. Hence, our exfoliation mechanism is not driven by an acid/base neutralization reaction as for the protonated metal oxides, but

rather one based on the stoichiometry of oxidized cobalt species formed during electrochemical oxidation. From our results, this exfoliation process is much faster than that usually obtained with osmotic swelling through the proton-exchange route, which usually requires several weeks.[54, 57, 63] This is because the intercalation of TEA^+ is assisted by the oxidation of hydroxide and driving force towards electro-neutrality, whereas the usual proton exchange method only relies on the diffusion of guest ions between layers.

The nanosheets were recovered from solution using centrifugation and Raman spectroscopy was performed to acquire structural information. Commercial bulk LCO was used as a comparison. As shown in Figure 3.7, the bulk LCO was characterized by the E_g peak at 486 cm^{-1}, which represents the O-Co-O bending mode in the *a-b* basal plane, and the A_{1g} peak at 596 cm^{-1}, which corresponds to Co-O stretching modes along the *c*-axis[74]. In comparison, the Raman spectrum of the nanosheets showed peak broadening and shifted towards higher wavenumbers, the latter which is correlated with an expansion in the *c*-axis.[74] This is possible if the nanosheets reassembled with TEA^+ in between the layers during the centrifugation process. The peak broadening and shift to higher wavenumbers have also been correlated with the presence of nanosized crystals.[75, 76] The A_{1g} peak was found to split into two peaks at 582 and 613 cm^{-1}, which can be the influence of adsorbed TEA^+ and Li^+ on the Co-O stretching mode. Also, no peaks from $LiCoO_2$ spinel or Co_3O_4 phases[75] were observed, indicating that the layered hexagonal $[CoO_2]^-$ structure was maintained during exfoliation.

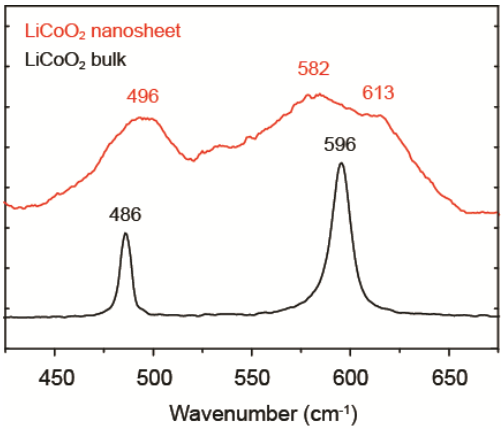

Figure 3.7 Raman spectrum of bulk LCO and $LiCoO_2$ nanosheets obtained by centrifuging the nanosheets exfoliated with $[TEA^+]:[V_{Li}+] = 1$.

3.3.2 Purification of Nanosheets

To purify the nanosheets and remove excess TEA, the nanosheet dispersions were subjected to dialysis in DI water. Transmission electron microscopy (TEM) of the dispersions after dialysis (sample V in Figure 3.1) confirmed the nanosheet morphology (Figure 3.8A and B). The high resolution TEM image and electron diffraction pattern revealed a hexagonal structure and a = 2.814 Å, which matched that for bulk O3-LCO (a = 2.817 Å, $R\bar{3}m$ space group)[67]. The integrity of the basal plane confirmed that the exfoliation occurred along the layer stacking direction along the c-axis.

Atomic force microscopy (AFM) showed the thickness of the nanosheets was 1 – 2 nm, which is similar with previous investigations on cobalt oxide nanosheets[54] and suggests that the nanosheets were single and double layered sheets (Figure 3.8C and D). The lateral dimension of these nanosheets was around 50 – 200 nm while the initial LCO particles were 2 – 5 μm. This difference can indicate that the nanosheet dimensions were

restricted by the diffusion of TEA into the bulk LCO and/or that the nanosheets were fragmented during ultrasonication.

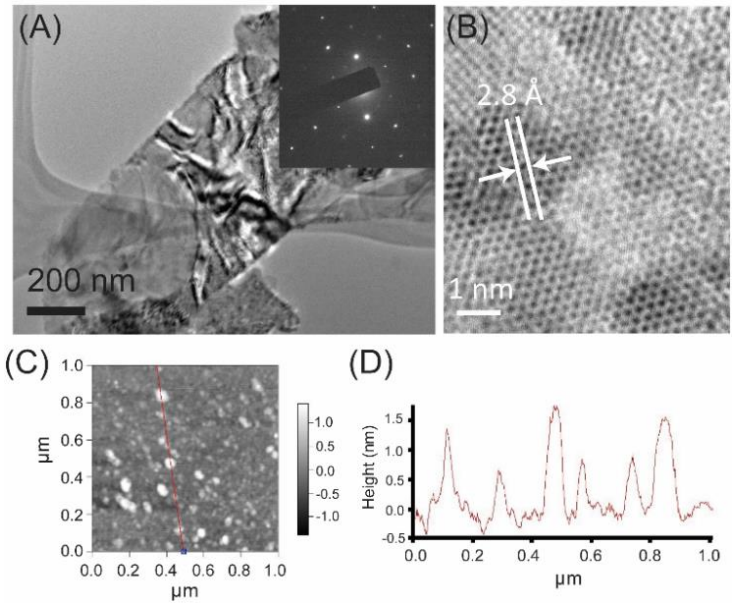

Figure 3.8 (A) TEM with electron diffraction pattern inset and (B) high resolution TEM of exfoliated LCO nanosheet. (C) AFM image of exfoliated LCO nanosheets and (D) height profile showing the thickness of nanosheets is around 1 - 1.5 nm.

3.3.3 Reassembly of Nanosheets

With the Raman spectroscopy, TEM, and AFM results confirming that the LCO was successfully exfoliated, the nanosheets were reassembled back into $LiCoO_2$ to demonstrate that they can serve as functional building blocks for building up cathode materials. The nanosheet dispersions in the TEA solutions were dialyzed in 1 M $LiNO_3$ solution (rather than DI water as for the TEA^+ removal) for 1 day. In this dialysis process, the TEA^+ ions slowly diffuse out of the nanosheet dispersion while Li^+ ions diffuse in. Due to the negatively charged surface of the $[CoO_2]^-$ layers, the presence of Li^+ will

cause flocculation. As a result of the slow diffusion of ions during dialysis, the nanosheets can restack and grow under a slow and controlled rate. Scanning electron microscopy (SEM) images of the reassembled nanosheets showed that the resulting particles were very smooth, with the layer stacking clearly visible on the edges of the particles (Figure 3.9).

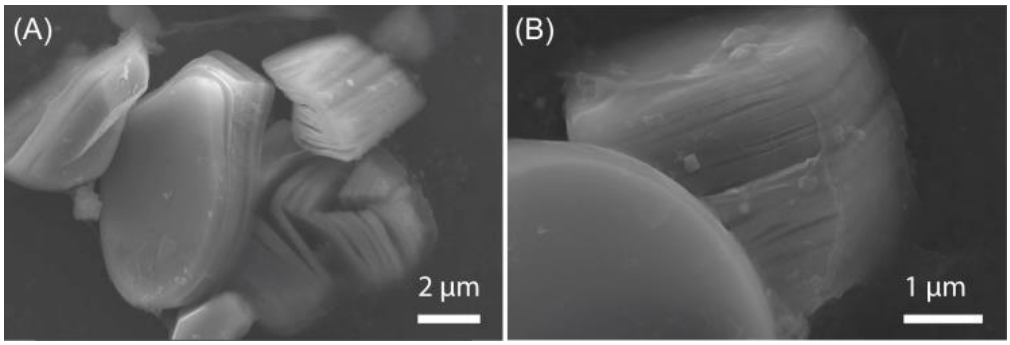

Figure 3.9 SEM images of LCO nanosheets restacked into particles after using dialysis of the nanosheet/TEA^+ dispersion in 1 M $LiNO_3$.

Although the dialysis procedure was effective for obtaining dispersions of well isolated nanosheets (when performed in DI water) as well as restacked LCO particles (when performed in $LiNO_3$ solution), the resulting materials did not display high electrochemical activity. As shown in Figure 3.10A, cyclic voltammetry measurements prepared from nanosheets obtained after dialysis in DI water only displayed small capacitances associated with double layer charging, with the Co^{3+}/Co^{4+} redox peaks at 3.7 and 3.8 V vs. Li/Li^+ barely observable. Galvanostatic charging/discharging of the nanosheets after dialysis in DI water (Figure 3.11A) and the restacked LCO particles obtained after dialysis in $LiNO_3$ (Figure 3.11B) also did not result in any significant capacity. Since other Li-ion battery materials prepared in sheet morphology using

synthetic methods, rather than exfoliation, demonstrate similar potential-dependent activity as the bulk materials[76, 77], this inactivity is most likely due to the presence of TEA^+ which can hinder electrical contact of the nanosheets. The TEA^+ can also function as guest charge balancing ions and block Li^+ sites.[78, 79] Hence, these results show that although dialysis was effective for removing excess TEA^+ from solution, it was not effective for removing TEA^+ adsorbed on the nanosheet surfaces.

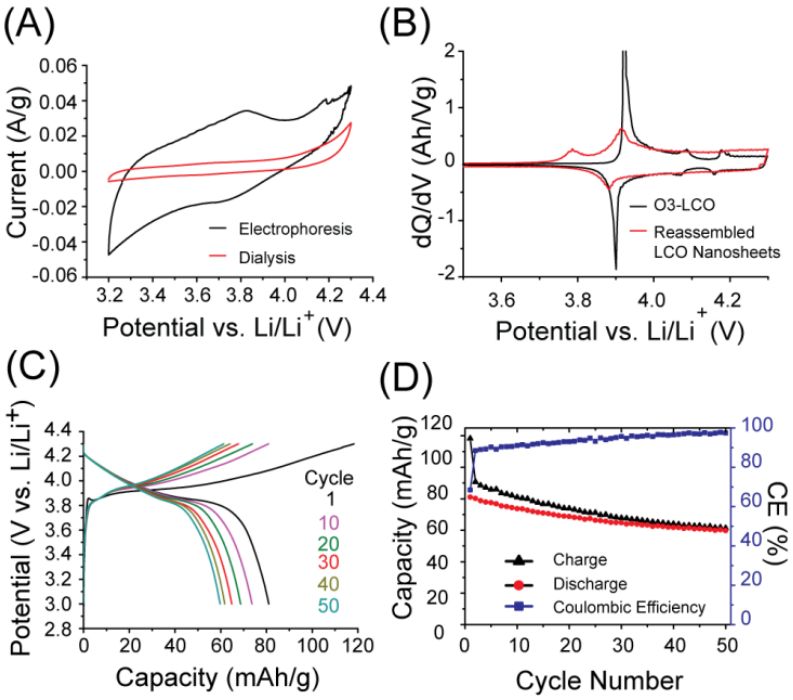

Figure 3.10 (A) Cyclic voltammetry (1 mV/s) of LCO nanosheets after dialysis in DI water compared to LCO nanosheets that were purified using electrophoresis. (B) Differential capacity plots of LCO derived from reassembled nanosheets after purification by electrophoresis, microwave hydrothermal treatment, and annealing at 500 ^oC (2^{nd} cycle) compared with commercial bulk O3-LCO. (C) Galvanostatic voltage

profiles and (D) capacity and Coulombic efficiency (CE) vs. cycle number using a 0.2C rate for LCO particles in (B) coated with 3 nm ALD Al_2O_3.

To investigate this issue, electrophoresis was employed to try to separate the TEA^+ ions adsorbed on the nanosheets using protocols adapted from the literature[80]. Electrophoresis was performed on LCO nanosheets in aqueous dispersions after the DI water dialysis. Only 10 V of DC voltage was applied because higher voltages resulted in water electrolysis. Afterwards, the cathode was covered with a film of dark brown materials, while the anode was clean (uncoated). This indicated that the nanosheets were positively charged in aqueous solution, confirming that their surfaces were covered with adsorbed TEA^+. On the other hand, when electrophoresis was performed in acetonitrile with a 30 V DC bias, the cathode was covered with a white film attributed to the TEA^+ and the LCO nanosheets deposited on the anode, indicating that they are negatively charged and separated from the TEA^+.[79] This was also confirmed by performing cycling voltammetry on the nanosheets after dialysis and electrophoresis (Figure 3.10A). The Co^{3+}/Co^{4+} redox peaks were observed at ~ 3.8 V vs. Li/Li^+, indicating that the TEA must be removed to recover the electrochemical activity of the nanosheets. ICP-MS analysis of the purified nanosheets showed that Li: Co was 0.0025, which means that in addition to the TEA^+, most of the Li^+ was removed from the nanosheets during electrophoresis. The concentration of Li^+ in the digested solution is below 0.1 ppm, which means the existence of Li^+ is hardly observed. Therefore it can be treated as CoO_2 nanosheets.

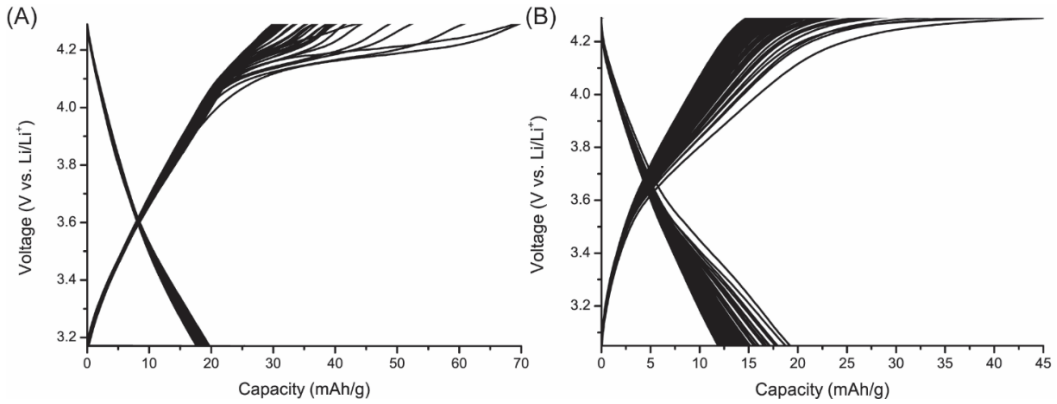

Figure 3.11 Galvanostatic cycling data of nanosheets (A) after dialysis in DI water, (B) after restacking through dialysis in 1M $LiNO_3$. Fifty charge/discharge cycles are shown for both materials.

In order to confirm the electrochemical functionality, the nanosheets were reassembled back into LCO powders. After electrophoresis in acetonitrile, the LCO nanosheets were collected from the anode and re-dispersed in DI water. To ensure that there was sufficient Li available to promote re-formation of $LiCoO_2$, 1 M LiOH was added to the DI water. The reassembling process was conducted using microwave hydrothermal treatment at 160 ^oC to improve the crystallinity of the reassembled particles as well as decrease the reaction time from 5 days (for conventional hydrothermal reaction) to 15 minutes.[55]

XRD analysis of the samples after electrophoresis revealed the (003) peak for LCO, indicating the successful restacking of the nanosheets, but with a position ($2\theta \sim 19.5^o$) suggesting a smaller c-axis spacing, perhaps due to Li^+ deficiency and/or the high electric field compressing the interlayer spacing (Figure 3.5D). After the microwave treatment, ICP-MS analysis on the sample showed that Li:Co was 0.99 (Table 3.2), confirming that lithium was successfully inserted back in between the cobalt oxide layers. The XRD pattern (Figure 3.5E) of the reassembled LCO particles showed a broad peak matching

the (003) reflection at 2θ ~18.9° for LCO. A sharp peak at 2θ ~18.6° was also observed, which matched the (002) peak for the O2-polytype of LCO. Peak fitting showed the integrated O3/O2 peak area ratio was 4.31 (Figure 3.12A inset), indicating the particles consisted of mixed phases. The XRD pattern of the reassembled LCO after microwave hydrothermal treatment also contained traces of the spinel Co_3O_4 (Figure 3.12A), which may have originated from Li^+ deficient domains that formed during flocculation.

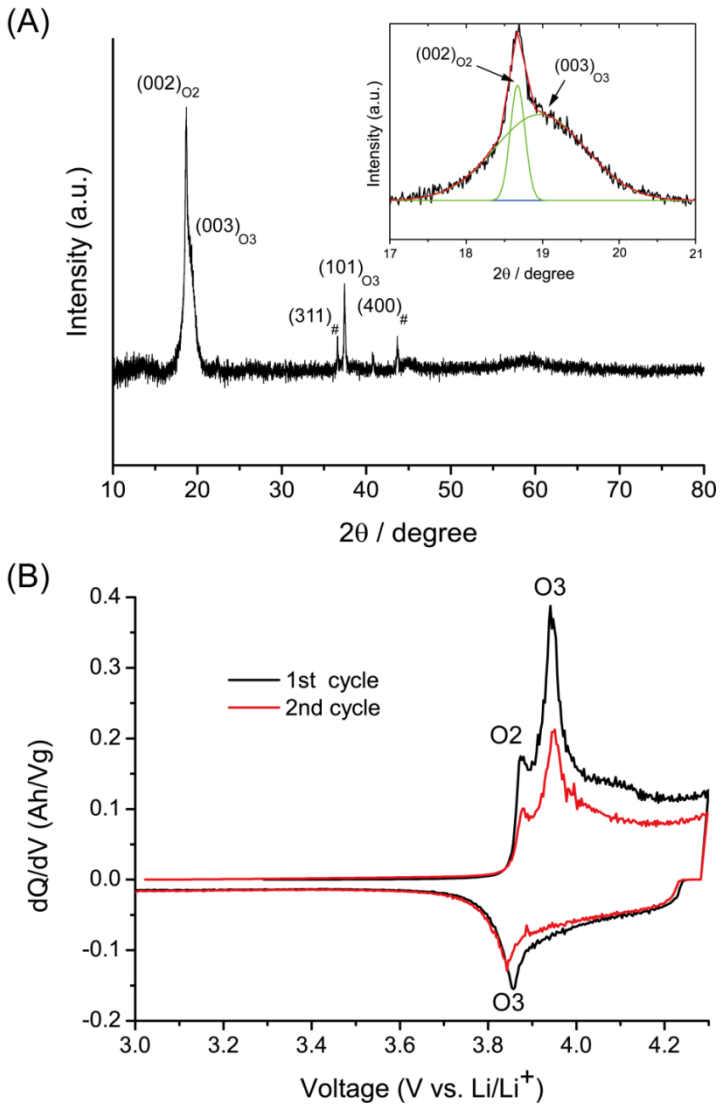

Figure 3.12 Characterization of LCO particles reassembled after electrophoresis and microwave hydrothermal treatment in LiOH without annealing. (A) XRD with inset showing fitting results to O2 and O3-LCO reflections; #: Co_3O_4. (B) Differential capacity vs. potential plot obtained from galvanostatic measurement showing delithiation from O2 and O3-LCO.

The observation of the O2-polytype in these materials is particularly interesting since it is a metastable phase that transforms to the equilibrium O3-phase when sintered at temperatures higher than 270 ^{o}C.[81, 82] O2-LCO is conventionally obtained through a Li^{+}/Na^{+} ion-exchange treatment of the P2-polytype of $NaCoO_2$, during which CoO_2 slab gliding occurs in order to form octahedral environments for the Li^{+}, which are too small to reside in the Na^{+} trigonal prismatic sites.[83] Unlike O3-LCO, where every cobalt oxide layer is related by translation, in the O2 structure, every adjacent cobalt oxide layer is mirrored or rotated 60^{o} along the *c*-axis (Figure 3.13).[81] Hence, it is not possible to obtain O2-LCO directly from O3-LCO. On the other hand, when restacking the nanosheets using flocculation, the formation process is rapid due to the strong electrostatic interactions between the Li^{+} ions and $[CoO_2]^{-}$ sheets. Therefore, it is likely that a large amount of stacking faults formed during the nanosheet reassembly process, which can induce the formation of metastable O2-LCO domains. Furthermore, the low temperature used in the microwave hydrothermal treatment was not sufficient to transform the O2-LCO to the thermodynamic O3-phase.

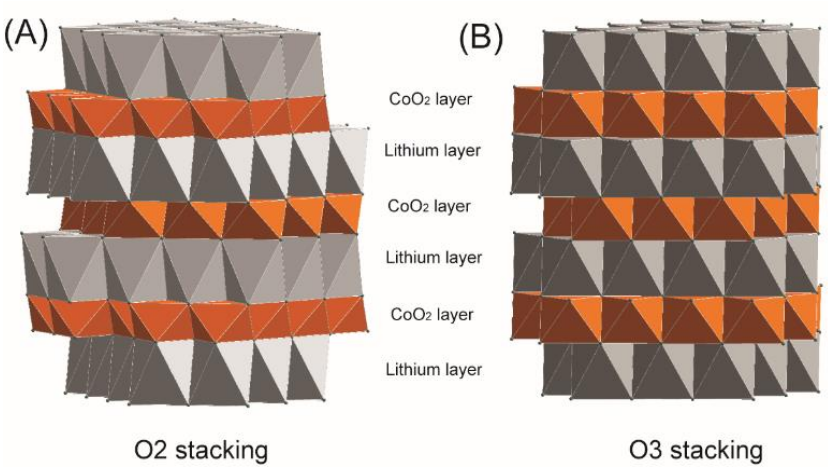

Figure 3.13 LCO polytypes with different CoO_2 slab arrangements in the layer stacking direction along the *c*-axis (A) O2-LCO and (B) O3-LCO.

After the microwave hydrothermal treatment, the particles were annealed at 500 ^oC for 2 hours. Heat treatment at temperatures higher than 300 ^oC is typically necessary for the crystallization of hydrothermally synthesized LCO.[77] After annealing at 500 ^oC, the XRD pattern showed that the mixed phase O2/O3-LCO was transformed to the O3-polytype (Figure 3.5F, full range in Figure 3.6). In contrast, $[CoO_2]^-$ nanosheets prepared by exfoliation of $HCoO_2$ and then reassembled with LiOH show an additional XRD reflection at 20.3^o from intercalation of protons,[55] indicating the formation of $Li_{1-x}H_xCoO_2$ rather than LCO. Our results show that with our method, the LCO structure is successfully achieved without interference from proton adsorption.

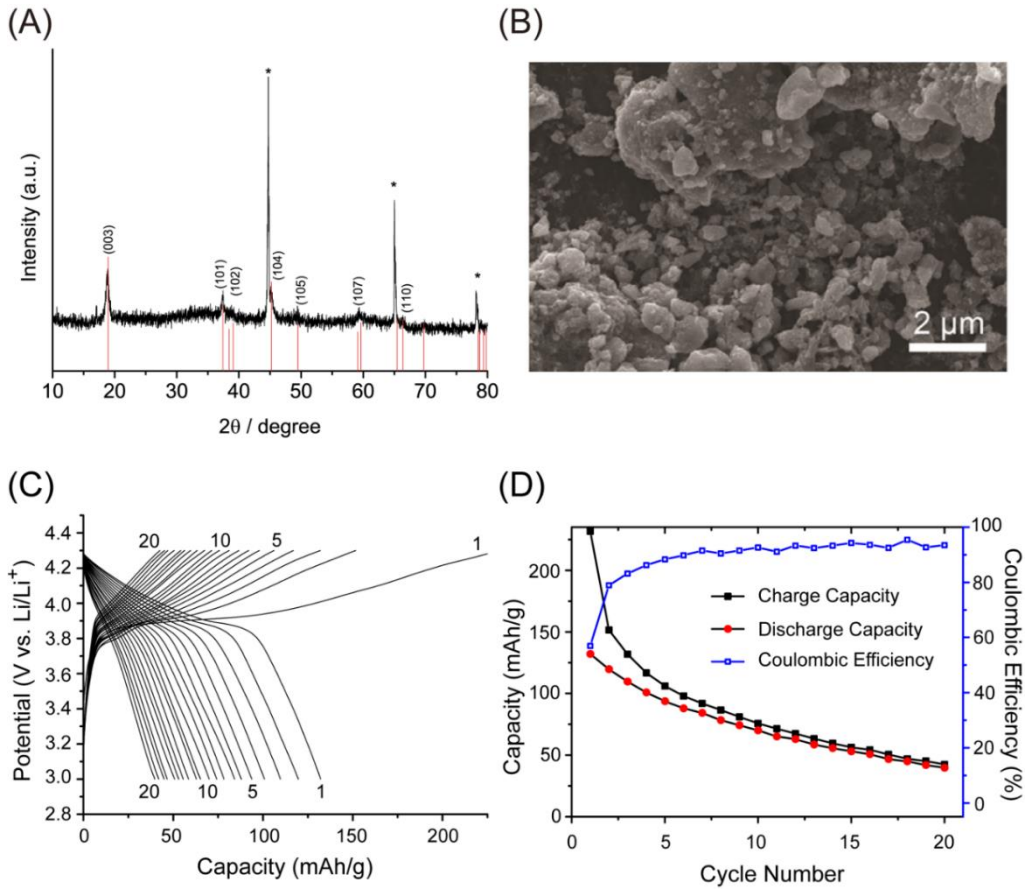

Figure 3.14 Characterization of reassembled LCO particles obtained after purification by electrophoresis, microwave hydrothermal treatment, and annealing at 500 ^{o}C for 2 hours. (A) XRD pattern matching O3-LCO; * indicate peaks from Al foil substrate. (B) SEM images, (C) Galvanostatic cycling data between 3.0 - 4.3 V vs. Li/Li^{+}. (B) Coulombic efficiency, charging and discharging capacity of each cycle.

3.3.4 Electrochemical Performance of Reassembled Nanosheets

The mixed phase LCO particles obtained after electrophoresis and microwave hydrothermal treatment were evaluated using galvanostatic cycling. The differential capacity plots (Figure 3.12B) showed two oxidation peaks at 3.87 and 3.95 V vs. Li/Li^{+}, corresponding to oxidation (delithiation) of O2- and O3-LCO, respectively.[81] This further

confirms the XRD results (Figure 3.12A) that the reassembled particles contain a mixture of the O2 and O3-polytypes of LCO.

The electrochemical properties of the mixed phase particles after annealing at 500 ^{o}C for 2 hours were also studied. Under galvanostatic cycling, the reassembled particles showed a discharge capacity of 131 mAh/g in the first cycle (Figure 3.14C), which is slightly lower than the 140 mAh/g typically observed in bulk LCO[76] but much higher than the previous attempts to obtain LCO from nanosheets due to the absence of interfering protons. For instance, $Li_{1-x}H_xCoO_2$ restacked nanosheets prepared from the exfoliation of $HCoO_2$ showed first cycle discharge capacities < 74 mAh/g.[55] Analysis of the differential capacity plots (Figure 3.10B) showed that oxidation features from O2-LCO were still present, despite our XRD results showing reflections only from O3-LCO (Figure 3.14A). This may indicate that the O2-LCO domains are very small, since previous studies showed that only traces of O2-LCO remain after annealing at 400 ^{o}C.[81] Both O2- and O3-LCO features decreased with cycling (Figure 3.15A), leading to poor capacity retention (Figure 3.14D). Due to side reactions with the electrolyte and surface instability, nanostructured LCO typically demonstrates poor cycling and low Coulombic efficiency[76, 77, 84] unless passivated with surface coatings[85]. Inspection of the reassembled LCO with SEM imaging showed that they consisted of particles ranging from a few hundred nanometers to ~ 2 μm (with some larger agglomerates containing several particles) (Figure 3.14B).

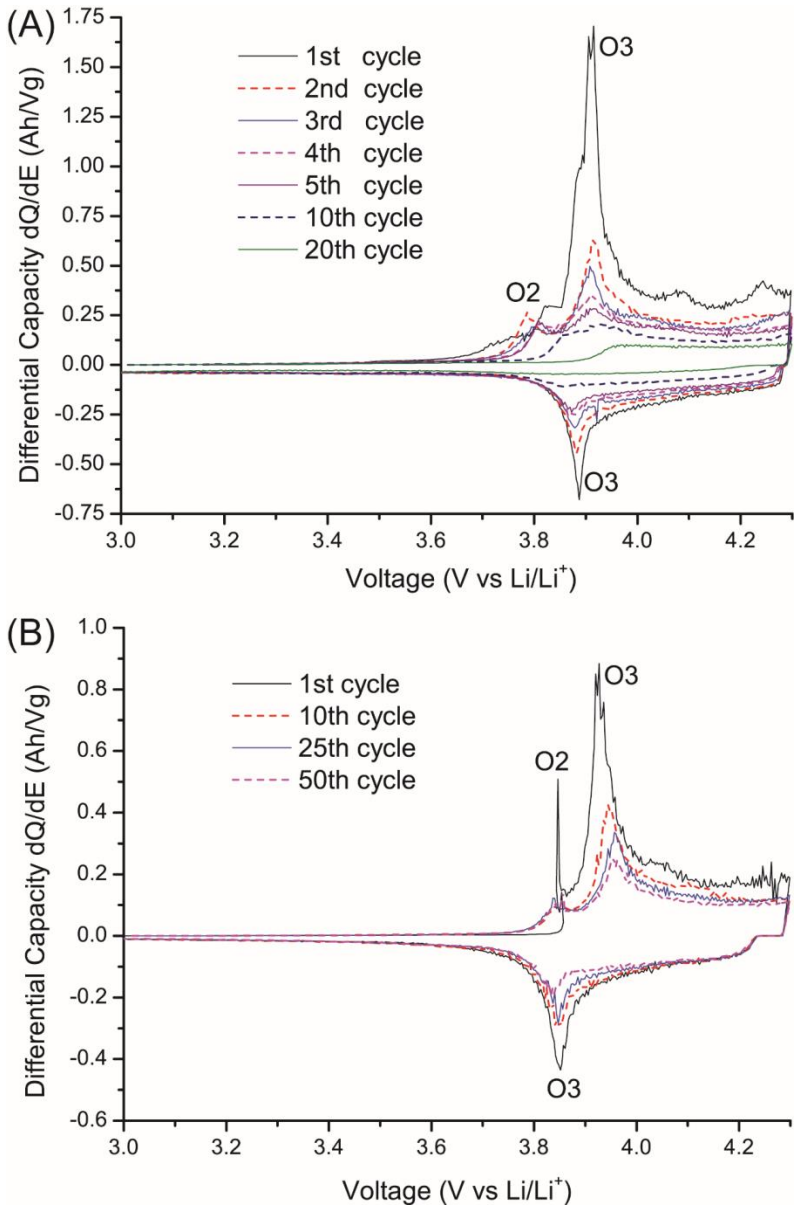

Figure 3.15 Differential capacity vs. voltage plot of LCO reassembled particles (A) without ALD coating and (B) with Al_2O_3 ALD coating.

To investigate whether surface passivation can also improve the cycling performance of the reassembled LCO nanosheets, atomic layer deposition (ALD) was used to deposit 3 nm of Al_2O_3. The initial capacity decreased to ~ 81 mAh/g (Figure 3.10C), likely due to

the un-optimized layer thickness and insulating nature of the Al_2O_3,[85] but the capacity retention was greatly improved, with 74% retained after 50 cycles (Figure 3.10D), compared to only 30% after 20 cycles for the uncoated materials (Figure 3.14D). The differential capacity plots (Figure 3.15B) showed that both O2- and O3-LCO redox peaks were stable with the ALD coating. These results show that our nanosheet synthesis and restacking process can be applied to form functional LCO materials with improved electrochemical properties compared to conventional osmotic swelling methods. Furthermore, the restacking can be used to obtain non-equilibrium structures, as demonstrated by the formation of the O2-LCO, which can lead to novel electrochemical behavior. Although the morphology of the restacked nanosheets does not contain fine nanostructures, the cycling properties are similar in that poor capacity retention and Coulombic efficiencies can be remedied with surface passivation using ALD coatings. Future efforts will be focused on the improvement of cycling by obtaining better control over the structure of the reassembled particles, as well as exploring hybrid structures.

3.4 Conclusion

In summary, a new method was developed to obtain cobalt oxide nanosheets by exfoliation of $LiCoO_2$ with TEA-OH. The approach uses electrochemical oxidation to create a driving force for TEA insertion into the interlayer space without requiring a proton exchange step. Purification of the nanosheets was successfully performed with dialysis and electrophoresis, which facilitated the nanosheet reassembly into functional cathodes for Li-ion batteries. This methodology can be applied to other layered materials

with strong interlayer bonding to make functional nanosheets and novel Li-ion battery materials.

4 EXFOLIATION AND REASSEMBLY OF NMC 2D NANOSHEETS

4.1 Introduction to the Exfoliation of NMC 2D Nanosheets

In the last chapter, by using method of oxidation-reduction assisted exfoliation, $LiCoO_2$ (LCO) was successfully exfoliated into nanosheets and reassembled back into functional $LiCoO_2$ particles. One of the interesting observations was that two different structures caused by different oxygen packing, known as O2 and O3 phase, were found in the reassembled particles. It also worth noticing that in the differential capacity of reassembled LCO, two minor peaks that should exist in O3 LCO at 4.08 V and 4.16 V vs Li/Li^+, corresponding to the phase change from monoclinic to hexagonal and hexagonal to monoclinic respectively, has disappeared. The phase change induced the change in c-axis spacing, which is directly related to the structure stability and cobalt loss.[28] As the cutoff voltage of the cell increases, the capacity fades quickly, coming along with the decrease in the c-axis and increase of cobalt loss which brings irreversible capacity[27, 28]. These structural changes would induce internal stress which would lead to the collapse of the active matrix. Therefore, the disappearance of the peaks that correspond to the phase change suggests that the restacked materials are probably more stable than bulk materials during cycling.

Thus, it is interesting to study the exfoliation of another widely used layered material, $LiNi_{1/3}Mn_{1/3}Co_{1/3}O_2$(NMC), which has been previously exfoliated but without any electrochemical investigation on either nanosheets or reassembled particles. The exfoliation of $LiNi_{1/3}Mn_{1/3}Co_{1/3}O_2$ can not only prove the universality of the oxidation-

reduction assisted exfoliation method, but can also enable the investigation of new emerging properties and structure in restacked NMC particles. At the same time, reassembly of two different kinds of nanosheets provide an opportunity to design new layered materials cathodes to break the bottleneck of cathode as discussed in the last chapter.

4.2 Synthesis of NMC Nanosheets

4.2.1 Oxidation of $LiNi_{1/3}Mn_{1/3}Co_{1/3}O_2$

The exfoliation of $LiNi_{1/3}Mn_{1/3}Co_{1/3}O_2$ powder (NMC, Sigma-Aldrich) follows previous section. The SEM and XRD of pristine $LiNi_{1/3}Mn_{1/3}Co_{1/3}O_2$ are shown in Figure 4.1

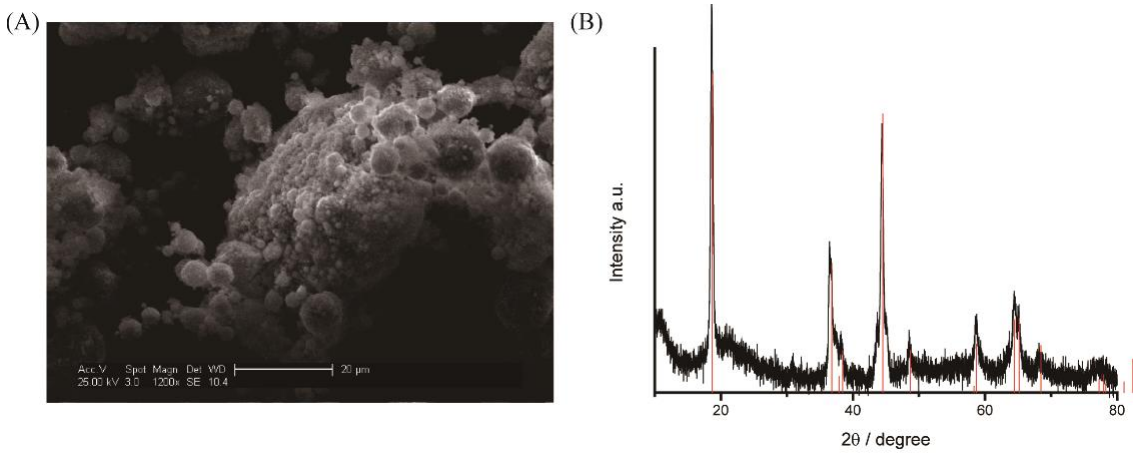

Figure 4.1 SEM (A) &XRD (B) of pristine NMC particles.

The NMC powder was mixed in de-ionized (DI) water with 5 wt% carboxymethyl cellulose (CMC, Mw ~ 250K, Sigma-Aldrich) to serve as binder and the slurry was subsequently coated onto aluminum foil current collectors. NMC particles were potentiostatically charged at a 4.3 V vs. Li/Li^+ at a current of 7 mA/g to reach a Lithium

deficient composition of $Li_xNi_{1/3}Mn_{1/3}Co_{1/3}O_2$ ($0<x<1$). The conductivity of NMC is not as good as LCO, thus the battery was charged for around 2 days in order to fully delithiate NMC at certain voltage. After electrochemical oxidation, the charged NMC electrode was washed with DI water several times to remove the electrolyte and CMC binder.

4.2.2 Exfoliation of $Li_xNi_{1/3}Mn_{1/3}Co_{1/3}O_2$

The washed NMC (0.14 g) was immersed in tetraethylammonium hydroxide (TEA, ~ 40% in water, Sigma Aldrich) aqueous solution with a volume of 45 mL and concentration of 0.025 M. After immerging charged NMC particles into the TEA solutions, the mixture was sonicated using a tip probe ultrasonicator (CPX 600, 660 W) for 15 minutes to assist with the intercalation of TEA into the NMC. Afterwards, the mixture was sonicated using a bath sonicator (CPX 1800H, 70 W) at 60 ^oC for two days. The solution was then centrifuged at 5000 rpm for 15 minutes to remove any unexfoliated particles. The unexfoliated particles in the pellet were used for XRD characterization, while the nanosheet dispersions were taken from the decanted phase for all other (e.g., ICP-MS, Raman, TEM, SEM, AFM) characterization, dialysis and electrophoresis.

4.2.3 Dialysis of $Li_xNi_{1/3}Mn_{1/3}Co_{1/3}O_2$ Nanosheets Dispersion

To remove TEA ions from the nanosheet dispersions, dialysis was employed using a Slide-A-Lyzer Dialysis Cassette (30 mL capacity, Thermo Scientific) with pores that can allow molecules with molecular weight 20K or below to pass through. The nanosheet dispersions were placed inside the dialysis cassette, which was then placed in 1 L of DI water and allowed to sit with slow stirring. The 1 L beaker was replaced with 0.1 M

$LiNO_3$ solution afterwards for 2 – 3 times until the pH of the water decreased to 7. Due to the negatively charged surface of NMC, the nanosheets in the dispersion would slowly flocculate under electrostatic force brought by lithium ion which diffuse slowly into the dispersion through the membrane.

4.2.4 Electrophoresis

After the reassembly through dialysis, the particles were separated from the dispersion through the centrifuge. The collected reassembled particles were washed with DI water once. Then the washed particles were dispersed in acetonitrile (Sigma-Aldrich) by bath sonicating for 15 minutes. The washed NMC reassembled particles should avoid being dried due to requirement to disperse on next step. After being dispersed in acetonitrile, electrophoresis was performed using a DC regulated power supply (Circuit Specialists, CSI 3003X5) to purify the NMC nanosheets and remove any adsorbed Li^+, H^+ and TEA^+. Stainless steel which was cleaned in DI water, ethanol and acetone was used as the electrode for both the cathode and anode.

4.2.5 Microwave Synthesis

After electrophoresis, the reassembled NMC particles were collected from acetonitrile and re-dispersed by sonication in DI water containing 1 M LiOH to replenish the lost cations in the electrophoresis. The suspension was then treated in a microwave hydrothermal reactor (Discover-SP, 300 W, 160 ^oC, 300 psi) for 30 minutes to improve the crystallinity of the reassembled particles.

4.2.6 Sintering

The LCO reassembled particles obtained after the microwave treatment were recovered using vacuum filtration, then annealed at 500 ^{o}C for 12 hours in air using an oven (Lindberg M, Thermal Scientific) to remove solvent and any residual organics or carbon as well as improve the crystallinity of the sample.

4.3 Results and Discussion

A primary goal of using oxidation-reduction assisted exfoliation is to avoid the introduction of protons. Also, the oxidation-reduction process simulate a charging-discharging process of battery, therefore, it lowers the risk of possible phase change brought by proton intercalation. The intercalation of TEA into NMC can be written as:

$$LiNi_{1/3}Mn_{1/3}Co_{1/3}O_2 \rightarrow (1\text{-}x)\ Li^+ + (1\text{-}x)\ e^- + Li_xNi_{1/3}Mn_{1/3}Co_{1/3}O_2 \quad (4.1)$$

$$TEA\text{-}OH \rightarrow TEA^+ + OH^- \quad (4.2)$$

$$4OH^- \xrightarrow{Ni} 2H_2O + O_2 + 4e^- \quad (4.3)$$

$$Li_xNi_{1/3}Mn_{1/3}Co_{1/3}O_2 + (1\text{-}x)TEA^+ + (1\text{-}x)e^- \rightarrow Li_x(TEA^+)_{1\text{-}x}Ni_{1/3}Mn_{1/3}Co_{1/3}O_2 \quad (4.4)$$

Overall reaction:

$$Li_xNi_{1/3}Mn_{1/3}Co_{1/3}O_2 + (1\text{-}x)TEA\text{-}OH \rightarrow$$

$$Li_x(TEA^+)_{1\text{-}x}Ni_{1/3}Mn_{1/3}Co_{1/3}O_2 + (1\text{-}x)/2H_2O + (1\text{-}x)/4O_2 \quad (4.5)$$

Equation 4.1 shows the charging process happening in NMC. In $LiNi_{1/3}Co_{1/3}Mn_{1/3}O_2$, the state of Co is same with the one in $LiCoO_2$, however the Ni and Mn is very different from $LiNiO_2$ and $LiMnO_2$. The valence of Ni, Co and Mn are +2, +3 and +4 respectively.[35] Ni^{2+} can be oxidized to Ni^{4+}, Ni^{2+}/Ni^{4+} redox is the major capacity source. For $Li_xNi_{1/3}Co_{1/3}Mn_{1/3}O_2$, when $2/3<x<1$, the materials undergoes Ni^{2+}/Ni^{3+} reaction.[35]

The redox position of $LiNi_{1/3}Co_{1/3}Mn_{1/3}O_2$ in our experiment is at 3.9 V vs Li/Li^+, which is different with ordinary $LiNi_{1/3}Co_{1/3}Mn_{1/3}O_2$ which has a redox potential at 3.7 V vs Li/Li^+. From previous work, this voltage is enough to oxidize OH^- group in the TEA solution. (Equation 4.3) It is unclear why this NMC has higher plateau than the normal ones. But from Figure 4.1, it worth noticing that the high (006) / (101) ratio from XRD of these NMC particles prove very high Li/Ni disorder. That should be responsible for the bad cycling and abnormal redox potentials.

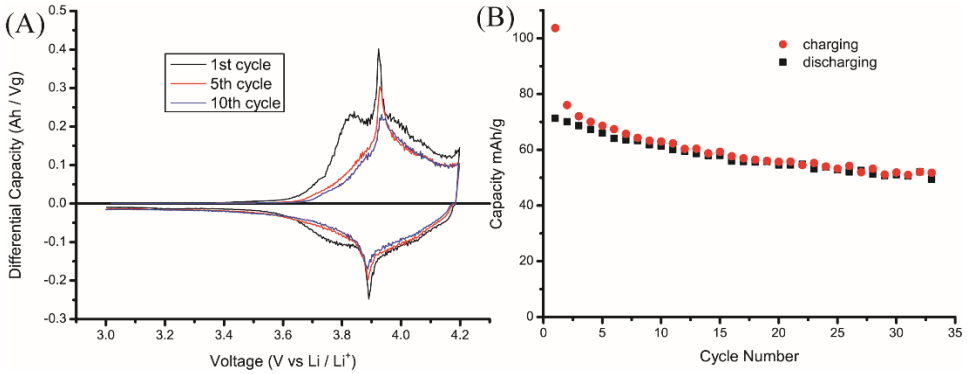

Figure 4.2 Cycling data of pristine NMC. (A) differential capacity and (B) cycling data.

After $Li_{0.43}Ni_{1/3}Co_{1/3}Mn_{1/3}O_2$ was achieved (Sample 2), it was also examined by XRD and ICP, and the result is shown in Figure 4.3 and Table 4.1. The position of (003) peak of oxidized NMC and $Li_{0.48}Ni_{1/3}Mn_{1/3}Co_{1/3}O_2$ are at 18.44° and 18.3° respectively. During this stage, the ratio of Ni/Mn/Co didn't undergo large composition change. It indicates that the NMC is not fully charged and the reason is the bad conductivity of NMC or high Li/Ni disorder. There are abnormal peaks at 36.5° and 64.5° in the oxidized samples, indicating the bad structure of original particles.

Table 4.1 Composition of NMC samples in different steps from ICP-OES results. The composition can be written as $Li_aNi_bMn_cCo_dO_2$. Sample 1 is the pristine $LiNi_{1/3}Mn_{1/3}Co_{1/3}O_2$, Sample 2 is the electrochemical oxidized $LiNi_{1/3}Mn_{1/3}Co_{1/3}O_2$, Sample 3 is the NMC nanosheets, Sample 4 is reassembled NMC particles through dialysis, Sample 5 is electrophoresis treatment on Sample 4, Sample 6 is sample 5 reacted with LiOH with microwave.

Materials	Li/a	Mn/b	Ni/c	Co/d
Sample 1	0.80	0.37	0.30	0.33
Sample 2	0.43	0.36	0.30	0.33
Sample 3	0.41	0.21	0.33	0.46
Sample 4	0.95	0.21	0.35	0.43
Sample 5	/	0.23	0.42	0.35
Sample 6	3.40	0.19	0.35	0.45

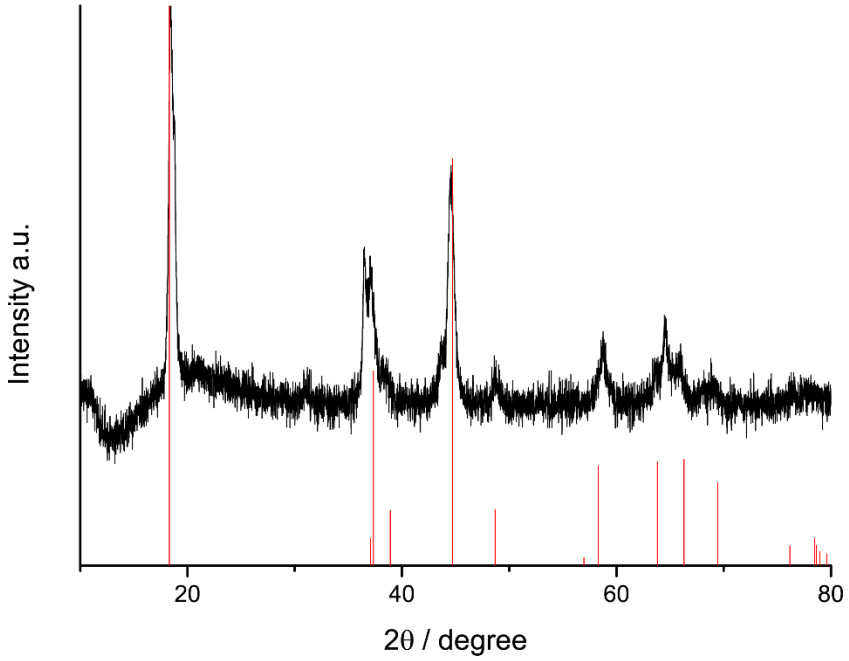

Figure 4.3 XRD of NMC particles after it was electrochemically oxidized.

The charged particles were washed and dispersed in TEA solution. TEA is known as strong alkaline and electrolyze to TEA ions which was used as big organic guest ions to insert into the matrix of NMC and OH^- provide electrons to charged NMC, (Equation 4.2) and finally Ni^{3+}/Ni^{4+} was reduced back to Ni^{2+} and TEA was inserted into the matrix of NMC and cause the exfoliation. To verify the exfoliation behavior, the concentration of TEA/Vacancy was set as 0.5, 1, 1.5, 2, 5, 10. After sonication and centrifuge to remove unreacted NMC particles, the solution dark red in color shows tyndall effect which is a sign of 2D nanosheets dispersion (Figure 4.4), this proves the successful exfoliation of NMC nanosheets in the range of 0.5-2. When the ratio of NMC/Vacancy is higher than 5, the exfoliation was hardly observed. The explanation is similar with LCO. If the concentration is too low, the amount of TEA is not enough for exfoliation; but when the

concentration of TEA is too high, the Ni^{2+} may transfer from transitional metal layer to lithium layer, thus block the intercalation of TEA^{+}.

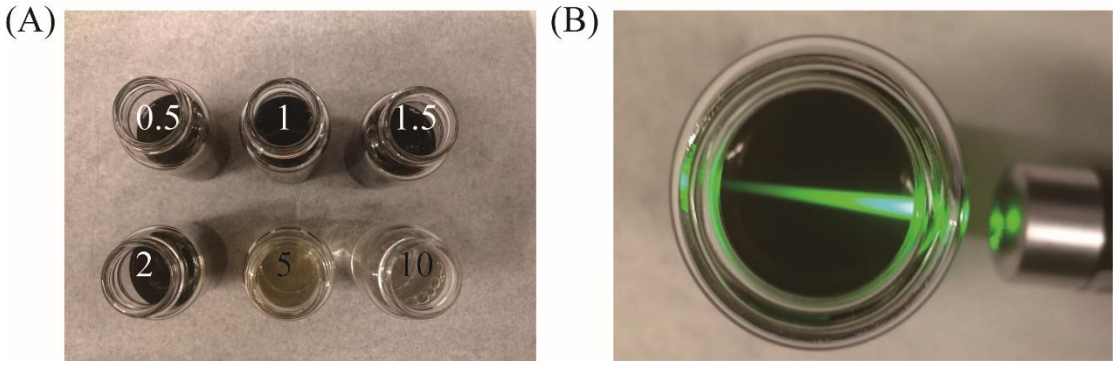

Figure 4.4 NMC nanosheets dispersion showing Tyndall Effect.

To further confirm the previous assumption, XRD were used to examine the unreacted particles in the decant (Figure 4.5). The results showed that these unexfoliated particles are very similar with pristine NMC. Due to the high Li/Ni disorder of pristine samples, it is highly possible that the parts of NMC with high Li/Ni disorder cannot be intercalated with TEA due to Ni^{2+} occupation in Li^{+} diffusion channel. Then these parts were left unexfoliated in the decant. The intercalation peaks are hardly observed, showing that there is intercalation happening in the charged NMC, but it is not enough for the exfoliation to happen. The composition of NMC nanosheets is $Li_{0.41}Ni_{0.21}Mn_{0.33}Co_{0.46}O_2$ (Sample 3). It is very interesting to notice that while lithium ions are still adsorbed on the surface of nanosheets, Large ratio of Mn ions were lose from the nanosheets. It is very well known that Mn has very strong John-Teller effect and Mn has solution problems in Li rich materials. During the exfoliation, large quantity of Mn octahedrals were contacted with solution, resulting in the Mn dissolve from nanosheets to aqueous solution.

Nanosheets samples were prepared for transmission electron microscopy (TEM) and atomic force microscopy (AFM) imaging by dropping the dispersion onto the respective substrates. Figure 4.6A shows the transmission electron microscopy (TEM) image of the exfoliated nanosheets. From the picture it can be clearly saw that NMC was exfoliated to form thin nanosheets. The hexagonal crystal lattice was verified by diffraction pattern (Figure 4.6B). The integrity of the basal plane indicates the exfoliation occurs along the layer stacking direction in the *c*-axis. The AFM and TEM shows that the sizes of NMC nanosheets is around 50 nm which is slightly smaller than LCO. This is due to the smaller radius of prisitine NMC particles (<500 nm, Sigma Aldrich, also shown in Figure 4.1) comparing with the large size of LCO (2 μm ~ 5 μm). Usually NMC particles were prepared through co-precipitate instead of solid state method, therefore the particles of NMC is aggregated by small NMC particles, thus the sizes of exfoliated NMC nanosheets are usually small. The high Li/Ni disorder is also the reason of limited size of nanosheets since the exfoliation cannot keep going once the Ni occupy the position of Li.

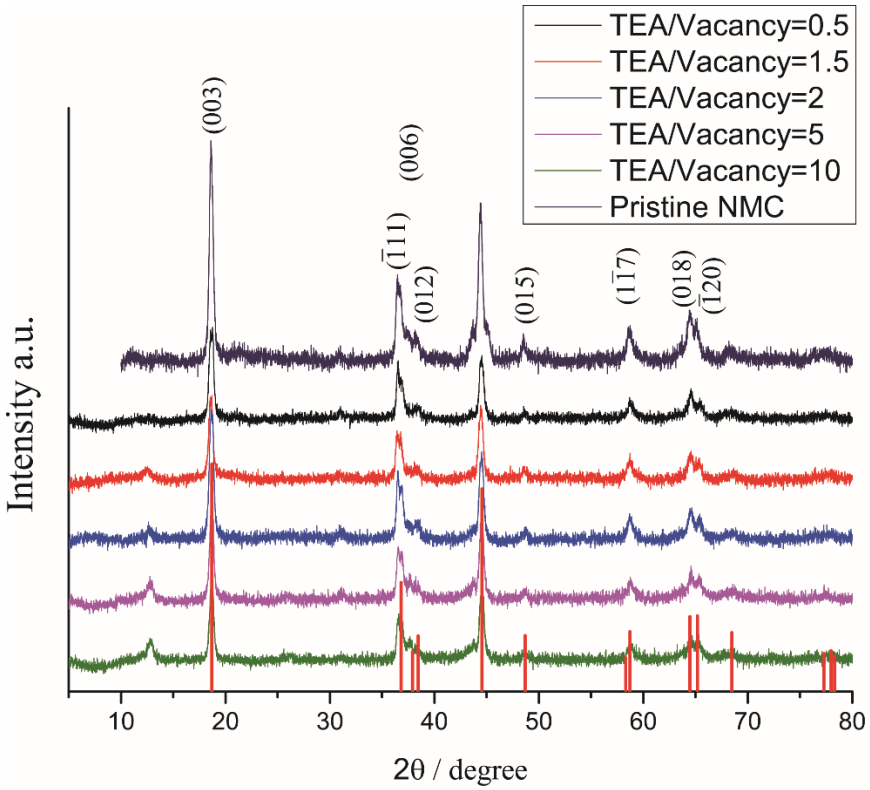

Figure 4.5 XRD of unreacted NMC particles in different concentrated TEA solutions. The ratio of TEA/Vacancy is 0.5, 1, 1.5, 2, 5, 10.

The thickness of the nanosheets was determined using AFM (Figure 4.6 C &D). The nanosheets were collected from decant after centrifuge at 13000 rpm, then it was dispersed in isopropyl alcohol and dropped onto clean polished Si substrate which was cleaned by bath sonication in DI water, acetone and isopropyl alcohol respectively. Our results shows the lateral dimensions of NMC nanosheets is from 0.7 to 2 nm, which is consistent with our previous investigation of cobalt oxide nanosheets of which has a thickness around this range. And this comparable results show that NMC was successfully exfoliated into monolayer or dual-layer nanosheets.

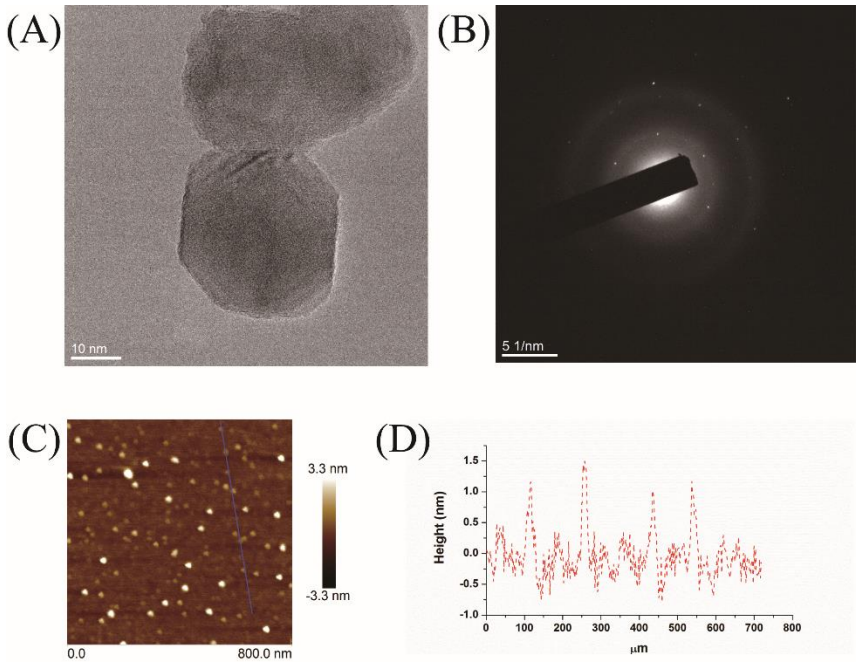

Figure 4.6 (A) TEM of exfoliated NMC nanosheets and (B) the diffraction pattern. (C) AFM of exfoliated NMC nanosheets and (D) the height profile.

With TEM and AFM results confirming that the NMC was successfully exfoliated, the nanosheets were reassembled back into NMC particles to demonstrate that they can serve as functional building blocks for new cathode materials. First, the NMC nanosheet dispersions in the TEA solutions were dialyzed in 1 M $LiNO_3$ solution for 1 day to reassemble NMC nanosheets with electrostatic force. Different from the reassembly of LCO in last chapter, TEA^+ ions were not removed using electrophoresis first in this case. Given to the fact that electrophoresis is very effective on the removal of TEA^+, if the electrophoresis was utilized on big reassembled particles, the removal of TEA^+ ions which glue negatively charged particles/sheets together will dissociate the large reassembled particles (1μm ~ 5 μm in diameter) to much smaller nanoparticles. During this dialysis process, the TEA^+ ions slowly diffuse out of the nanosheet dispersion while

Li^+ ions diffuse in. Due to the negatively charged surface of the NMC layers, the presence of Li^+ will cause flocculation. As a result of the slow diffusion of ions during dialysis, the nanosheets can restack and grow under a slow and controlled rate. Comparing with direct flocculation, particles reassembled by dialysis should have better crystal match between different nanosheets.

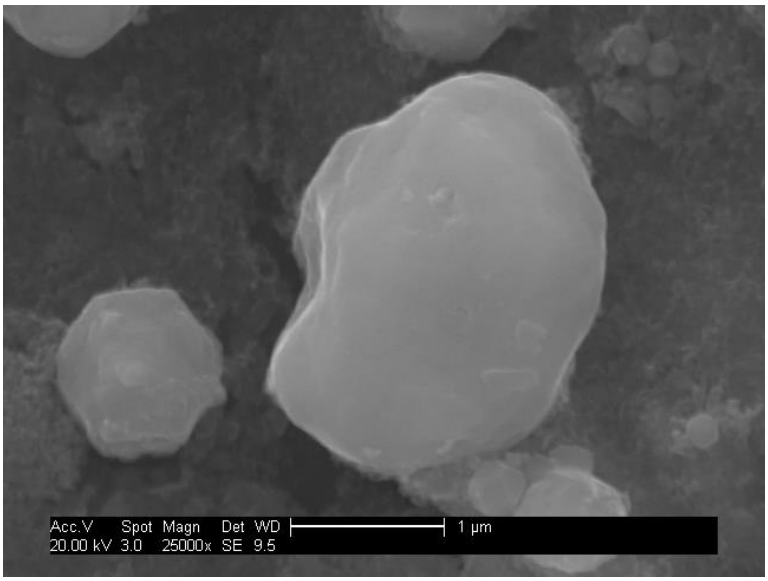

Figure 4.7 Reassembled NMC nanosheets by dialysis with 1 M $LiNO_3$.

However, due to the electrostatic force, the size of reassembled particles is uncontrollable and will grow into larger sizes than they should be (Figure 4.7). According to our previous work, the reassembled LCO didn't show very ideal electrochemical properties. The reason is the existence of TEA guest ions which highly limits the electrical conductivity of inside particles in the reassembled particles. Another reason is probably because the large amount of dislocations and grains existing in the larger LCO particles (> 10 μm) due to the reassembly of small sizes of nanosheets. These dislocations and grains would cause the lower electron conductivity and trouble of conducting lithium

ions, even the collapse of the whole LCO reassembled particles during the cycling. However, if the particles were reassembled simultaneously through electrostatic force, either dialysis, or direct flocculation in lithium ion solution, would always agglomerate to very large sizes.

How to control the sizes of reassembled particles? The sizes of nanosheets of NMC is around 50 nm ~ 100 nm. That means if it was reassembled to a spherical shape, the final diameter should also in this range. These smaller particles which is still negatively charged was glued together under the electrostatic force of TEA^+. The structure is like house of cards which usually happens in the reassembly of nanosheets.[86] Due to the large sizes of TEA^+, the junction of nanosheets that were connected by TEA^+ is not compact. Therefore, it is reasonable to speculate that if we can remove the TEA^+ from big particles through strong electro-static force, the big reassembled particles can be ripped apart just like the collapse of house of cards and back into small nanoparticles, then the problem of dislocations/grains can be solved.

To verify this thought, NMC nanosheets were reassembled first in 1 M $LiNO_3$ solution through dialysis, then the reassembled particles was separated through centrifuge and dispersed in acetonitrile through sonication. At last the NMC-acetonitrile dispersion was treated with electrophoresis under 30 V DC. After electrophoresis the dispersion were dropped onto Cu grid for TEM characterizations.

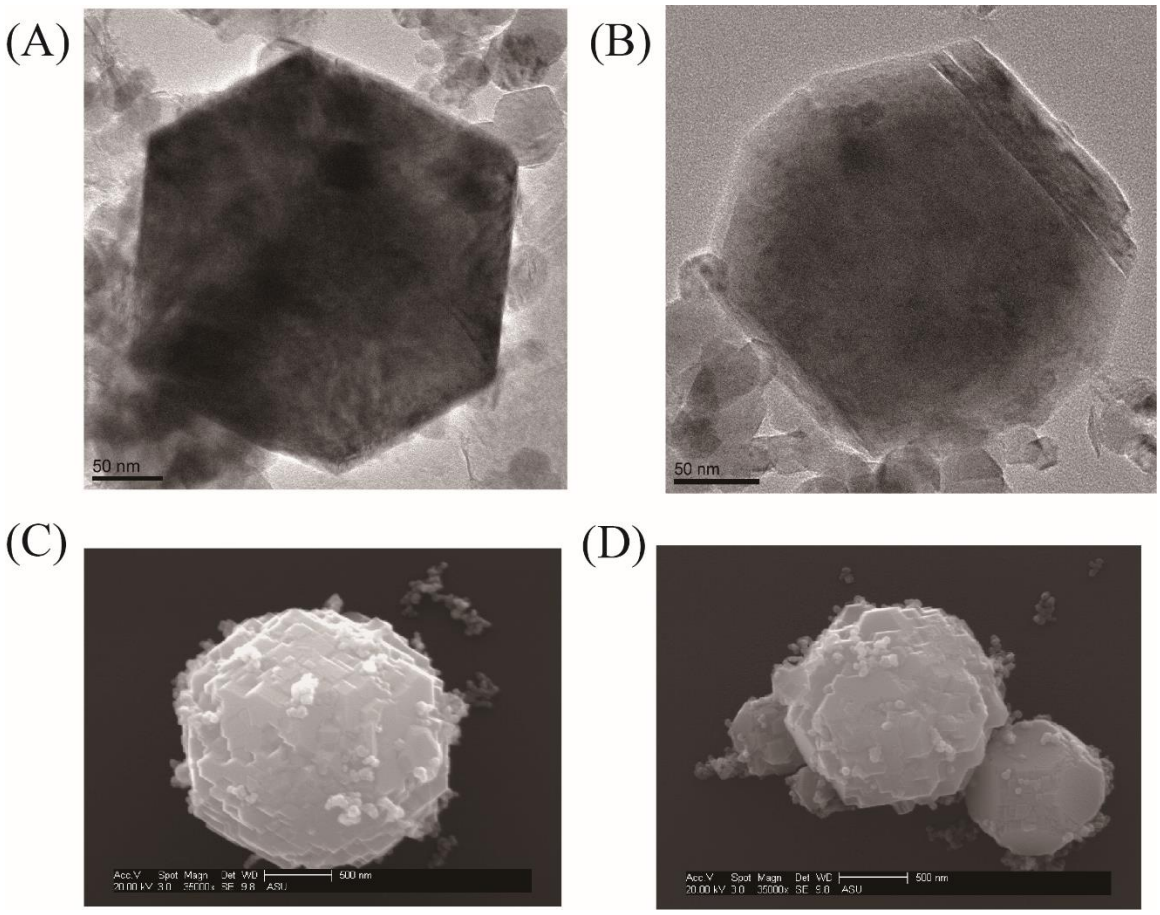

Figure 4.8 TEM and SEM images of small NMC hexagonal particles found after electrophoresis.

Both TEM and SEM in Figure 4.8 shows these particles has a very uniform hexagonal shapes. It can be clearly saw that the large particles were unveiled as nanoparticles after strong electrical field in the electrophoresis. It is interesting to notice that these nanosheets would grow into an exterior shape that is similar with its basal structure. The diffraction patterns of these reassembled particles show very good crystallinity (Figure 4.9), which prove that these reassembled particles are highly oriented with same direction. During the reassembly, the nanosheets may automatically choose the direction with

lowest energy, close packing in this case, then grow to a suitable size of nanosheets. This theory can be proved by the SEM (Figure 4.8 C&D) Therefore, reassembly controlled by dialysis is a perfect way to reassembled particles back into the integrities.

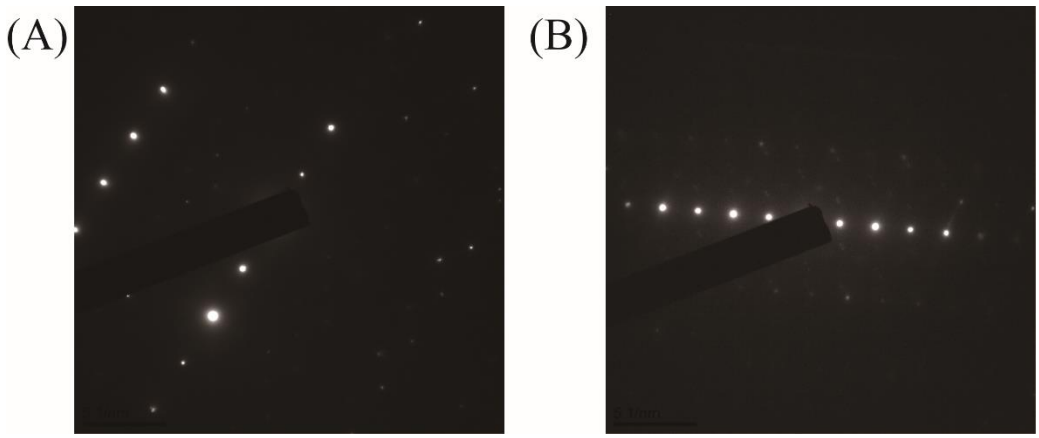

Figure 4.9 Diffraction patterns of NMC reassembled nanoparticles.

From ICP results, most of the lithium ion adsorbed on the nanosheets are removed from nanosheets in the electrophoresis (Sample 5). The nano-particles were further treated with microwave at 160^{o}C for 30 minutes to replenish lithium back into structure. Then the reassembled particles were sintered at 500 ^{o}C for 12 hours, the particles were dispersed in NMP by sonication, then mixed with carbon black and PVDF with a ratio of 8:1:1. Finally it was drop-casted onto Al foil and dried under 120 ^{o}C overnight. From Figure 4.10A, the NMC reassembled particles maintained as nanoparticles, which successfully avoid the previous problem. The cycling is not ideal, but both cycling and capacity retention are recovered to the level of pristine NMC particles.(Figure 4.10B) Further research would be on the exfoliation of better NMC and improvement of capacity and capacity retentions.

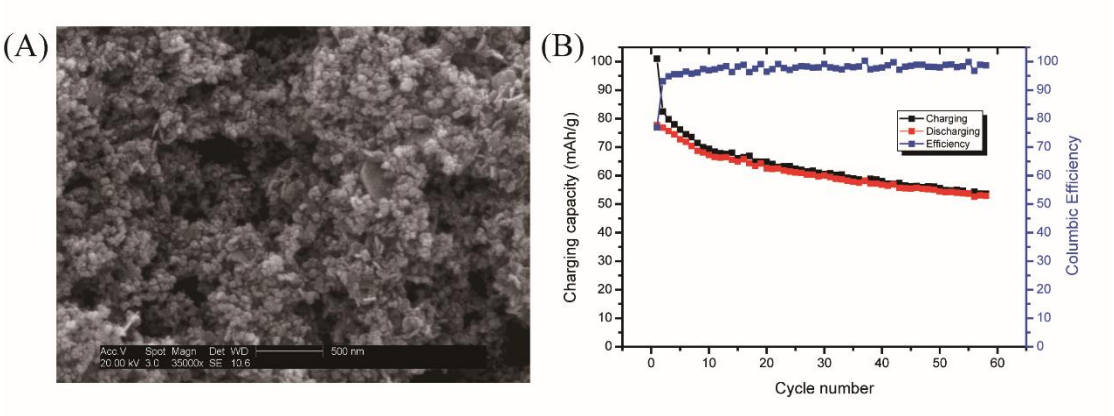

Figure 4.10 (A) morphology of NMC reassembled particles after microwave and (B) capacity retention and columbic efficiency of NMC particles.

4.4 Conclusion

The oxidation-reduction assisted exfoliation method was successfully used to obtain NMC nanosheets by exfoliation of $LiNi_{1/3}Mn_{1/3}Co_{1/3}O_2$. In order to control the sizes of NMC reassembled particles, purification of the nanosheets was performed with dialysis first, then TEA was further removed using electrophoresis, which controlled the nanosheet reassembly into hexagonal crystalline nanoplates. After microwave the NMC reassembled particles have recovered its original electrochemical properties. This methodology can be applied to control the sizes of reassembled particles to make functional nanosheets and novel Li-ion battery materials.

5 FOLDABLE LITHIUM ION BATTERY FOR HIGHER AREAL CAPACITY

5.1 The Device Architecture of Lithium Ion Batteries

Lithium ion batteries can be classified as cylindrical cells, prismatic cells and coin cells by the shape. Prismatic cells can save more space compared with the other kinds. An actual lithium ion battery consists of components than just the cathode and anode materials. Figure 5.1 shows a cross-section view of the components inside a typical commercial prismatic Li-ion battery:

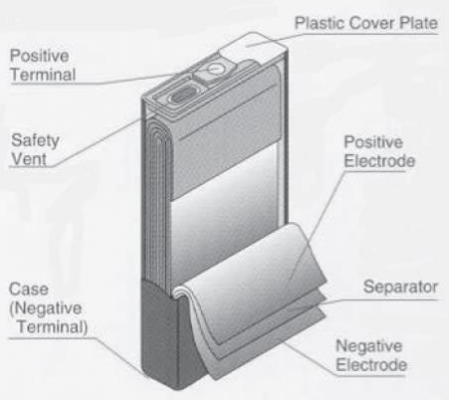

Figure 5.1 Schematic drawing of a prismatic cell (Japan Storage Battery Co., Ltd)

1. Active materials: the core of a battery. They store and provide energy through electrochemical reactions.
2. Conductive additives: usually carbon black or graphite. They provide enough electrical contact between the active material particles and current collector.
3. Binder: a polymer. It is used to attach active materials and conductive additives onto the current collector.

4. Current collector: metal substrate that collect charges from the active materials and delivers them to the terminals. For lithium ion batteries, Al and Cu are usually used as cathode and anode current collector respectively; the surface of Al can be oxidized and form a dense layer of Al_2O_3 which can resist corrosion. Cu has very good electronic conductivity and doesn't form alloys with lithium.

5. Separator: insulating material used to avoid a short circuit between anode and cathode; at the same time, it has to allow the passage of the lithium ions. The separator also needs to have good mechanical properties to prevent any possible penetration induced by the growth of lithium dendrites. Common separators are polyethylene and polypropylene.

6. Electrolyte: ionic medium that enables Li ions to shuttle between the two electrodes. Due to the strong reducing power of lithium metal, organic solvents such as propylene carbonate and ethylene carbonate are required. Solutes are usually $LiPF_6$, $LiClO_4$ and $LiBF_4$.

7. Case / positive terminal / negative terminal: prevent the inside materials from air, and provide the interface to the outside circuits.

8. Vent: release the gas to avoid safety problems brought by pressure buildup.

Since it has been difficult for battery researchers to find anode and cathode materials with significantly higher capacities, minimizing the weight of inactive components in the battery can also lead to improvements in energy density. During the past 20 years, the improvement of energy density in lithium ion batteries mainly comes from lightening the inactive parts, which still occupy most of the mass in nowadays batteries. Taking the well-known 18650 batteries which are widely used in laptops as an example (Aosibo

18650 2500 mAh flat top battery): this battery has a capacity of 2500 mAh and weight of 44.5 g. The theoretical capacities of $LiCoO_2$ and graphite are 140 mAh/g and 398 mAh/g, respectively. The total mass of active materials can be easily calculated as:

$$(2500/140 + 2500/398) = 24.14 \text{ mg}$$

The ratio of active materials versus the entire battery is:

$$24.14/44.5 = 54.24\%.$$

For conventional Li-ion batteries, aluminum and copper foils are used as the current collectors for the cathode and anode respectively, which are heavy (2.7 g/cm^3 for Al and 8.96 g/cm^3 for Cu). In prismatic cells, the active materials are coated on either side of the metal foil as thin coatings and the electrodes are separated by polymeric separators to avoid short-circuits. However, the coatings must be thin (< 200 microns) due to slow Li-ion diffusion through the electrode materials of ca. 10^{-10} m^2/s. Thicker electrode also induce deterioration of capacity and cycling capability, accompanied by the loss of energy density.[87] This limits the areal energy density (Wh/cm^2) of Li-ion batteries since the capacities of the electrodes cannot be increased by simply making thicker electrodes, which is a good way to improve the ratio of active materials.

5.2 Folded Cells to Compact Power

To address problems of heavy inactive components and limited areal capacity, we developed a paper-based Li-ion battery that makes use of carbon nanotube (CNT) coated paper electrodes as the current collectors. Recently, there has been much interest in the development of electronic and energy storage devices using paper and textile

components.[88] The low cost, roll-to-roll fabrication methods, flexibility, and bendability of these substrates are attractive for high-performance devices. Many flexible devices demonstrated using paper or cellulose components include organic field effect transistors,[89] RF devices,[90] sensors,[91, 92] microfluidics,[93-95] displays,[96] transparent conducting films,[97] and light-emitting diodes and three-dimensional (3D) antennas.[98] Specifically for energy storage and conversion applications, the ability for the power source to be intimately integrated to unconventional substrates has motivated research in paper-based flexible devices such as batteries,[99, 100] supercapacitors,[101, 102] nanogenerators,[103] solar cells,[104] and fuel cells.[105, 106] The CNTs impart electrical conductivity to the paper and are coated onto the paper from dispersions containing surfactant and binder. The CNT-paper substrates offer the following advantages:

1) Significant weight and cost savings over the metal foil current collectors; Li-ion batteries using the CNT-paper electrodes to replace the Al and Cu current collectors can offer substantial savings in weight. These savings arise from the lower density of paper, therefore, it helps improve the energy density. Table 5.1 compares the areal density and thickness for the CNT-papers compared to Al and Cu foil. As we did not screen a large variety of papers in the proof-of-concept, the paper thickness can also be further optimized.

Table 5.1 The weight and thickness parameter of different current collector

Material	Areal density (mg/cm^2)	Thickness (microns)
Aluminum foil	4.13	18
Copper foil	15.06	17
CNT-Paper	2.42 (CNT-paper total) 0.7 (CNT mass loading)	26

2) permeability to the electrolyte due to the porous nature of the paper, which enables double coating of active material layers without requiring extra layers of separator; (Figure 5.4)

3) better adhesion with active materials;

4) deformability including flexing and folding, which enables the areal energy density to be increased without increasing the thickness of the active material layers. The art of paper folding has recently been applied to impart compactness and 3D morphologies to devices such as telescope lenses,[107] microfluidic sensors,[93, 108] complex functional structures,[109, 110] as well as actuators and robots.[111, 112] The use of paper as substrates for Li-ion battery electrodes creates a natural opportunity to exploit paper folding to achieve energy storage devices with higher areal energy density using conventional active materials.

5) The CNT paper is soft and help prevent the possible safety issue brought by the messy edges of metal current collector.

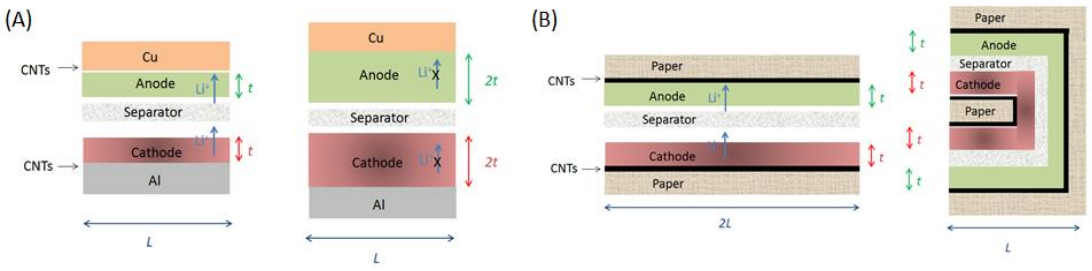

Figure 5.2 (A) Conventional electrodes must increase thickness (t) of active materials to increase the areal capacity. For simplicity, only single-side coated electrodes are shown; (B) Paper-based electrodes can be folded to increase the energy density with multiple layers rather than thicker electrodes.

These properties make the paper-electrodes particularly suitable for applications where high energy density in a small footprint area is desired. Specifically, since the electrical conductivity of CNT-films does not decrease upon folding, a planar electrode consisting of active material coated on the CNT-paper substrate can be folded to increase the energy density within a given area. This concept is illustrated in Figure 5.2. As shown in Figure 5.2A, increasing the thickness of the active material layer in a conventional electrode (from *t* to 2*t*, for example) to increase the areal energy density (from *E* Wh/cm^2 to 2*E* Wh/cm^2) results in Li-ion transport limitations, which will ultimately reduce both the battery capacity and rate performance. On the other hand, the foldability of the paper-based electrodes enables the dimensions to be elongated (from length L to 2L) and then folded to achieve 2*E* Wh/cm^2 without increasing the active material thickness, *t*, as illustrated in Figure 5.2B. Our attempts to fold conventional, metal foil based electrodes revealed delamination of active material and cracking at the creases, as shown in Figure

5.3A. In contrast, there is no indication of delamination of active material or cracking when the paper-based electrodes are folding, as shown in Figure 5.3B.

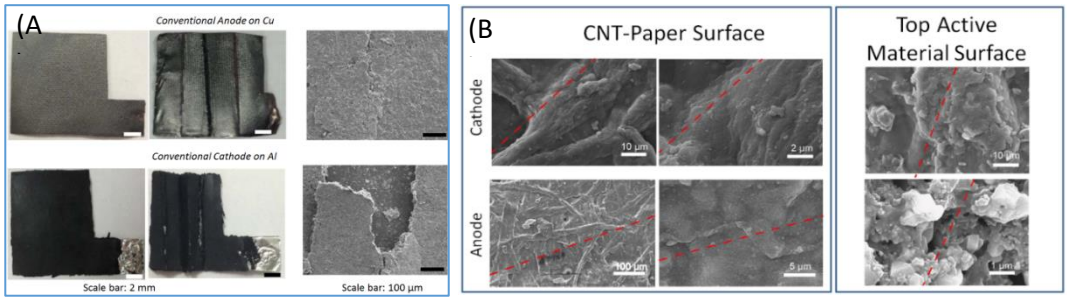

Figure 5.3 Effect of folding on electrodes based on (A) conventional metal foils, (B) CNT-paper

If considering only the anode and cathode composites (typically 8:1:1 by weight of active material to conducting carbon to binder) coated on the metal foils, replacing the Al and Cu with the CNT-coated papers would decrease the weight of the electrodes by 16.6%. However, if considering the entire battery, including the electrolyte, separator, and other inactive components, the weight savings is decreased, since the active materials only constitute ca. 53.3 % of the total mass of the battery. However, the CNT-papers also enable the elimination of a layer of separator, one of the most expensive components of the battery (ca. 20% of the total cost). As shown in Figure 5.4A, when the electrodes are rolled (wound) in a prismatic or cylindrical cell, additional separators are required to prevent the double-sided coated current collectors from short-circuiting. The extra thickness from the separator layers decreases the volumetric energy density of the battery and also limits the number of winds that can be achieved. In contrast, by folding the

paper-battery using an “accordion” fold as shown in Figure 5.4B, the extra separator layers are not needed since Li-ions can diffuse through the porous paper electrodes. The negligible diffusion of Li through Al and Cu metal is an inherent limitation of conventional electrodes.

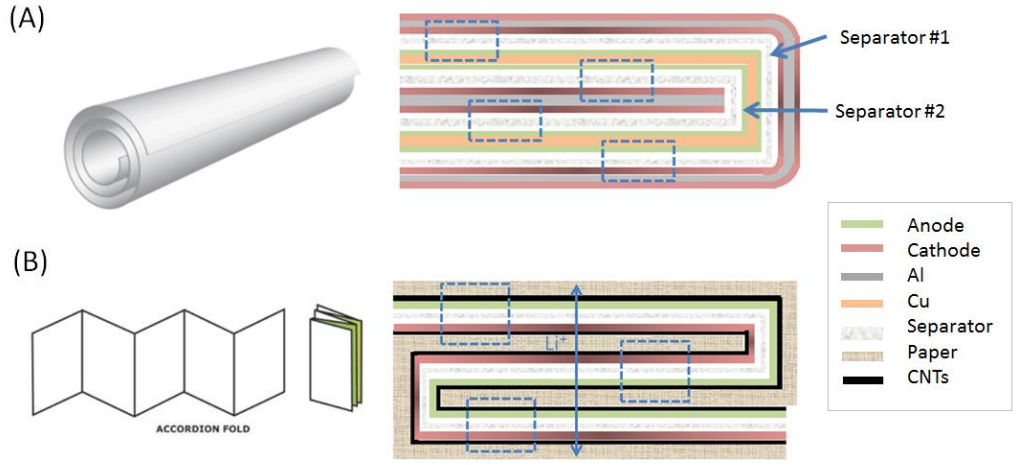

Figure 5.4 Comparison of cross-sections of (A) rolled and (B) accordion folded battery layers. The anode/separator/cathode stacks are indicated with the dotted boxes. More than one separator is needed in the rolled battery, while the same separator is folded in the accordion battery. Only the paper-based electrodes can be folded in the accordion style since Li^+ ions can diffuse through the pores of the paper.

The amount of improvement in energy density using the paper battery can be estimated with a simple calculation. For a 10 Wh battery with dimensions of 0.45*3.8*10 cm (commercial battery), to simplify the calculation, only the anode / cathode / separator were considered. Table 5.2 presents some basic characteristics for a typical lithium ion

battery. For a single layer battery, the areal capacity is 3 mAh / cm^2; then the capacity of a single layer is:

$$C_{single} = C_{areal\ capacity} * area = 3\ mAh / cm^2 * (10\ cm * 3.8\ cm) = 114\ mAh.$$

The number of layers can be calculated as:

$$N = C_{total} / C_{single} = (10\ Wh / 3.7\ V) / 114\ mAh = 23.7$$

3.7 V is the average voltage of a $LiCoO_2$ / graphite lithium ion battery. The battery needs at least 24 layers in order to have a total capacity of 10 Wh.

Table 5.2 Specifications for Li-ion battery volumetric energy density calculation *Graphite anode assumed to undergo 10.5% volume expansion

Anode	Current collector thickness	6 μm
	Capacity	320 mAh/g
	Active layer thickness*	65 μm
	Active material ratio	90 wt%
	Density	1.5 – 1.6 g/cm^3
	Areal loading	9.5 – 9 mg/cm^2
	Areal capacity	3 mAh/cm^2
Cathode	Current collector thickness	6 μm
	Capacity	140 mAh/g
	Active layer thickness	60 μm
	Active material ratio	88 wt%
	Density	4 g/cm^3

	Areal loading	24 mg/cm^2
	Areal capacity	3 mAh/cm^2
Separator	Thickness	25 μm

For a battery of 24 layers, we need 24 layers of active materials (LCO + Graphite), 24 layers of separator, 12 layers of Al foil and 13 layers of Cu foil.

The total thickness:

$$24 * (65 + 60 + 25) + 12 * 6 + 13 * 6 = 3750 \text{ μm}.$$

Graphite has 10.5% thickness expansion during lithiation but LCO is considered to have a stable volume, then the final thickness would be:

$$3750 + 10.5\%*24*65 = 3913.8 \text{ μm}$$

The volumetric energy density of the battery using conventional current collectors, without including the battery packaging is:

$$\frac{24*114*3.7}{38*0.39138} = 680.668 \text{ Wh/L}$$

The same calculations can be performed when changing to the CNT paper battery, assuming the thickness of the CNT paper is 6 μm.

For a battery of 24 layers, we need 24 layers of active materials (LCO + Graphite), 12 layers of separator, and 24 layers of CNT paper.

The total thickness is then:

$$24 * (65 + 60) + 12*25 + 24*6 = 3444 \text{ μm}.$$

Taking into account the 10.5% thickness expansion in graphite:

The final thickness would be $3444 + 10.5\%*24*65 = 3607.8$ μm

$$\frac{24*114*3.7}{38*0.36078} = 738.4 \text{ Wh/L}$$

The improvement in volumetric energy density by using the CNT paper substrates is:

$$\frac{738.4-680.668}{680.668} = 8.33\%$$

If all the parts were considered, using a Panasonic prismatic battery as an example (model number UF103450P, 2000 mAh, 4.88 cm x 3.38 cm x 1.05 cm, mass: 38.5 g), the mass savings can also be calculated.

Table 5.3 The % weight ratio of the whole battery

Parts	Weight (g, normal battery)	Weight (g, folded battery)
Can	7.6	7.6
Header	1.218	1.218
Graphite	5.625	5.625
Current collector	7.395	2.266
LCO	12.85	12.85
Electrolyte	4.116	4.116
Separator	2.1	2.1

The mass distribution was calculated to be divided as shown in Table 5.3 and Figure 5.5A. Replacing the Al and Cu with the CNT-paper results in a 12.4% weight savings, as shown in Figure 5.5B.

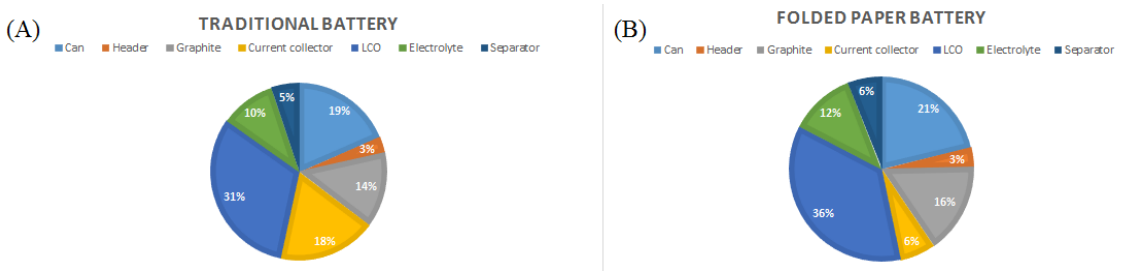

Figure 5.5 The ratio of each composition in Lithium ion battery (A) traditional battery and (B) CNT folded battery.

In summary, these calculations show that the CNT coated paper substrates can impart both volumetric and gravimetric energy density improvements, in addition to the advantages from having the capability to use folding to introduce new battery designs. The next section describes the methods to realize the CNT paper batteries and characterization of the performance.

5.3. Experimental Methods

CNT inks were prepared with 4 mg/mL single-walled carbon nanotubes (P3, Carbon Solutions) and 8 mg/mL sodium dodecylbenzenesulfonate (SDBS, Sigma-Aldrich). The CNT ink was sonicated for 25 minutes to obtain a uniform dispersion. Afterwards, the paper was soaked in the CNT ink solution to ensure that the CNTs would be distributed uniformly on the surface and within the paper pores. The CNT-coated paper was then dried with a heat gun set to 200 ^{o}F (93 ^{o}C). The soaking and drying process was repeated 13-15 times followed by washing with deionized water and ethanol three times each to obtain a sheet resistivity as low as 5 Ω/square. The resistance was around 6-8 Ω between the two sides of the CNT-coated paper. Effective washing to remove excess surfactant

was needed to improve the conductivity of the CNT-coated papers. The amount of material deposited was determined by measuring the mass of the paper before and after coating/drying using an ultramicrobalance (Mettler-Toledo UMX2).

To add the PVDF binder and improve the cycling behavior, 3 mg/mL of CNT solution was sonicated in N-methyl-2-pyrrolidone (NMP) containing 6 mg/mL of PVDF for 30 min to prepare a CNT/PVDF slurry. This slurry was coated on both sides of CNT-coated papers followed by drying at 120 ºC on a hot plate. Then, the CNT-coated paper was placed on a piece of Al or Cu foil and soaked with NMP at 60 ºC for half an hour in order to dissolve and redistribute PVDF from the surface CNT layer throughout the entire CNT-coated paper. Afterwards, the CNT/PVDF-coated paper was dried at 120 ºC for 4 hours. The paper can also be dried at 60 ºC for 10 hours, after which it would display strong adhesion to the metal foil substrate.

5.4 Results and Discussion

As a proof-of-concept, we have chosen to apply simple paper folding as well as the more complicated Miura-ori pattern to paper-based Li-ion battery electrodes. Miura folding consists of dividing a sheet into parallelograms with interdependent folds and has been used to fold maps,[113] solar panels,[113, 114] and recently, metamaterials.

Li-ion batteries were prepared based on the methods established by Hu, et al.[115] using carbon nanotube (CNT) coated papers as the current collectors and depositing conventional active material layers on top of them. Laboratory Kimwipes (Kimtech Science, Kimberly-Clark) were used as substrates because the thin and porous nature of the paper allowed the CNT ink to diffuse easily both inside and outside of the paper. This

resulted in CNT-coated papers that were conductive on either side. Figure 5.6A shows a photograph of a CNT-coated paper. Figure 5.6B shows the scanning electron microscopy (SEM) image of the surface of the CNT-coated papers, showing the CNTs formed ropes, and were uniformly distributed on the surface of the paper.

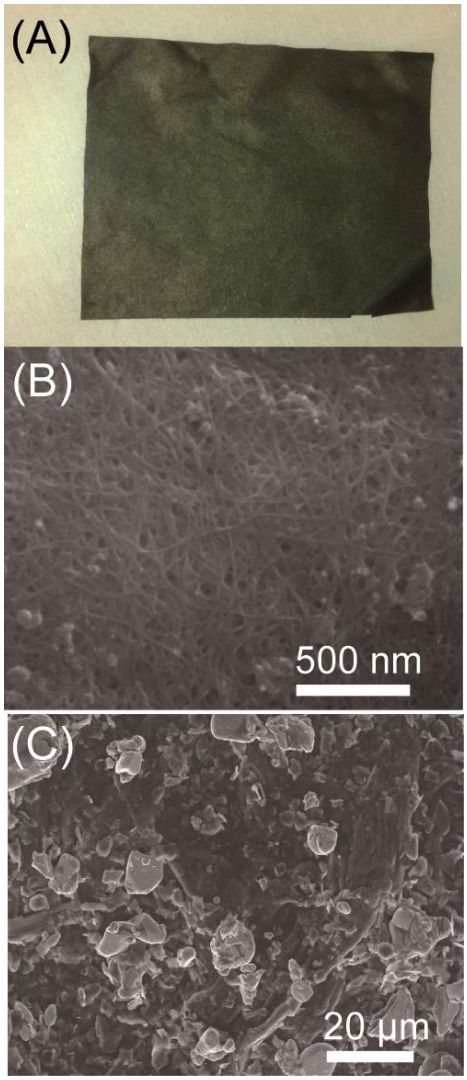

Figure 5.6 (A) Photograph of CNT-coated paper with dimensions of 6 cm x 7 cm. Scanning electron microscope images of (B) Surface of CNT-coated paper, (C) CNT-coated paper with $LiCoO_2$ active material.

To check if the CNT-coated papers would exhibit any reversible capacity, half-cells were prepared using Li metal as counter electrode and 1 M $LiPF_6$ in EC/DMC/DEC (4:2:4) as electrolyte (MTI Corp). A piece of Cu foil was placed under the CNT-coated paper as an additional current collector and it was tested from 1.7 to 1.2 V versus Li/Li^+ at 25 mA/g as an anode control test (Figure 5.7A). For the cathode control test, a piece of Al was used as an additional current collector and it was tested from 2.8 to 4.2 V vs Li/Li^+ at 25 mA/g (Figure 5.7B). As shown in Figure 5.7C, the CNT-coated paper had a charge capacity of 0.054 mAh/cm^2 in the first cycle, but this decreased to ~1 $\mu Ah/cm^2$ in subsequent cycles. This irreversible capacity loss can be due to solid-electrolyte interphase formation on the CNTs. The CNT-coated paper showed a capacity of ~0.01 mAh/cm^2 in the potentials relevant for a cathode (Figure 5.7D). These results are consistent with previous reports.[88]

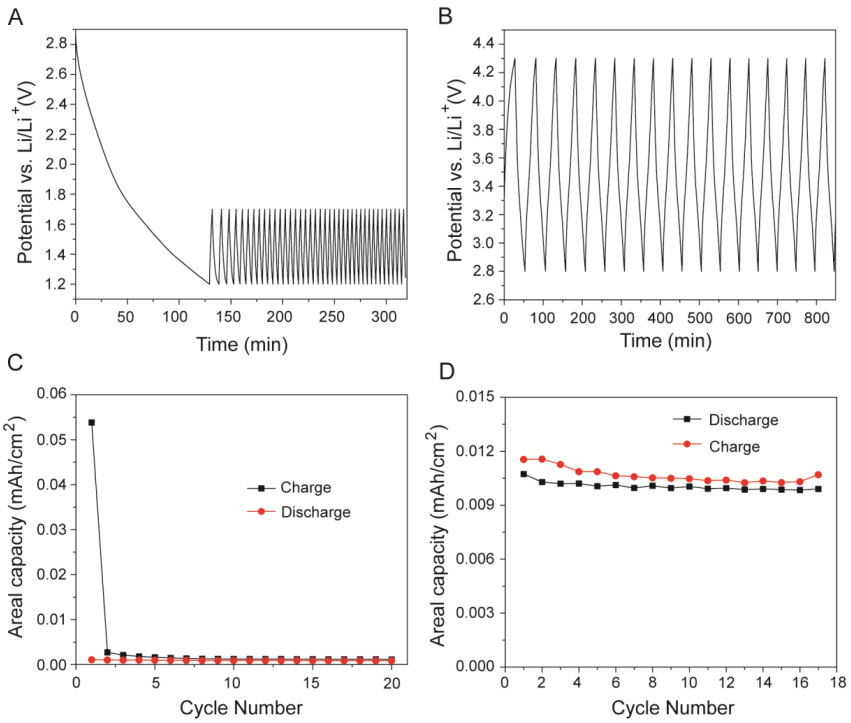

Figure 5.7 Cycling of CNT-coated papers in half-cells using 25 mA/g. (A) and (B) are the voltage profiles, (C) and (D) are the areal capacity vs. cycle number. (A) and (C) are for cells cycled in the same range as the LTO anode, (B) and (D) are for cells cycled in the same range as the LCO cathode.

$LiCoO_2$ (LCO, Sigma-Aldrich) and $Li_4Ti_5O_{12}$ (LTO, MTI Corp.) were chosen as cathode and anode materials, respectively. Slurries were prepared by mixing the active materials, carbon black (Timcal Super C45) and binder (PVDF, MTI Corp.) with a ratio of 8:1:1.3 by weight. The slurry was uniformly coated on the CNT-coated paper using doctor blading, followed by drying on a hot plate at 120 °C for 5 h. A piece of Cu or Al foil was used as metal backing layer to supplement the CNT/PVDF-coated paper current collector. Figure 5.6C shows a typical SEM image of the active material composite (in this case, LCO) on the CNT-coated paper. The LTO electrodes also looked similar.

Despite the low sheet resistivity, electrodes prepared using the CNT-coated paper as the substrate showed large capacity decay upon cycling in half-cells, particularly for the LCO half-cell (Figure 5.8A-B).

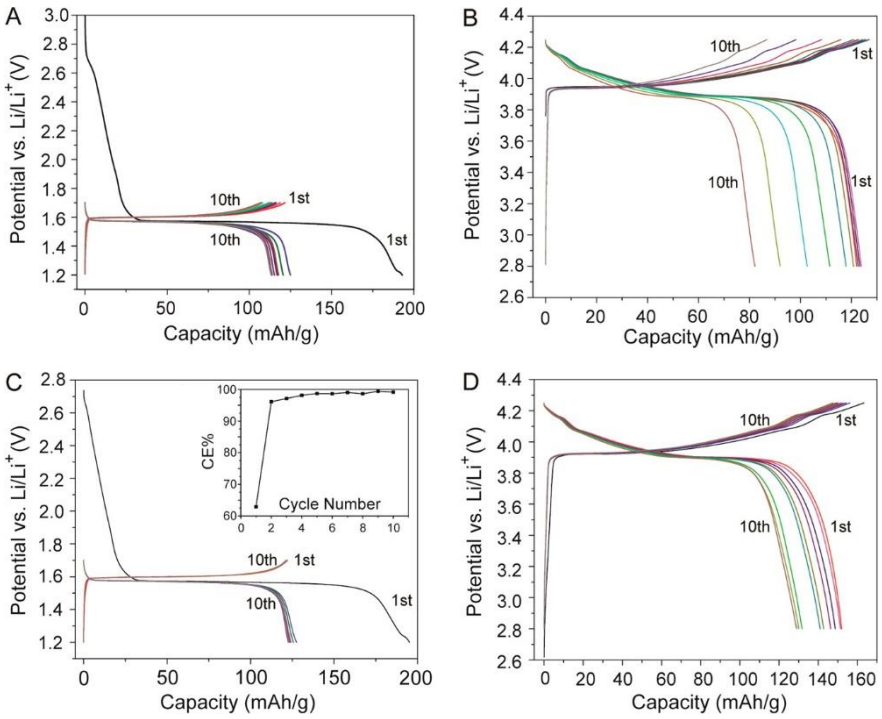

Figure 5.8 Cycling results for half-cells using 25 mA/g. (A) LTO on CNT-coated paper, (B) LCO on CNT-coated paper, (C) LTO on CNT/PVDF coated paper, insets shows the Coulombic efficiency versus cycle number, and (D) LCO on CNT/PVDF-coated paper.

Since the control tests showed some capacity in the cathode potential range (Figure 5.7D), there can be some Li^+ insertion in between CNT ropes that may cause them to lose contact with each other, the LCO particles, or the paper fibers during the electrochemical cycling, resulting in the capacity decay.

To address this, polyvinylidene difluoride (PVDF) was used as a binder to improve the CNT adhesion by coating an additional CNT/PVDF layer onto the CNT-coated papers

prior to depositing the active materials. The final mass loading of CNTs on the paper was around 0.7 mg/cm^2. The sheet resistivity of the papers increased from 5 to 10 Ω/square with addition of the PVDF. However, the final CNT/PVDF-coated papers showed good conductivity that would not change upon creasing or wrinkling.

The electrochemical cycling results of half-cells prepared with the CNT/PVDF-coated papers using a current of 25 mA/g are shown in Figure 5.8C, D. The capacity retention for the anodes and cathodes was improved using the PVDF binder on the CNT-papers and the discharge capacities were higher for LCO deposited on CNT/PVDF-papers (152 mAh/g in the first discharge compared to 122 mAh/g without the additional PVDF). The LTO anodes showed low Coulombic efficiency (CE) of 63% on the first cycle in half-cells regardless of the presence of additional PVDF (Figure 5.8A, C). After the first cycle, the LTO electrode on CNT/PVDF-coated paper showed higher CE of 97–99% (Figure 5.8C, inset) and good capacity retention. This suggests that the irreversible capacity loss can be due to solid-electrolyte interphase formation or other side reactions, such as with the functional groups on the CNTs, but that they were largely absent after the first charge. Therefore the LTO electrodes were assembled in half-cells and cycled once to remove irreversible capacities. After that, the half-cells were disassembled and the LTO electrodes were assembled in full cells. A mass ratio for LTO/LCO was around 1.5 to ensure enough anode material to prevent Li dendrite formation from overcharging.

In order to understand the effect of folding on the electrochemical characteristics of the electrodes, the films were folded as shown in Figure 5.9A. A planar, unfolded cell (2 cm × 2 cm) consisting of LTO/CNT/PVDF-coated paper as anode, monolayer polypropylene (Celgard 2500) as separator, and LCO/CNT/PVDF-coated paper as cathode was used as

the control test. Cu and Al foils were used as additional current collectors and the cells were sealed in aluminized polyethylene (PE) bags (Sigma-Aldrich) as pouch cells. This planar full cell is shown schematically in Figure 5.9B. To test the effect of a single fold, a 2 cm × 4 cm cell was prepared in the same manner as the planar one and folded in half with the anode in the center of the cell (Figure 5.9C). To test the effect of two folds, a 4 cm × 4 cm cell was prepared and folded in half twice. Finally, a cell with three folds was prepared from an initial area of 4 cm × 8 cm. In all cases, a Cu tab was placed in between the folds to make contact to the LTO/CNT/PVDF-coated paper. The final geometric area of all of these cells was 2 cm × 2 cm.

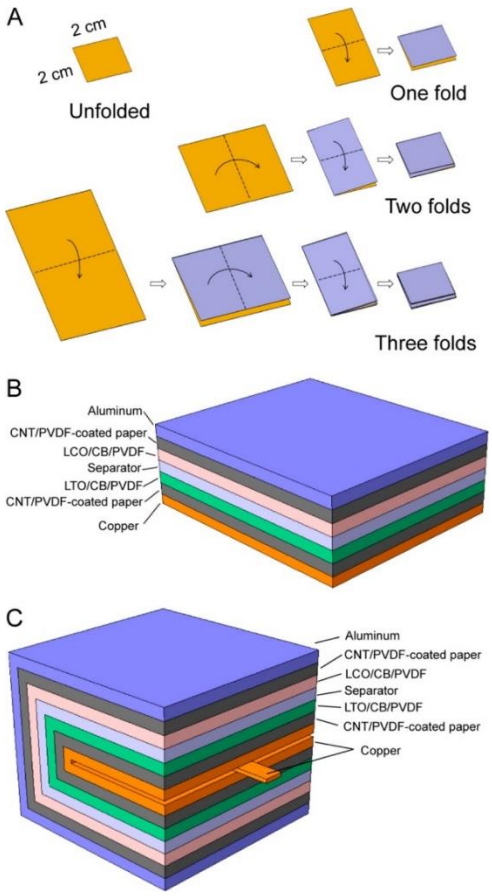

Figure 5.9 (A) Schematic of folding procedures for batteries with one fold, two folds, and three folds. (B) Schematic showing planar, unfolded full cell, and (C) full cell with one fold.

The voltage profiles for the folded cells looked very similar to the planar, unfolded cells and the cells displayed similar gravimetric capacities. Figure 5.10A compares the first charge and discharge curve for the unfolded cell and cell with three folds. As shown in Figure 5.10B, the areal capacities increased with increasing number of folds, as expected, since the amount of active material per square centimeter was increased. The

amount of active material in each cell was slightly different since manual doctor blading was used but ranged from 0.92 to 1.29 mg/cm^2 in the unfolded state (Table 5.4).

Table 5.4 Mass loading and cell dimensions for unfolded and folded batteries

	Unfolded	1 fold	2 fold	3 fold	Unfolded Miura-Ori Pattern	Folded Miura-Ori Pattern
Unfolded area (cm x cm)	2 x 2	2 x 4	4 x 4	4 x 8	6 x 7	6 x 7
Mass loading before folding (mg/cm^2)	0.9715	0.9284	1.2519	1.2887	1.0541	0.7365
Area after folding (cm x cm)	2 x 2	2 x 2	2 x 2	2 x 2	6 x 7	1.2 x 1.4

The batteries with one fold, two folds, and three folds had approximately 1.9×, 4.7×, and 10.6× the areal capacity compared to the planar one. The CE for the folded cells were higher than for the unfolded cell (Figure 5.10C). The reason for the higher CE in the folded cells is not understood but may be due to improved contact between the active materials layers and the CNTs after folding. These results show that the Li-ion batteries can still exhibit good electrochemical performance even after multiple folds.

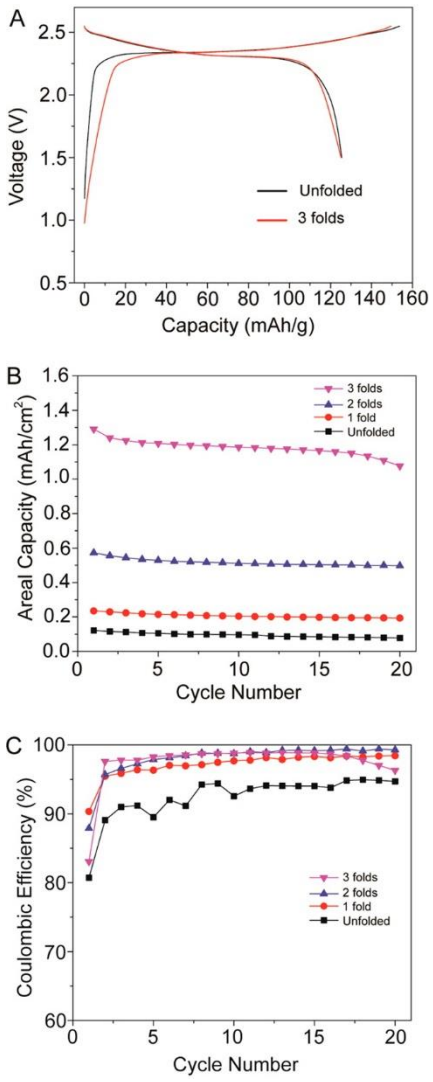

Figure 5.10 (A) Comparison of voltage profiles for unfolded full cell compared to cell with three folds. (B) Comparison of areal discharge capacities and (C) Coulombic efficiencies for folded cells compared to unfolded, planar cell.

SEM imaging was employed to observe the morphology of the folded electrodes after cycling. Figure 5.11 shows the images of the front side (containing the active material layer) and backside (containing CNTs only) of the cathode and anode in the region of a

crease resulting from a single fold. No discernible cracking, delamination, or other change in microstructure was observed compared to the planar electrodes (Figure 5.6).

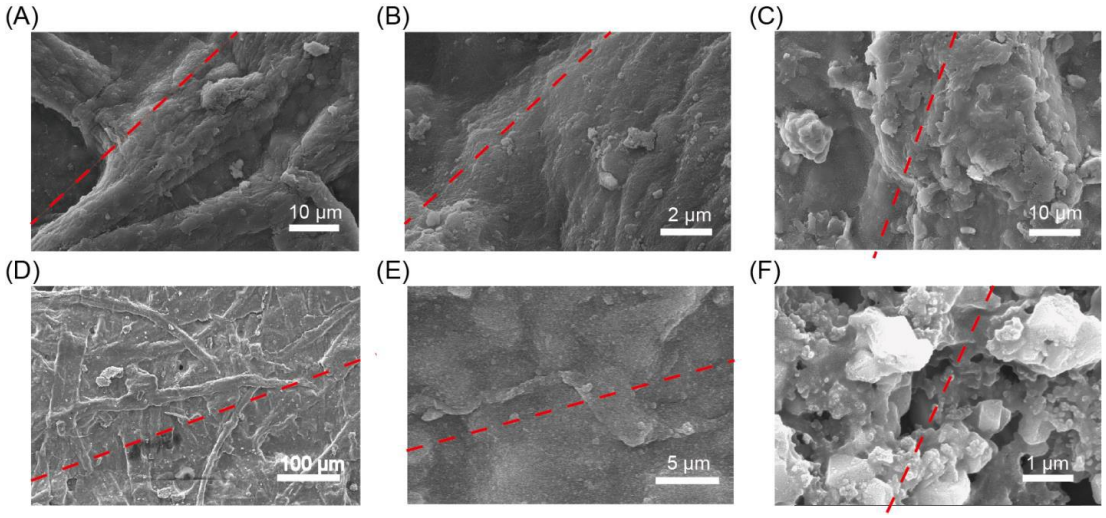

Figure 5.11 SEM images of electrodes after folding and unfolding, zooming in at a crease resulting from one fold (approximate location indicated with red dashed line). All images are from electrodes after cycling. (A) and (B) are from the backside of the cathode, showing the bare surface of the CNT/PVDF-coated paper; (C) front side of the cathode, showing the LCO layer surface; (D) and (E) are from the backside of the anode; (F) front side of the anode, showing the LTO layer surface.

When looking at the vertex corresponding to the intersection of two perpendicular folds, some delamination of the CNT-layer was observed, revealing the paper fibers underneath (Figure 5.12). However, far away from the intersection, no delamination was observed as shown in Figure 5.11. These results show that lower specific capacities

(compared to planar cells) in batteries with high degrees of folding may be due to poor adhesion of the CNT coating at the high stress regions found at vertices.

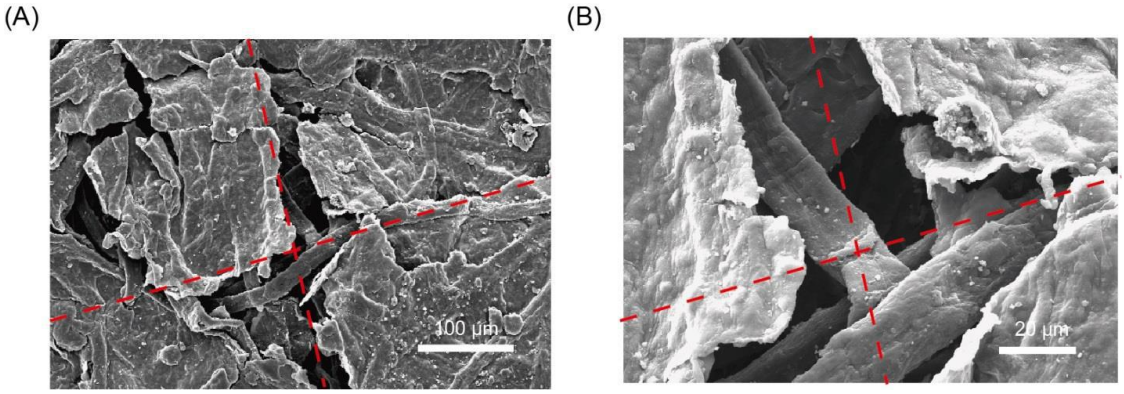

Figure 5.12 SEM images of electrodes after folding and unfolding, zooming in at a crease resulting from the intersection of two folds (approximate location indicated with red dashed lines). Both images are from the back of an electrode after cycling, showing the CNT layer. (A) Low magnification, (B) zoomed in version of same region.

The data in Figure 5.10A indicate that this delamination may not play a large role in the cells with three folds, because there were only two of these vertices and the specific capacity was almost identical to that in the unfolded cell.

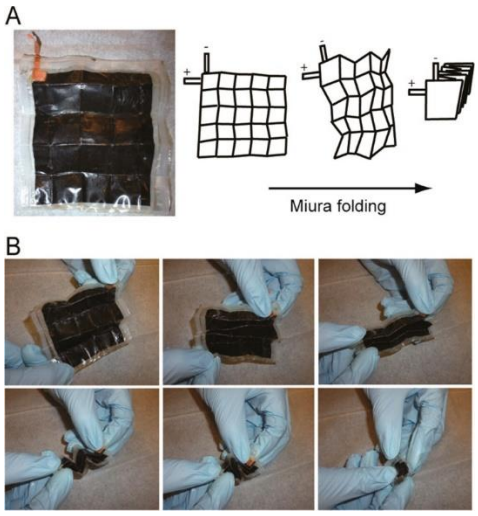

Figure 5.13 (A) Schematic of Miura folding procedures for 5 × 5 pattern and photographof 6 cm × 7 cm battery sealed in Parylene-C (unfolded state). (B) Photographs of Miura folding to compact the battery to its folded state.

To increase the areal capacities further, Miura folding[113] was used to more efficiently compact and fold the paper (Figure 5.13A). In these Miura batteries, additional Cu or Al current collectors were not used because they can not be folded that many times. Thus, the CNT/PVDF-coated papers served as the sole current collector. Double-sided tape was used to fix the Cu or Al metal tabs to the back of the CNT/PVDF-coated papers since no additional metal current collector was used. While the anode/separator/cathode layers can be compacted using Miura folding, the aluminized PE bags were too thick and did not crease well. Therefore, Parylene-C was used to prevent short-circuiting between adjacent layers after folding. Parylene-C is a monochlorosubstituted poly(para-xylylene) that has been used in flexible sensors[116] and electronic devices[117] and has good chemical resistance and permeability to gases and humidity.[118] Twenty grams of parylene dimer were used to deposit 40 μm thick Parylene-C thin films on a flat glass mold using a

Parylene coater (Specialty Coating Systems Labcoter 2). A release agent (2% Micro soap solution) was applied to the mold prior to the coating process. After the coating, the Parylene-C film was peeled off. The cells were sealed in between two Parylene-C films using an impulse sealer. The photographs in Figure 5.13 show cells sealed in Parylene-C. The original area of the unfolded cell was 6 cm × 7 cm and creases were applied to the entire stack to create a 5 × 5 Miura-ori pattern. After Miura folding, the stack consisted of 25 layers with a geometric area of 1.68 cm^2 (Figure 5.13B). Galvanostatic testing was performed using 25 mA/g rate. For long-term testing, the folded cells were sealed inside aluminized PE bags to prevent air leakage. Figure 5.14A shows the voltage profile for the Miura battery in its folded state. The discharge capacity was 103 mAh/g in the first cycle and decreased to 74 mAh/g in the 20th cycle. The voltage profiles for the first charge/discharge for Miura battery when folded (red curve), and unfolded (blue curve) are compared in Figure 5.14B. The battery in the folded state showed a slightly lower discharge capacity of 103 mAh/g compared to 113 mAh/g when unfolded. Compared to the results for the cell with three folds (Figure 5.10A), the gravimetric capacity was lower in the folded cell. The lower specific capacity in the folded cell may indicate that some of the active material was inaccessible to the electrolyte after folding. It can also be due to delamination at the intersections of perpendicular folds, since the 5 × 5 Miura pattern contains 16 of these vertices. The charging curve of the folded Miura cell was also shifted up to higher potentials and the discharge curve was shifted to lower potentials compared to the unfolded state. This suggests that there are some internal resistance losses for the cell in the folded state as a result of using the CNT/PVDF-coated papers as the sole current collectors. However, these potential differences were only 50 mV. The internal

resistance losses can also be responsible for why the gravimetric capacities are lower in the Miura folded batteries compared to the simple folded cells, which had Cu and Al foil backing layers underneath the CNT/PVDF-coated papers. However, the Miura folding still resulted in a significant increase in areal capacity compared to the planar cells. As shown in Figure 5.14C, the areal capacity was ~14× higher for the folded Miura cell at the 20th cycle, indicating that the Miura folding can be used to increase the energy density of the Li-ion battery.

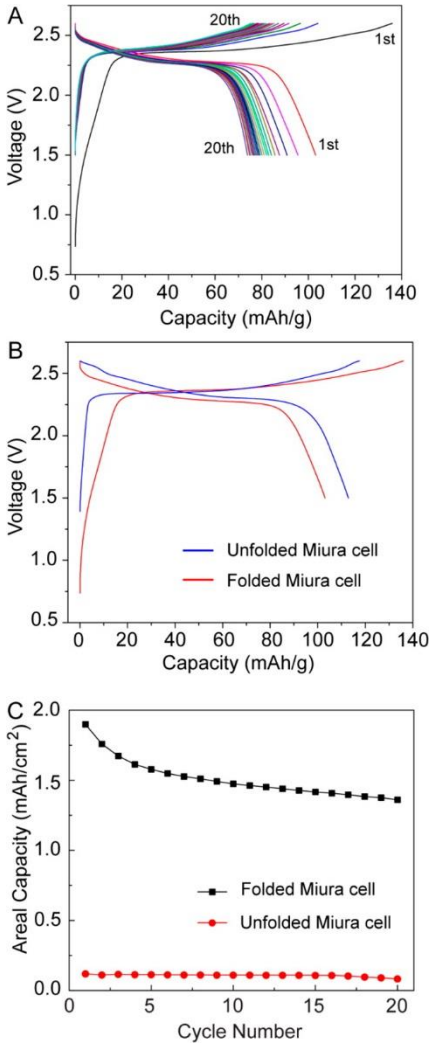

Figure 5.14 Comparison of folded versus unfolded Miura cell. (A) Charging and discharging curves for Miura cell in the folded state; (B) voltage profiles and (C) areal discharge capacities for folded versus unfolded cells.

5.5 Conclusions

We have shown that paper-folding concepts can be applied to Li-ion batteries in order to realize a device with higher areal energy densities. CNTs coated with ordinary laboratory Kimwipes and modified with PVDF binder were effective current collectors for the LTO anodes and LCO cathodes to allow for current flow throughout the folded batteries. Parylene-C was utilized as the Li-ion battery packaging to prevent short-circuits after Miura folding. Advances in geometric folding algorithms and computational tools[111, 119] to determine folding patterns for making complex 3D structures from planar 2D sheets may lead to numerous other configurations possible for 3D batteries. Folded cells showed higher areal capacities compared to the planar versions, with the a ~10X increase in the 3-folded cell A 5 x 5 cell folded using the Miura-ori pattern displayed a ~14X increase in areal energy density. Furthermore, with advances in robot manipulation including paper folding by robots,[120] the manufacturability of folded batteries at scale may be possible in the near future.

6 EVALUATION OF THE PHOTOELECTROCHEMICAL PROPERTIES OF Sn-DOPED $AgInS_2$

6.1 Introduction to Photocatalytic Water Splitting

Hydrogen as a clean energy source has received a lot of attention during the past few decades. The combustion product of hydrogen is water which can be decomposed into hydrogen and oxygen again without generation of any pollutant. The rapid development of fuel cells have made hydrogen-fuel-cell cars possible. However, most of the hydrogen production is from degradation of fossil fuels, which contributes to carbon emissions, or electrolysis of water, which is expensive. This further impedes the wide application of hydrogen fuel cells.

Since Fujishima and Honda reported that TiO_2 can be used to split H_2O into H_2 and O_2 under UV irradiation, photocatalyic water splitting using semiconducting absorber materials has been investigated for solar energy-to-fuel applications.[121] Besides TiO_2, a wide range of semiconductors were discovered as highly efficient photocatalysts, such as WO_3,[122] ZnO,[123] Fe_2O_3,[124] $NaTaO_3$,[125] and ZnO-GaN solid solution[126].

Understanding how semiconductors can split water beings with energy band theory. According to the Pauli exclusion theory, each electron in an isolated atom has a unique quantum state. Electron orbitals in the atom are independent and indiscrete with each other and each orbital has two quantum states: spin-up and spin-down. That means one orbital can contain two electrons. When two atoms form a bond, the two discrete valence electron orbitals will combine and form two orbitals: a bonding orbital and anti-bonding

orbital. Electrons will stay in the bonding orbitals due to their lower energy. When multiple atoms join the systems (the number of electron is N), there will be N/2 bonding orbitals which are full of electrons and N/2 antibonding orbitals which are empty. The process is illustrated in Figure 6.1. The bonding band that is filled with electrons is called the valence band; the empty anti-bonding band is called the conduction band. There are not any electron orbitals existing between the conduction band and valence band. The region without electron orbitals is called the forbidden band. The width of the forbidden band is determined by the difference between the conduction band minimum (CBM) and valence band maximum (VBM) and is called bandgap.

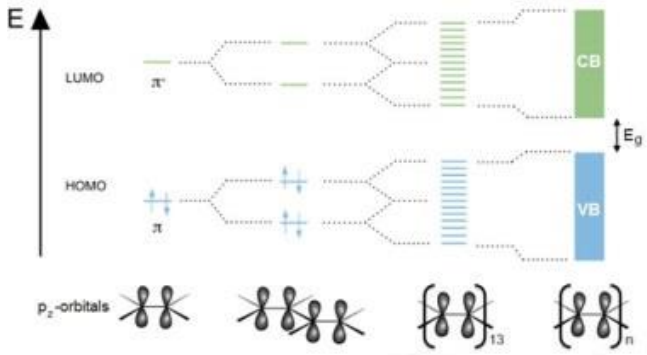

Figure 6.1 Scheme of the formation of bands. Source: M. Rehahn, Elektrisch leitfähige Kunststoffe, Chiu. Z, 37(1), 20, 2003

The electrons in the valence band can be excited to the empty conduction band once they accept enough energy from photons or phonons that have energy higher than the bandgap, then the excited electrons can move freely in the empty conduction band. What is left in the valence band is a hole that is treated as a positively charged electron which can also move freely in the valence band. Therefore, there are two kinds of carriers in the semiconductor: electrons and holes. The width of the bandgap directly determines the

number of electrons that can be excited, and thus the conductivity of semiconductor. The excited electrons in the conduction band can return to the valence bands, coming along with the elimination of an electron-hole pair and release of energy in the form of photons and phonons, a process that is called recombination. The excited electrons and holes have strong reducing power and oxidizing power, which are determined by the position of CBM and VBM respectively. These charge carriers can participate in electrochemical reactions, such as water splitting to form hydrogen and oxygen. To realize full water splitting, the generated photo excited electron/hole pairs must be swept to the solid/liquid interface without recombining. If the CBM and VBM of a semiconductor can straddle the redox position of H_2/H^+ and O_2/OH^- as shown in Figure 6.2, excited carriers will react with these species adsorbed on the surface of photocatalyst.[127, 128]

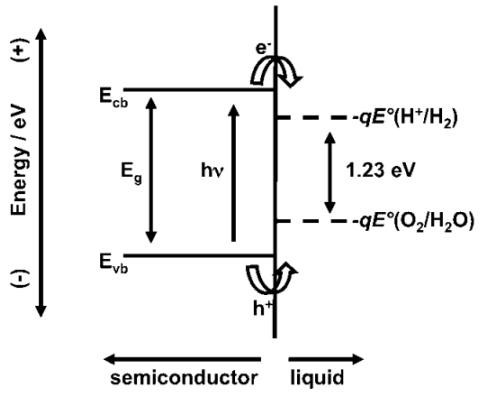

Figure 6.2 The CBM and VBM criteria for semiconductors to split water.[127]

Figure 6.3 illustrates some common semiconductor photocatalysts and their band edges. It is worth noticing that only a few semiconductors can satisfy the requirement for overall water splitting. Besides, there are more properties that affect the efficiency of water

splitting, such as bandgap energy, carrier lifetime, diffusion length and light absorbance. Therefore it is very hard to find a suitable photocatalyst to realize full water splitting.

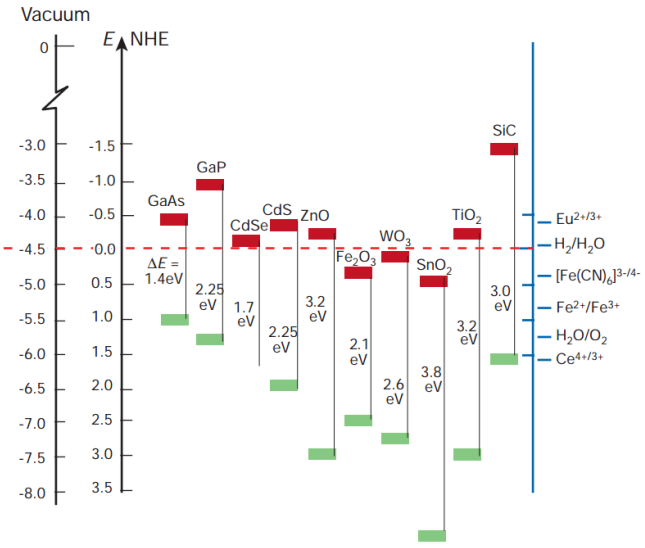

Figure 6.3 the CBM and VBM of common semiconductor photocatalysts.[129]

6.1.1 Introduction to Photocatalyst Slurry System

Semiconductor photocatalysts can be used in different configurations. For powder-slurry systems, photocatalysts are directly immersed into water as shown in Figure 6.4. [130] The performance of photocatalysts can be evaluated by measuring the production of hydrogen and oxygen over the time using a gas chromatography or gas analyzer. Lifetime is another important criteria for the evaluation of photocatalysts. The simultaneous generation of large quantities of hydrogen and oxygen would cause safety issues and require extra costs to separate hydrogen and oxygen.

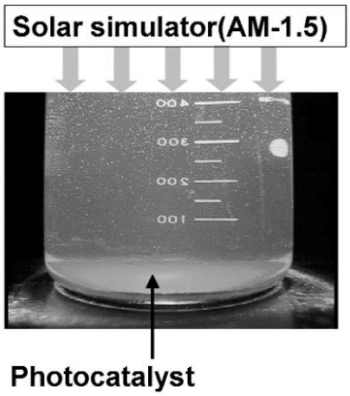

Figure 6.4 Photocatalyst undergoes water splitting in simulated solar cells.[130]

Another difficulty of full water splitting is that most photocatalysts can only realize one of the half reactions. The problem originates from the band positions and solid-liquid interface electrical field. When semiconductors were immersed into the aqueous solution, the position of redox in the aqueous solutions must align with the Fermi level of the semiconductors due to the requirement of equal chemical potential. Then a solid-liquid interface electrical field must be built to compensate the difference of chemical potential. The existence of solid-liquid electrical field can only swept the photo-generated carriers into the solid-liquid interface, which means only one reaction can happen at the interface. However, photo water splitting must have both half reactions at the interface in equal rates, both photo-generated carriers must be swept to the interface in order to improve the efficiency. In this case, a sacrificial reagent can be used to accelerate the slower half reaction as shown in Figure 6.5. [131] The usage of sacrificial reagents can increase the over potential of slower half reaction, and thus accelerate the slower half reaction to improve the overall photocatalytic reaction.

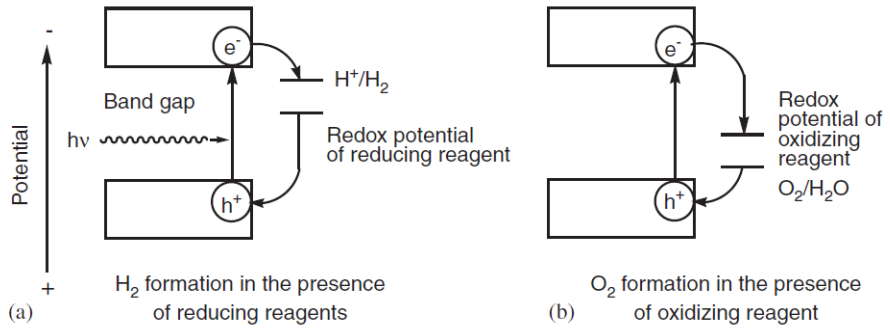

Figure 6.5 Scheme of photocatalytic H_2 or O_2 evolution in the presence of sacrificial reagents.[131]

Another method that can improve the efficiency of photocatalysts involves the utilization of co-catalysts, which can be noble metals (Pt/Ir) or transition metal oxides (CoO_x, NiO_x) as shown in Figure 6.6. The presence of co-catalysts can accelerate the reaction rate between the carriers and adsorbed species by providing more reaction sites and reducing activation energies for the reactions.

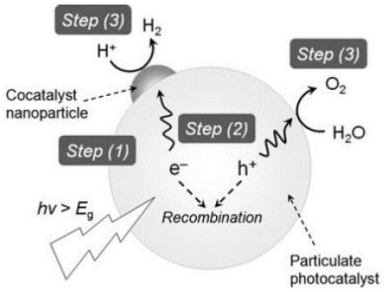

Figure 6.6 Processes involved in full water splitting under the assistance of co-catalyst.[128]

6.1.2 Introduction to Photoelectrochemical Cells

Photoelectrochemical cells can be utilized to address problems of slurry systems. The architecture of a photo-electrochemical cell is shown in Figure 6.7. It looks very similar with heterogeneous photocatalysts, but instead of direct contact between the co-catalyst

and photocatalyst, they are separated and connected through an outside electric-chemical workstation. Photocatalysts can be analyzed by using multiple techniques using a potentiostat, such as Mott-Schottky, linear sweep voltammetry, and open circuit voltage measurements, which can provide information about carrier concentrations, flat-band positions, photo voltage, and diffusion coefficients.

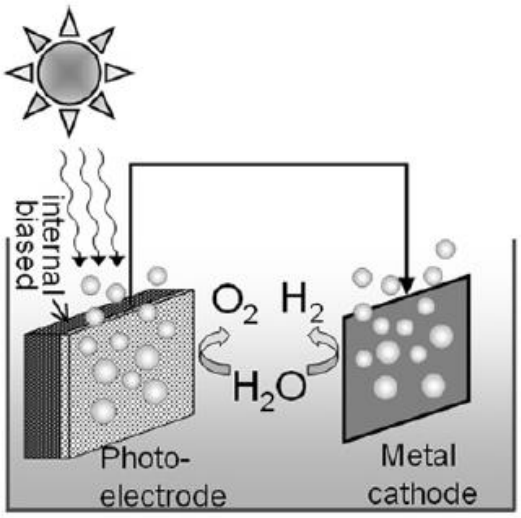

Figure 6.7 photoelectrochemical cells generate hydrogen/oxygen using sunlight.[132]

Different from solar cells that use p-n junctions to separate carriers, photo-electrochemical cells take advantage of the solid-liquid electrolyte junction to generate a photo-voltage and separate photo-generated carriers. At each electrode, only one reaction, either oxidation of hydroxide or reduction of protons, will occur. This is convenient for the collection of H_2 and O_2 in separate locations. If the electrode cannot provide enough photovoltage, the outside potentiostat can provide extra applied voltage to adjust the photoelectrode to reach an ideal water splitting efficiency.

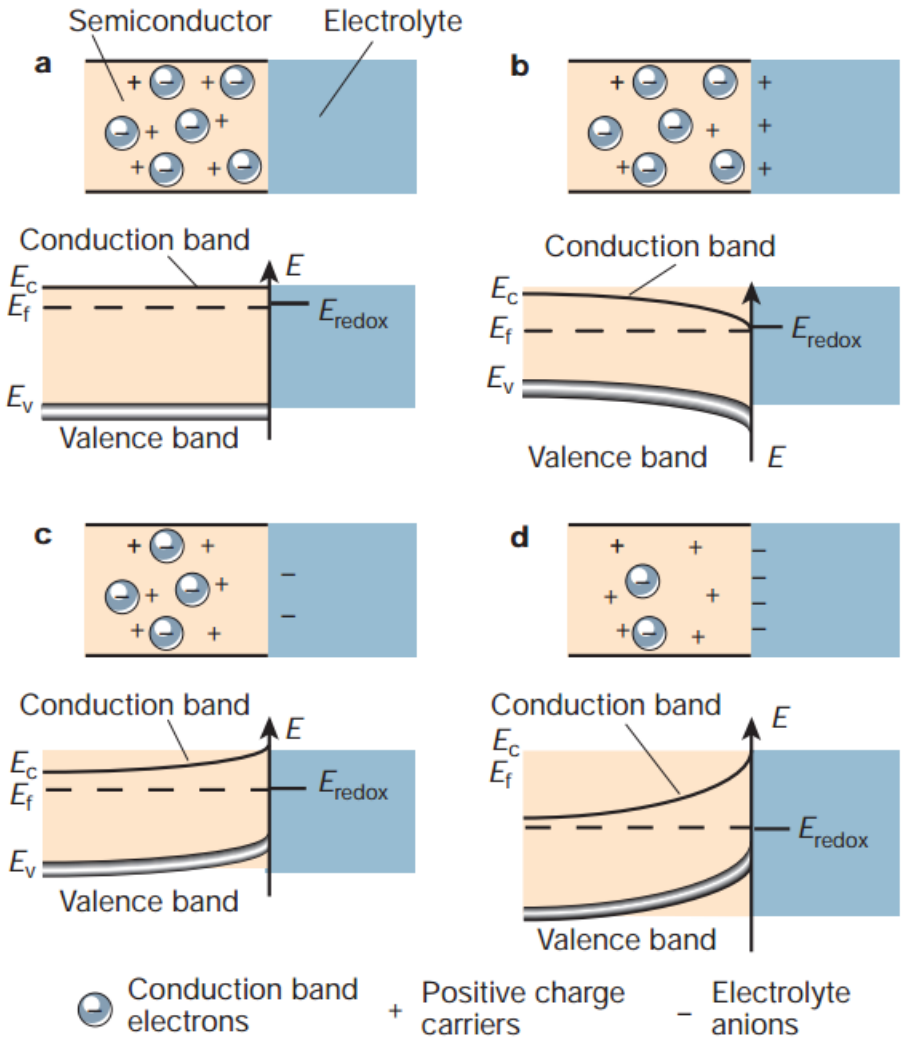

Figure 6.8 Semiconductor that was immersed into electrolyte. (A) Flatband position, (B) accumulation mode, (C) depletion mode and (D) Reverse mode.[129]

Figure 6.8 shows the solid-liquid interface of n-type semiconductors. The chemical potential should be equal everywhere in the absence of an applied external voltage; therefore the inner electrical field is determined by the Fermi level of the semiconductor and redox potential in the electrolyte. The depletion mode is the working mode for a

photoanode, in which the photogenerated holes (minority carriers) can be swept to the interface and oxidize adsorbed OH^-.

$$4OH^- + h^+ \rightarrow 2H_2O + O_2$$

For p-type semiconductors it is electrons that are swept to the interface for the reduction of protons to form hydrogen.

$$2H^+ + e^- \rightarrow H_2$$

6.1.3 Introduction to the Testing Systems of Photoelectrode

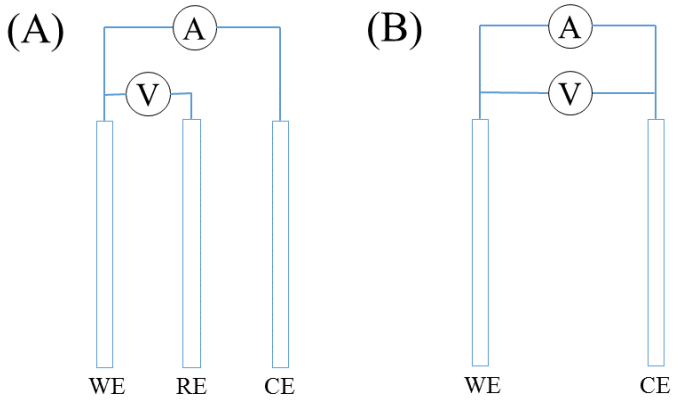

Figure 6.9 (A) Three-electrode and (B) Two-electrode systems. WE, RE and CE are working electrode, reference electrode and counter electrode respectively.

The difference between two-electrode and three-electrode systems is shown in Figure 6.9. In three-electrode systems, there exists a reference electrode which can provide a stable potential as a standard. Ag/AgCl (3M KCl) electrode, which has a potential of 0.21 V vs NHE, was used in all of our photoelectrochemical measurements. The potential of the working electrode can be accurately changed and measured by applying a bias voltage between the working electrode and counter electrode. For two-electrode systems,

the working electrode and reference are short circuited, and the voltage is applied only between the working electrode and counter electrode. Therefore it is hard to know the precise chemical potential of the working electrode.

The solar to hydrogen conversion efficiency (STH) is the most important parameter for evaluating a photoelectrode. The STH can be calculated by this equation[127]:

$$\eta_{STH}(\%) = \frac{J_{sc}(mA/cm^2) * (1.23 - V_{app})}{P_{total}}$$

J_{sc} is the current flowed from cathode to anode which was recorded by the potentiostat. V_{app} is the applied voltage between the working electrode and reference electrode. As mentioned earlier, due to the disadvantageous position of the semiconductor's VBM and CBM, a slight applied voltage may be needed to adjust the STH to the maximum efficiency. For a two-electrode system, the V_{app} is the voltage applied between the WE and CE. The current between the photocathode and photoanode must match to reach a maximum efficiency. The blue box in Figure 6.10 represents the converted chemical energy.

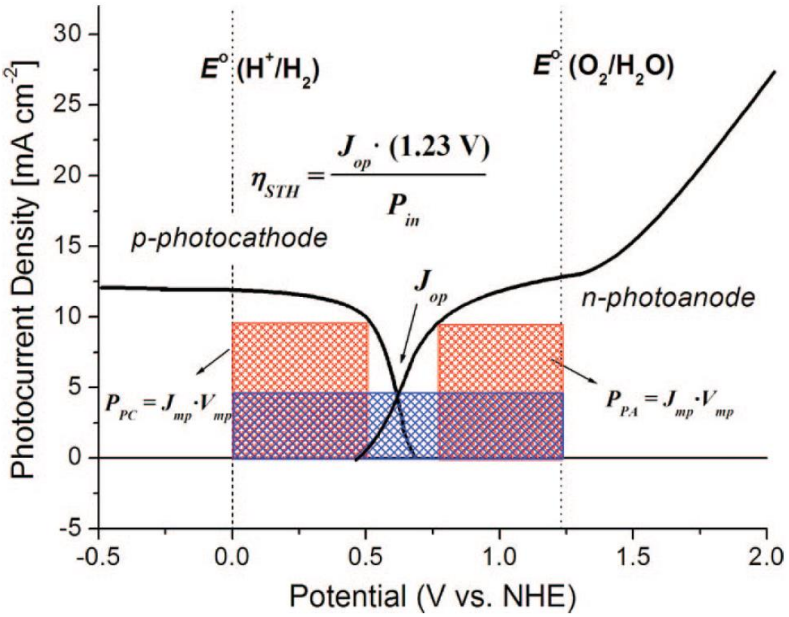

Figure 6.10 Linear sweep voltammetry of photoanode and photocathode and how to measure STH.[127]

To explore the maximum efficiency, linear sweep voltammetry (LSV) is widely used to measure the current passing through the electrode at different voltage. The red box in Figure 6.10 represents the actual converted energy, J*(1.23-V). We need to find the maximum of energy output (E_{max}) by using the I-V curve. The fill factor (ff) is another important parameter:

$$ff = \frac{J_{sc}(mA/cm^2) * (1.23 - V_{app})}{V_{oc} * I_{sc}}$$

Similar with solar cells, it is a key parameter for evaluating the performance of a photoelectrochemical cell.

6.1.4 Ultraviolet-Visible Microscopy

Ultraviolet-visible light (UV-Vis) spectroscopy measurements give us information about optical properties such as light absorption and bandgap as a function of wavelength through electronic transitions occurring in the material. We usually measure the transmittance and reflectance of light through a material. The transmittance of light through a sample follows the Beer-Lambert law:

$$\frac{I}{I_0} = e^{-\sigma(N_1 - N_2)l}$$

Where I is the transmitted light and I_0 is the initial incident intensity, l is the path length of light through the sample, and σ is the absorption. N_1 and N_2 are the number of initial states and excited final states, respectively. The more common form of the equation is:

$$A = \varepsilon cL = \log_{10}(\frac{I_0}{I})$$

Where A is the absorbance, ε is the molar absorptivity coefficient of the material, c is the concentration of the absorbing species, and L is the path length of light through the sample. Optical transmission and diffuse reflectance in this work were obtained by using a UV/Vis spectrometer (Perkin–Elmer Lambda 18) equipped with an integrating sphere over the wavelength range of 300–850 nm. As mentioned above, semiconductors can only adsorb photons of which energy is higher than the bandgap to excite the electrons in the valence band. Therefore, it is very easy to determine the bandgap and if the semiconductor is a direct or indirect semiconductor using UV-Vis measurements. The bandgap can be determined from a plot of photon energy vs αhυ plotted using the

following equation:

$$\alpha h\upsilon = (h\upsilon - E_g)^{1/n}$$

N can be 2 or 1/2, depending on indirect (allowed) electron transition or direct (allowed) transitions, respectively.

6.1.5 Mott-Schottky Measurement

In photoelectrochemical cells, the flatband potential of the electrode, also known as the Fermi level of the semiconductor, is very important and Mott-Schottky is the one of the most accurate technique and can also give us information about the carrier concentration in the semiconductor.

Under different applied voltages, a semiconductor has different modes such as accumulation, flatband, depletion and reverse mode depending on the degree of band bending. There will be different charges in the space charge region under different applied voltage. This means there will be capacitance which is related to applied voltage following the below equation:

$$\frac{1}{C_{sc}^2} = \frac{1}{\varepsilon_r \varepsilon_0 A^2 e N_D}(V - V_{fb} - \frac{kT}{e})$$

Where C_{sc} is the space-charge capacitance of the semiconductor (F), ε_r is the relative permittivity of the semiconductor, ε_o is vacuum permittivity, A is the electrode area, e is the charge of an electron, N_D is the free carrier density, k is the Boltzmann constant, T is the temperature, V is the applied potential, and V_{fb} is the flatband potential. The potentiostat will apply an AC signal at a certain voltage, thus the capacitance at that

voltage can be measured. By linear plotting the Mott-Schottky curve of C^{-2} versus voltage, the carrier concentration can be calculated from the slope and the interception of linear plot of C^{-2} and voltage is the flatband position.

6.2 Introduction to Chalcopyrite Structure

Currently, the most studied semiconducting materials for photoelectrochemical cells (PEC) have been oxides such as TiO_2, WO_3, and Fe_2O_3. However, these oxides have bandgaps >2 eV, which limits their solar energy-to-H_2 efficiency. There has been much work on the incorporation of dopants to increase visible-light absorption in these oxide materials without the introduction of sites where the photogenerated carriers can recombine.[133-136] These issues related to light absorption and the transport of charge carriers are also relevant to researchers in the photovoltaic (PV) community. Among the most promising and successful thin-film PV materials are based on the Cu-chalcopyrite family, of which $Cu(In,Ga)Se_2$ solar cells demonstrate approximately 20 % solar energy-to-electricity efficiency.[137, 138] The high performance of chalcopyrite absorbers is attributed to several unique characteristics of the materials, which include a high absorption coefficient of $10^5\ cm^{-1}$, a direct bandgap that is tunable based on its composition, high minority carrier diffusion distances, and a high tolerance for grain boundaries. However, chalcopyrites have very complex defect chemistries. Even ternary $CuInS_2$ (CIS) has 12 possible intrinsic defects (three vacancies, three interstitials, and six antisite defects), many of which have a very low defect-formation energy of approximately 1 eV.[139] As a result, there have been many studies that try to understand

the effect of intrinsic defects, as well as extrinsic dopants, on the transport and photovoltaic properties of chalcopyrites.

Chalcopyrites have also been investigated in photoelectrochemical applications because of their aforementioned attractive material properties, particularly the ease of band gap tuning through the formation of solid solutions. For example, solid solutions of $CuInS_2$, $AgInS_2$, and/or ZnS,[140-142] as well as $AgGa_{1-x}In_xS_2$alloys,[143] have been studied as slurry photocatalysts. Photocathodes of $CuInS_2$,[144] $CuInSe_2$,[144, 145] $Cu(In,Ga)Se_2$,[145, 146] Cu_2ZnSnS_4,[147, 148] and $CuGaSe_2$[149] have also been studied, but their solar energy-to-H_2 efficiencies are limited by the small bandgaps of Cu-chalcopyrites and band-edge positions that require large external bias to achieve overall H_2O splitting.[149] Owing to the kinetic overpotentials for H_2O splitting, a bandgap of 1.8 eV is suitable[150] to obtain the maximum efficiency (solar energy-to-H_2) in a PEC (compared to an ideal bandgap of 1.4 eV for PVs). To this end, $AgInS_2$ (AIS) is attractive as a photoelectrode because of its bandgap of 1.8 eV. In contrast to CIS, which is commonly p-type because of intrinsic defects (namely, Cu vacancies),[151] AIS is almost always n-type, which is likely a result of donor levels from S vacancies.[151-153] Compared to n-type oxides, AIS has a more suitable bandgap and band-edge position for both H_2 and O_2 production. The implication for this is that a p/n-PEC that uses an n-type chalcopyrite can result in a higher maximum operating current density (which can be found by overlapping the individually tested current–voltage characteristics for the photocathode and photoanode and determining the intersection of the curves) compared to an n-type oxide photoanode. [154] However, the drawback is that sulfides are generally not stable to photocorrosion if used as photoanodes,[155, 156] and thus the anodic reaction is typically the oxidation of sulfide- and

sulfite-based sacrificial reagents rather than that of H_2O. Nevertheless, recent reports have shown that atomic-layer-deposition (ALD) coatings of stable oxide materials such as TiO_2 can be used to impart remarkable stability to n-type Si,[157, 158] another photoanode suffering from photocorrosion, which suggests that coatings and other protection strategies may allow materials such as n-type AIS (n-AIS) to be relevant as photoanodes for H_2O oxidation. Thus, a better understanding of the photoelectrochemical properties of AIS and the effects of doping is needed.

This is particularly true considering that previous studies have shown that the properties of AIS are highly dependent on the method of synthesis. For example, AIS made by electrodeposition gave films with carrier concentrations of 10^{19} cm^{-3},[159] whereas AIS made by sulfurization of Ag-In metal gave films with a resistivity of 10^4 Ω cm and carrier concentrations of 10^{12} cm^{-3},[160] and AIS synthesized by hot-wall epitaxy onto GaAs displayed carrier concentrations of 10^{17} cm^{-3}.[161] Other films synthesized by using spray pyrolysis yielded AIS with resistivities between 10^3–10^5 Ω cm.[162] Additionally, the reason for the n-type behavior of AIS, and the compositional and structural requirements to turn it into p-type, are not well understood. For example, p-AIS was synthesized by using co-evaporation with Ag/In ratios from 0.77 to 1.13,[163] which suggests that AIS can be p-type in both Ag-rich and Ag-poor cases. This is different from CIS for which Cu vacancies promote p-type behavior. The role of extrinsic dopants in AIS is similarly not well understood. For instance, Sn is a dopant in n-type CIS;[164, 165] however, p-type AIS was also formed through doping with Sn.[166] In most of the previous work related to AIS characterization, the properties were determined by using solid-state methods such as hot-probe, thermoelectric, or Hall measurements; the relevant photoelectrochemical

measurements have not been performed for any of the p-AIS materials and have only recently been pursued for n-AIS and Ga-doped n-AIS.[160, 167]

Here, we report a systematic study on the effect of annealing conditions and Sn doping on the optical, electrical, and photoelectrochemical properties of AIS prepared by spray pyrolysis with the hope of shedding more light on the characteristics needed for high performance photoelectrodes. Compared to other methods to synthesize $AgInS_2$, such as hot-wall epitaxy, chemical-bath deposition, electrodeposition, co-evaporation, and sulfurization of metal films, it is easy to obtain large-scale, high-quality films by using spray pyrolysis. The effect of annealing the deposited films under a N_2 or S atmosphere was investigated to control the crystallinity and understand the role of S vacancies on the AIS films. Sn was used as an extrinsic dopant because of the previously reported work on Sn-doped, p-type AIS. Density functional theory (DFT) was also used to analyze the effect of Sn-doping in AIS.

6.3 Experimental and Computational Method

Spray pyrolysis was used to prepare undoped and Sn-doped $AgInS_2$ thin films on FTO glass substrates as described in the literature.[166] A solution of $SC(NH_2)_2$ (0.15 M, Sigma–Aldrich), CH_3COOAg (0.04 M, Reagent Plus, 99 %, Sigma–Aldrich), and $InCl_3$ (0.1 M, Sigma–Aldrich) was prepared in deionized water. CH_3COOAg and $SC(NH_2)_2$ were mixed first to form a dark brown solution to avoid precipitation. According to previous studies, Ag is more volatile than the other reagents, and the AIS chalcopyrite structure is favored when the sample is Ag rich.[166] Thus the Ag/In and S/In ratios used were 1.5 and 5, respectively. Excess S was needed owing to the volatility of

$SC(NH_2)_2$. $SnCl_4$ (Sigma–Aldrich) was added into the solution according to the ratio x=[Sn]/([Ag]+[In]), which was varied from 0 to 0.08. After 10 min of stirring, absolute ethanol was added to the solution to promote solvent evaporation during the deposition.

The substrates were cleaned by using ultrasonication in acetone, ethanol, and deionized water for 30 min each. After cleaning, the FTO glass was fixed to a hot plate with a temperature of 300 °C, as determined by using an IR camera. N_2 was used as the carrier gas at a pressure of 6×10^5 Pa. The spacing between the spray gun and the substrate was 25 cm. After deposition of the film, the sample was washed with ethanol. For annealing experiments, N_2 annealing was performed in a tube furnace at 375 °C for 1 h, whereas S annealing was performed by adding S (250 mg, Sigma–Aldrich) and the samples to a steel autoclave sealed with a Cu O-ring gasket followed by heating in a box furnace at 400 °C for 2 h. After S annealing, the sample was heated at 120 °C for 10 min under N_2 to remove any excess S deposited on the surface.

XRD characterization of the films was performed under monochromatic CuK_α radiation (λ=1.5405 Å, Panalytical X′pert Pro). Field emission scanning electron microscopy (FSEM, FEI XL30) and EDS were performed to characterize the morphology and composition of the deposited films. To accurately determine the Sn concentration, EDS was performed on Sn-doped AIS films that were deposited onto glass substrates, not FTO. The surface thickness was determined by using a profilometer (Dektak II).

All photoelectrochemical tests were performed by using a potentiostat (Biologic VMP3) with the sample as the working electrode, Pt wire as the counter electrode, and a Ag/AgCl reference electrode. The electrolyte was prepared with deionized water and

contained Na_2S (0.35 M) and Na_2SO_3 (0.25 M, pH 13) as sacrificial agents. A 450 W Xe lamp (Newport, model 66923) was used to provide an illumination of 100 mW cm^{-2} intensity. The intensity of the illumination was measured by using a photometer (Thorlabs, Model S303). LSV was performed in the dark and under illumination from −1.0 to 0.5 V vs. Ag/AgCl. The photocurrents were evaluated by subtracting the dark current from the light current at 0.5 V vs. Ag/AgCl. To determine the flat-band voltage, illuminated open circuit measurements and M–S analysis were performed in an electrolyte that contained sacrificial reagents to compare to the photocurrent onset values obtained from LSV. M–S analysis was performed in the dark with a frequency of 10 Hz, AC amplitude of 25 mV, and voltage range of −0.9 to −0.6 V vs. Ag/AgCl. M–S analysis was also used to determine the free carrier concentration. Chronoamperometry was used perform the stability test at 0 V vs. Ag/AgCl in a Na_2SO_4 (0.5 M) electrolyte.

DFT calculations were performed to study the Sn-doping effects in AIS by employing the VASP code. The PBE functional and projector-augmented wave (PAW) potentials were used along with plane wave basis sets. The energy cutoff for the plane wave basis set was 300 eV. The total energy was converged to within 0.01 meV. The reciprocal space of the crystal was sampled at 6×6×6 by using Monkhorst–Pack meshes. The Ag 4d and 4s; In 4d, 5s, and 5p; S 3s, and 3p; and Sn 4d, 5s, and 5p electrons were treated as valence electrons in the calculations. Based on these parameters, the tetragonal $AgInS_2$ (space group *I42d*) bulk crystal lattice constants were a=5.937 Å and c=11.456 Å, which are very close to the experimental values.

To dope $AgInS_2$ with Sn, there are generally four possible doping scenarios: the Sn atom can take a 1) Ag site, 2) In site, 3) S site, or 4) interstitial site. To change the doping rate of Sn, four different $AgInS_2$ simulation cells were studied: a) using the unit cell for a doping rate of x=0.125, b) using a 2×1×1 supercell for x=0.0625, c) using a 2×2×1 supercell for x=0.031, and d) using a 2×3×1 supercell for x=0.02. To identify which site the dopant Sn prefers, the dopant formation energy is defined as follows [Eqs. (5.1)–(5.4)]:

For Sn in an Ag site:

$$E_{form} = E(\mathrm{SnAg_{4m-1}In_{4m}S_{8m}}) - \left[E(\mathrm{Ag_{4m}In_{4m}S_{8m}}) + E(\mathrm{Sn}) - E(\mathrm{Ag})\right] \quad (5.1)$$

For Sn in an In site:

$$E_{form} = E(\mathrm{SnAg_{4m}In_{4m-1}S_{8m}}) - \left[E(\mathrm{Ag_{4m}In_{4m}S_{8m}}) + E(\mathrm{Sn}) - E(\mathrm{In})\right] \quad (5.2)$$

For Sn in a S site:

$$E_{form} = E(\mathrm{SnAg_{4m}In_{4m}S_{8m-1}}) - \left[E(\mathrm{Ag_{4m}In_{4m}S_{8m}}) + E(\mathrm{Sn}) - E(\mathrm{S})\right] \quad (5.3)$$

For Sn in an interstitial site:

$$E_{form} = E(\mathrm{SnAg_{4m}In_{4m}S_{8m}}) - \left[E(\mathrm{Ag_{4m}In_{4m}S_{8m}}) + E(\mathrm{Sn})\right] \quad (5.4)$$

in which the m values 1, 2, 4, and 6 correspond to the unit cell, the 2×1×1 supercell, the 2×2×1 supercell, and the 2×3×1 supercell, respectively.

6.4 Results and Discussion

6.4.1 XRD Patterns of $AgInS_2$ Films

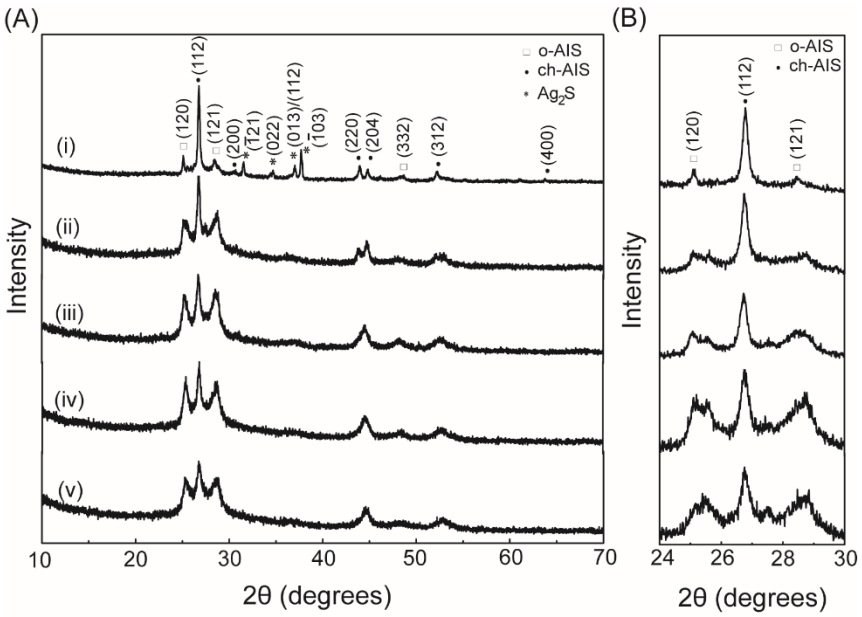

Figure 6.11 XRD pattern for AIS films deposited using spray pyrolysis onto glass substrates for x = [Sn]/([Ag]+[In]) where x is (i) 0, (ii) 0.02, (iii) 0.04, (iv) 0.06, and (v) 0.08, (A) as deposited, and (B) after annealing in nitrogen.

Compared to other I–III–VI compounds, AIS can adopt an orthorhombic phase in addition to a tetragonal chalcopyrite phase, of which the chalcopyrite phase is stable to >620 °C and characterized by a bandgap of 1.86 eV compared to 1.96 eV for the orthorhombic phase.[168] Figure 6.11A shows the XRD patterns of films of undoped AIS as well as AIS with different amounts of Sn doping after spray pyrolysis onto glass substrates prior to annealing under N_2. The main peaks belong to the (112), (200), (220), and (312) planes of the chalcopyrite phase of $AgInS_2$ (ch-AIS). The (112) peak shows the strongest intensity, which indicates that spray pyrolysis can yield ch-AIS with good crystallinity. Smaller peaks that belong to the orthorhombic phase (o-AIS) were also

present, and Ag_2S was observed in the undoped sample. These side products are likely to be present because the precursor solution was Ag-rich to compensate for the volatility of Ag.[153] Ag-rich precursor solutions also resulted in films with a predominant chalcopyrite structure in previous studies. Samples synthesized at temperatures below 300 °C did not crystallize well or show good adhesion to the substrate after PEC testing. The amount of Sn doping was controlled through the ratio x=[Sn]/([Ag]+[In]). Changing x from 0 to 0.08 did not change the presence of the ch-AIS peaks, although the increasing Sn concentration caused the Ag_2S peak to disappear and the o-AIS peaks to increase in intensity. This suggests that the presence of Sn can affect the structure of as-deposited AIS to favor the orthorhombic phase. After annealing the films under N_2, the ch-AIS (112) peak increased in intensity relative to the o-AIS peaks (Figure 6.11B). Deposition of the AIS films onto the fluorine-doped tin oxide (FTO) substrate showed similar XRD patterns, although the large reflections from FTO obscured the smaller peaks of o-AIS and Ag_2S (Figure 6.12). However, the peak intensities from o-AIS were significantly weaker for AIS films deposited on FTO compared to those on glass, which indicates a preference for ch-AIS formation over that of o-AIS on FTO.

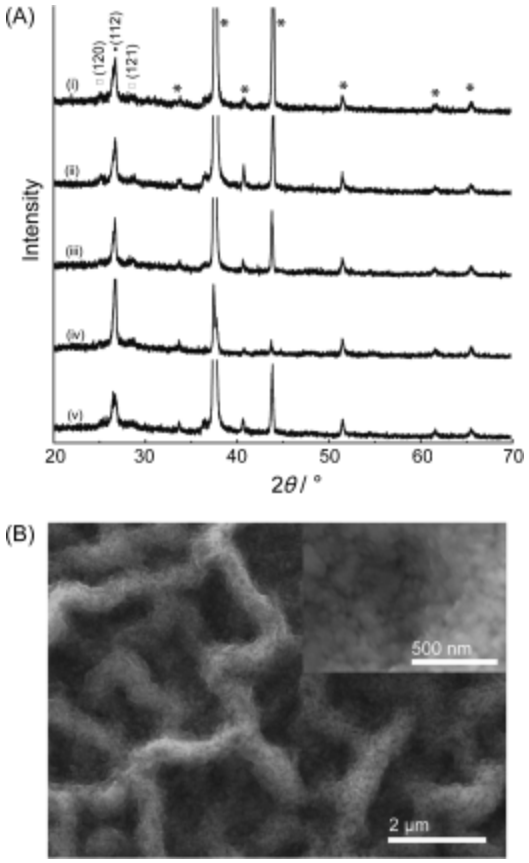

Figure 6.12 (A) XRD pattern for AIS films deposited by using spray pyrolysis onto FTO substrates (□ o-AIS, • ch-AIS, ✶ FTO) for x=[Sn]/([Ag]+[In]) in which x is (i) 0, (ii) 0.02, (iii) 0.04, (iv) 0.06, and (v) 0.08. (B) SEM image of an AIS film, inset shows magnification.

In previous studies on Ga-doped AIS, the (112) peak was observed to shift towards lower diffraction angles with increasing Ga content, which indicates the substitution of Ga at In sites, which is expected from the ionic radii of 0.8 Å for In^{3+} and 0.62 Å for Ga^{3+}.[143, 167] In contrast, the XRD pattern of Sn-doped AIS did not appear to have any peak shifts relative to the undoped AIS, which suggests that the Sn dopants did not occupy Ag or In sites.

6.4.2 Morphology and Composition

The AIS films showed a wavy morphology textured with nanoparticles as small as 30–60 nm. The microstructure was not affected by Sn doping. Figure 6.12B shows an SEM image of Sn-doped AIS with x=0.02 on FTO. Other reports of the use of spray pyrolysis to deposit AIS[166] did not achieve the same morphology, but had films that displayed more bulk characteristics. It is possible that this morphology is a result of the formation of small droplets of 110–120 μm in diameter from the atomization of the precursor solution during spraying. Spray deposition onto Mo-foil substrates led to films with similar morphologies (Figure 6.13).

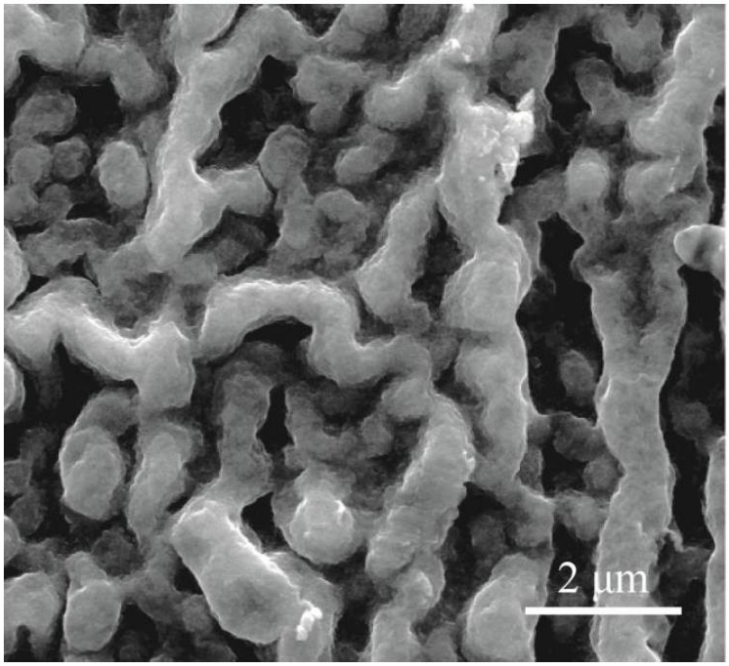

Figure 6.13 SEM image of AIS deposited onto Mo substrate using spray pyrolysis.

The nominal ratio for Sn doping was very similar to the actual amount of Sn determined by using energy dispersive X-ray spectroscopy (EDS) in conjunction with

SEM (Table 6.1). The compositions [wt % and at %] of the films determined by EDS are shown in Table 6.2

Table 6.1 Value of x = [Sn]/([Ag]+[In]) in Sn-doped AIS as determined by EDS

	x = 0		x = 0.02		x = 0.04		x = 0.06		x = 0.08	
Element	Wt%	At%	Wt%	At%	Wt%	At%	Wt%	At%	Wt%	At%
Ag	44.06	31.03	43.93	31.45	43.90	31.71	41.64	30.13	38.21	26.98
In	37.23	24.63	36.82	24.76	35.40	24.02	35.18	23.91	36.97	24.52
S	18.71	44.33	17.79	42.83	17.30	42.04	17.29	42.08	18.79	44.63
Sn	0	0	1.47	0.956	3.40	2.23	5.90	3.88	6.03	3.87

Table 6.2 EDS results on undoped and Sn-doped AIS films

	x = [Sn]/([Ag]+[In])			
Nominal ratio	0.02	0.04	0.06	0.08
Actual ratio	0.017	0.04	0.0718	0.0751

6.4.3 Optical Characterization

The transmission data for the AIS films with different amounts of Sn doping showed that about 50–60 % of the light was transmitted for wavelengths >700 nm (Figure 6.14A). The curvature of the transmitted light began to increase at 650 nm, which corresponds to the bandgap (E_g) of AIS. The transmittance was lowest for the undoped AIS sample and increased with Sn doping; the sample with x=0.02 showed the highest transmittance of approximately 60 %. This may reflect a change in the crystalline quality of the AIS films upon Sn doping. The films with x=0.02 may show a lower density of native defects than the other Sn doping concentrations, which results in a higher transmittance.[163]

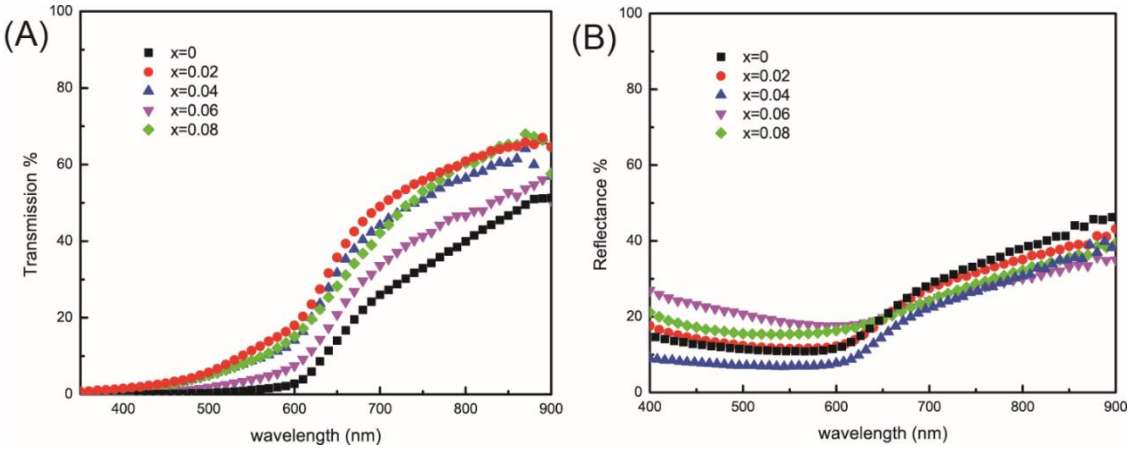

Figure 6.14 (A) Transmission and (B) reflectance data for AIS films with various amounts of Sn doping.

The absorption characteristics of the AIS films and E_g were determined by using diffuse reflectance instead of transmission because of the surface roughness of the films. In the diffuse reflectance spectra (Figure 6.14B), other than the sharp decrease around E_g, the reflectance increased as the wavelength decreased below 500 nm. The direct bandgap was acquired from the linear extrapolation of the Tauc plot to the x axis (Figure 6.15A).

There were some variations in the calculated E_g among samples with the same composition because of the surface roughness of the films. The thickness of the AIS films was approximately 350–500 nm. Bulk AIS is a direct bandgap semiconductor with $E_g \approx 1.8$ eV. The AIS films showed direct bandgaps that range from 1.833±0.004 eV for undoped AIS to 1.703±0.133 eV for x=0.08. The average E_g and root-mean-square deviation over three films for each composition are shown in Table 6.3. E_g was observed to increase for x=0.02, but then decreased when x>0.04. The increase in E_g with increasing Sn doping from x=0 to 0.04 can be a result of the increased presence of the higher E_g o-AIS phase, as shown by XRD. Our DFT calculations also suggest that Sn doping can decrease the E_g of AIS, which can explain the decrease in E_g when x>0.06. The absorption coefficients for the films were 10^5 cm^{-1} in the visible range, consistent with previous reports for AIS.

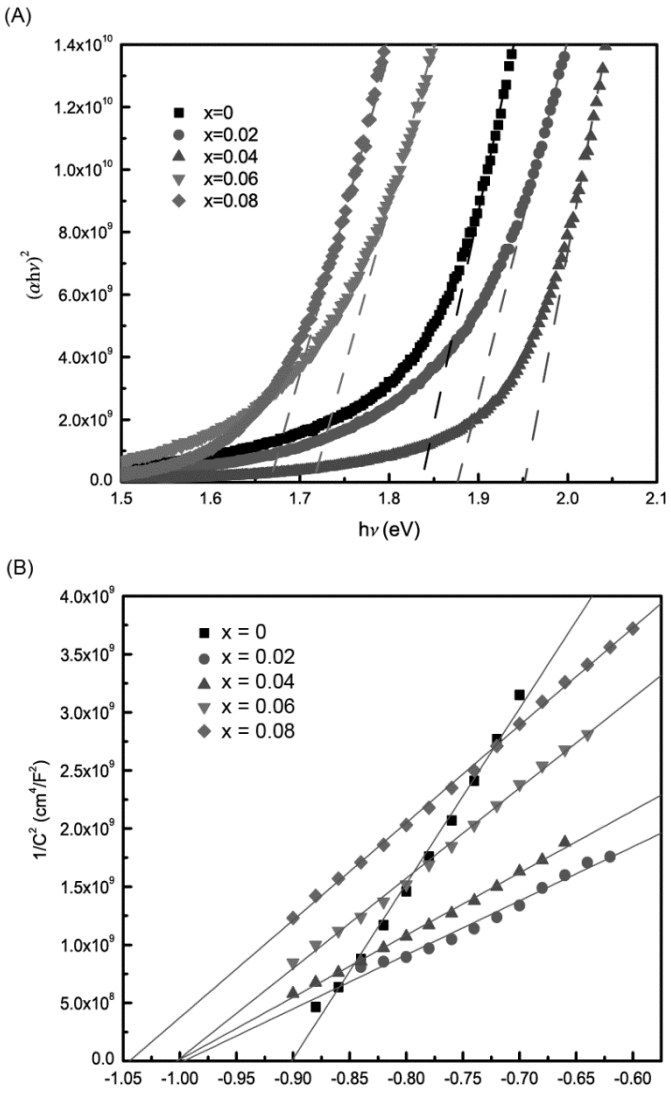

Figure 6.15 (A) Tauc plot from diffuse reflectance spectra and (B) Mott-Schottky plots for AIS films with different amounts of Sn doping.

Table 6.3 Average bandgap and standard deviation for AIS films with different ratios of Sn doping, for which x = [Sn]/([Ag]+[In]).

x	0	0.02	0.04	0.06	0.08
Average bandgap (eV)	1.833	1.876	1.919	1.746	1.703
Standard deviation	0.0042	0.063	0.03	0.027	0.131

6.4.4 Photoelectrochemical Analysis

The flatband potential (V_{fb}) corresponds to the applied voltage needed to flatten the bands, or remove the band bending, at the semiconductor–electrolyte interface. Determination of V_{fb} can identify the location of the Fermi level of the semiconductor. There are three methods to determine V_{fb}: 1) the open circuit voltage upon illumination, 2) the photocurrent onset potential in linear sweep voltammetry (LSV) measurements, and 3) Mott–Schottky (M–S) analysis.[169] All three of these measurements were performed for the AIS films with an electrolyte that contained Na_2SO_3 (0.25 M) and Na_2S (0.35 M, pH 13). Figure 6.16 shows the V_{fb} obtained from the illuminated open circuit voltage and photocurrent onset for AIS samples with different amounts of Sn doping annealed under N_2 or S after deposition. M–S analysis was performed only for AIS samples annealed under N_2.

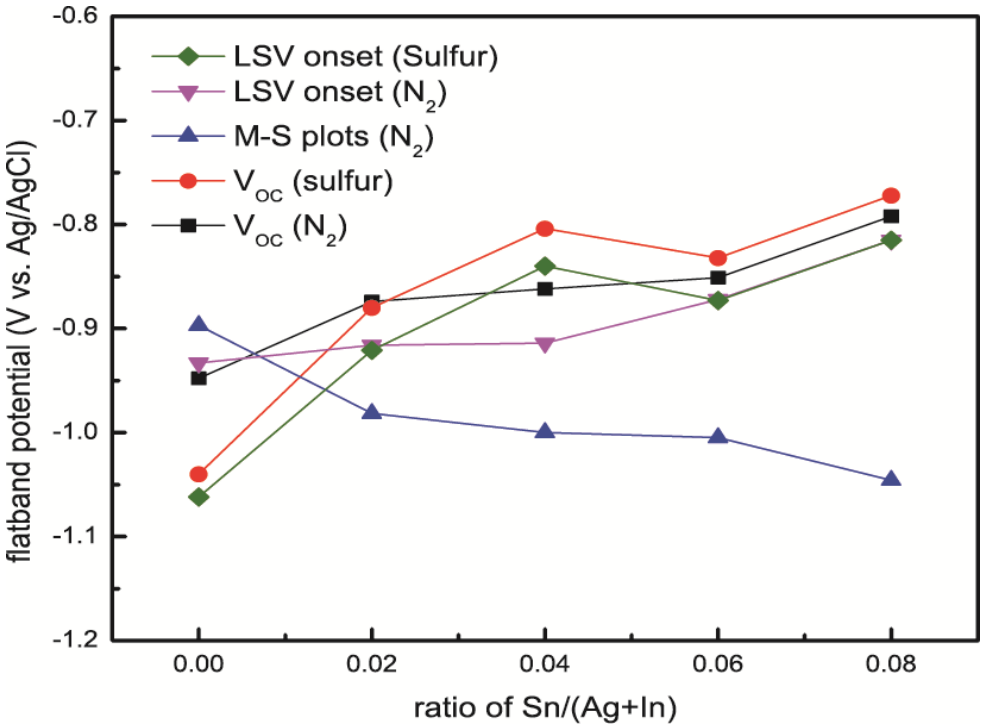

Figure 6.16 Comparison of flatband potentials obtained for AIS films with different Sn doping using the potential of photocurrent onset in a linear scan voltammetry (LSV) measurement after annealing in N_2 or sulfur atmosphere, Mott-Schottky analysis for films annealed in N_2, and the illuminated open circuit voltage (V_{oc}) for films annealed in N_2 or sulfur atmosphere.

All of the samples, even with Sn doping and annealing in S, displayed n-type behavior. This was evident from the change to negative potentials under illumination under open circuit conditions, by the positive slope of the M–S plots (Figure 6.15B), and by the photoanodic behavior (Figure 6.17), although there were variations in the V_{fb}values obtained. From the illuminated open circuit voltage measurements, V_{fb} became increasingly positive with larger amounts of Sn doping (Figure 6.16). However, the V_{fb} position acquired from M–S data decreased with larger amounts of doping. This

may be because the light intensity used for the open circuit voltage measurements was not strong enough to flatten the bands near the electrolyte interface. M–S plots have also been shown to give V_{fb} values approximately 0.1 eV more positive than the photocurrent onset value, which may cause the discrepancy.

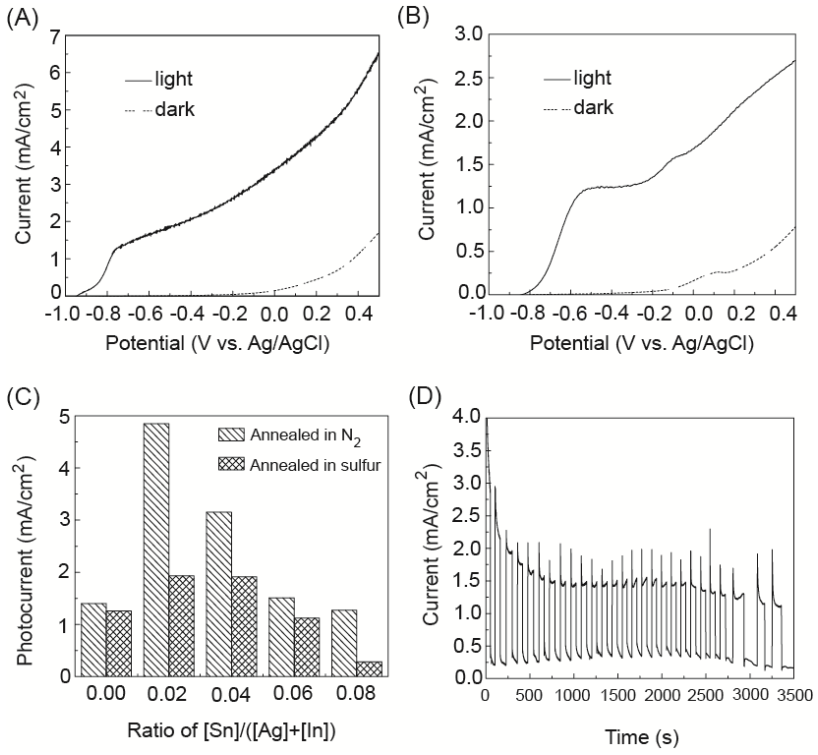

Figure 6.17 (A) LSV of Sn-doped AIS with x = 0.02 after annealing in N_2 and (B) x = 0.04 after sulfur annealing (C) Photocurrent of undoped and Sn-doped AIS samples at 0.5 V vs. Ag/AgCl, (D) Stability test of Sn-doped AIS with x = 0.02 after annealing in N_2 evaluated in 0.5M Na_2SO_4 solution

These data contradict the previous results obtained by Albor-Aguilera *et al.*[166] wherein p-type conduction, determined by using hot-probe methods, was observed with Sn doping in AIS. Moreover, the S annealing conditions used here were not effective to make the

AIS films p-type. S annealing to fill S vacancies is a common strategy to prepare p-type chalcopyrites,[151, 170] but the conditions used here do not seem to be effective for producing p-type AIS films.

Determination of the carrier concentration from the slope of the M–S plots showed that the carrier concentration increased with Sn doping at x=0.02, but then decreased with increasing Sn doping (Table 6.4). As suggested by the transmission data, this may reflect a difference in the defect density of the AIS films.

Table 6.4 Flatband position V_{fb} and major carrier concentration N calculated from M–S analysis of AIS films with x=[Sn]/([Ag]+[In]).

x	0	0.02	0.04	0.06	0.08
V_{fb}	-0.897	-0.982	-1	-1.005	-1.046
N	$1.43*10^{19}$	$4.66*10^{19}$	$4.17*10^{19}$	$2.88*10^{19}$	$2.68*10^{19}$

Annealing the spray-deposited samples was required to obtain the chalcopyrite structure, as discussed above. Annealing under a N_2 or S atmosphere had a notable effect on the photoelectrochemical performance. All of the AIS samples showed n-type photoanodic behavior. As the electrolyte contained Na_2SO_3 and Na_2S, which act as sacrificial hole scavengers, the anodic reactions are shown in the below [Eqs. (5.5)–(5.10)]:[167]

$$2H_2O+2e^- \rightarrow 2H_2+OH^- \quad (5.5)$$

$$SO_3^{2-}+H_2O+2h^+\rightarrow SO_4^{2-} \quad (5.6)$$

$$2S^{2-}+2h^+\rightarrow S_2^{2-} \quad (5.7)$$

$$S_2^{2-}+SO_3^{2-}\rightarrow S_2O_3^{2-}+S^{2-} \quad (5.8)$$

$$SO_3^{2-}+S^{2-}+2h^+\rightarrow S_2O_3^{2-} \quad (5.9)$$

in which h^+ indicates a photogenerated hole from AIS. The cathodic reaction was H_2O reduction by using the photogenerated electron (e^-) to form H_2 on the Pt counter electrode [Eq. (5.5)].

LSV was used to evaluate the photoanodic performance of the AIS films (Figure 6.17). The highest photocurrents obtained at 0.5 V versus Ag/AgCl are listed in Figure 6.17C. For undoped AIS, the highest photocurrent was 1.4 mA cm^{-2} (Figure 6.17C). Sn doping increased the photocurrent to 4.85 mA cm^{-2} for x=0.02 (Figure 6.17A), but the photocurrent dropped with increasing values of x, for which x=0.08 gave very similar photocurrents to the undoped AIS for samples annealed under N_2.

Although annealing CIS in a S atmosphere can improve its conductivity and turn it into a p-type material, AIS films treated under similar conditions remained n-type and showed lower photocurrents compared to those annealed under N_2, for which the highest photocurrent of approximately 2 mA cm^{-2} was observed for x=0.02 and 0.04 (Figure 6.17 B and C). Previous studies on the room-temperature electrical properties of AIS found that AIS films annealed under a minimum S pressure had a resistivity five orders of magnitude lower than n-AIS films annealed under a maximum S pressure.[151] S annealing has also been shown to change AIS from n- to p-type, but the p-type films also had a several orders of magnitude higher resistivity. These observations, along with our PEC

data, can be explained by the fact that S vacancies in AIS are donors and that S annealing can remove these donor levels, decrease the carrier density, increase the resistivity, and decrease the photocurrent.

The energy-band diagram of a semiconductor can be constructed by using V_{fb} and the calculated bandgap. For n-type semiconductors, the conduction band edge is approximately 0.1–0.2 eV higher than the V_{fb} value.[154] The V_{fb} determined by M–S analysis was −1.0 V versus SCE in the pH 13 electrolyte, and the bandgap was approximately 1.83 eV. Based on these conditions, the band edges for the conduction and valence bands for AIS are shown in Figure 6.18. The band edges for the commonly studied photoanodes TiO_2, WO_3, and Fe_2O_3 are also shown for comparison.[154] The band edges for AIS straddle the H_2 and O_2 redox potentials, which indicate that it is suitable for overall H_2O splitting without additional voltage bias, unlike WO_3 and Fe_2O_3. It also has a higher overpotential for H_2 evolution than TiO_2. However, as mentioned previously, sulfide semiconductors are not typically stable to photocorrosion. To confirm this, the stability of a Sn-doped AIS film with x=0.02 was evaluated at 0 V versus Ag/AgCl in a Na_2SO_4 solution (0.5 M, pH 7) under chopped light. In this environment, the initial photocurrent was approximately 2.1 mA cm^{-2}, which decreased to approximately 1.2 mA cm^{-2} at which it was stable for approximately 1 h (Figure 6.17D). After 1 h, the photocurrent remained at 50 % of its original value. This result indicates that AIS may suffer from degradation without a sacrificial reagent or protective coating from photo-oxidative corrosion, similar to other sulfide materials.[155]

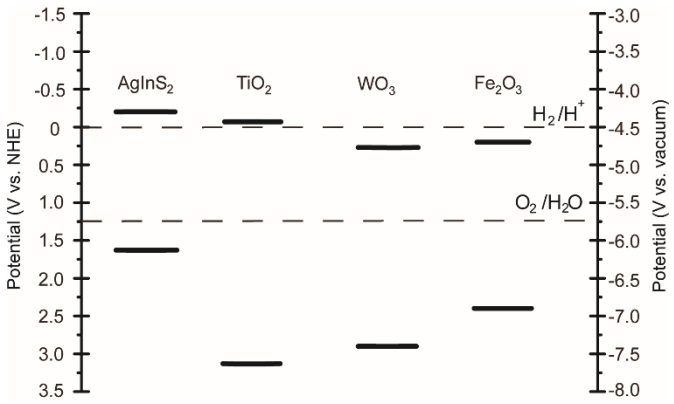

Figure 6.18 Band edges for $AgInS_2$ and other commonly studied photoanodes at pH 0.

6.4.5 DFT Calculations

DFT calculations were performed to understand how the band structure of AIS changed after Sn doping and to better understand the location of the Sn dopants in the AIS structure. The previously observed p-type behavior in Sn-doped AIS was attributed to Sn located at S sites.[171] The dopant-formation energy for Sn to occupy a Ag, In, S, or interstitial site in AIS (Figure 6.19) was calculated for each of the different doping ratios used (Table 6.5). The results show that the Sn dopants prefer to occupy interstitial sites until high doping ratios (x=0.125). Moreover, Sn in an S site is highly unfavorable.

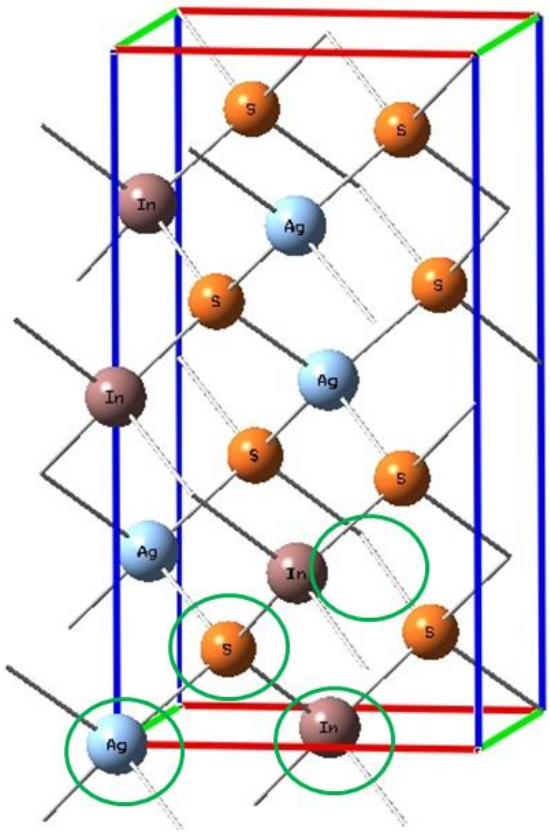

Figure 6.19 Host lattice of $AgInS_2$ (unit cell) showing possible sites that Sn can occupy circled in green: at a Ag-site, S-site, In-site, or interstitial site.

Table 6.5 Formation energies for Sn dopants at different sites in AIS with varying doping ratios (x=[Sn]/([Ag]+[In]).

x	Ag site	In site	S site	Interstitial
0.02	1.0	1.0	3.6	0.11
0.031	1.1	1.0	3.6	-0.023
0.0625	1.2	1.1	3.6	-0.04

0.125	1.1	1.0	1.9	2.7

To further investigate the Sn-doping effect, the electronic band structures and density of states (DOS) of pure AIS and Sn doped into an interstitial site in AIS for x=0.031 and 0.125 were calculated (Figures 6.10, 6.11, and 6.12).

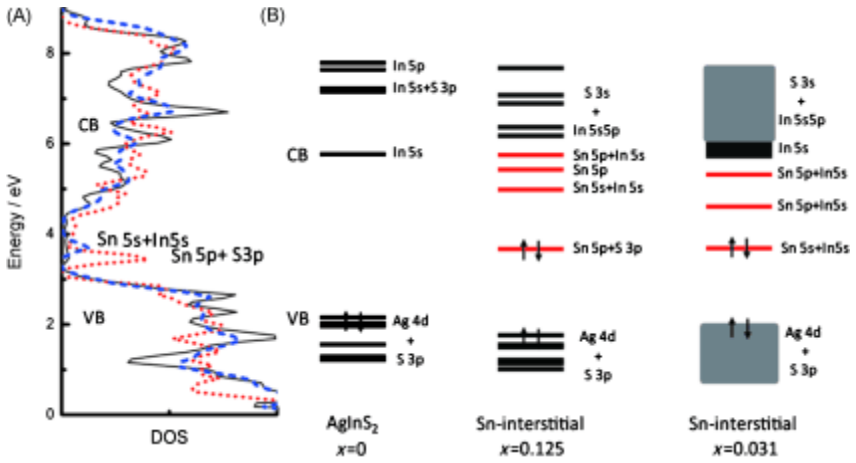

Figure 6.20 (A) DOS near the bandgap for x=0 (—), 0.031 (- - - -), and 0.125 (· · ·) and (B) energy diagram (with the energy levels at Γ in the Brillouin zone) for pure AIS and interstitial Sn-doped AIS at x=0.031 and x=0.125.

The undoped AIS and Sn-doped AIS with x=0.125 were calculated based on the AIS unit cell, whereas the x=0.031 band diagram was predicted by using a 2×2×1 supercell. Therefore, the x=0.031 case has a higher DOS and the energy levels form bands. The conduction band of pure AIS was found to be dominated by In 5s and S 3p orbitals, whereas the valence band is occupied by Ag 4d and S 3p electrons. The addition of Sn into the interstitial sites resulted in the formation of three shallow donor levels and a deep acceptor level (Figure 6.20B). This deep acceptor level is composed of Sn 5p and S 3p

orbitals for x=0.125, whereas it is composed of Sn 5s and In 5s orbitals for x=0.031. Close examination of the DOS near the region of the bandgap revealed that the conduction and valence band edges for pure AIS and Sn-doped AIS with x=0.031 matched well (Figure 6.20A). However, the bandgap for x=0.125 looks smaller, which indicates that higher Sn doping can reduce the bandgap of AIS, consistent with our experimental results (Table 6.3, Figure 6.15A). The DOS results also show that the deep acceptor level introduced by the Sn dopants increased proportionally with the amount of Sn and shifted towards the valence band for x=0.125. This reflects the contribution from the S 3p orbital to the deep acceptor level.

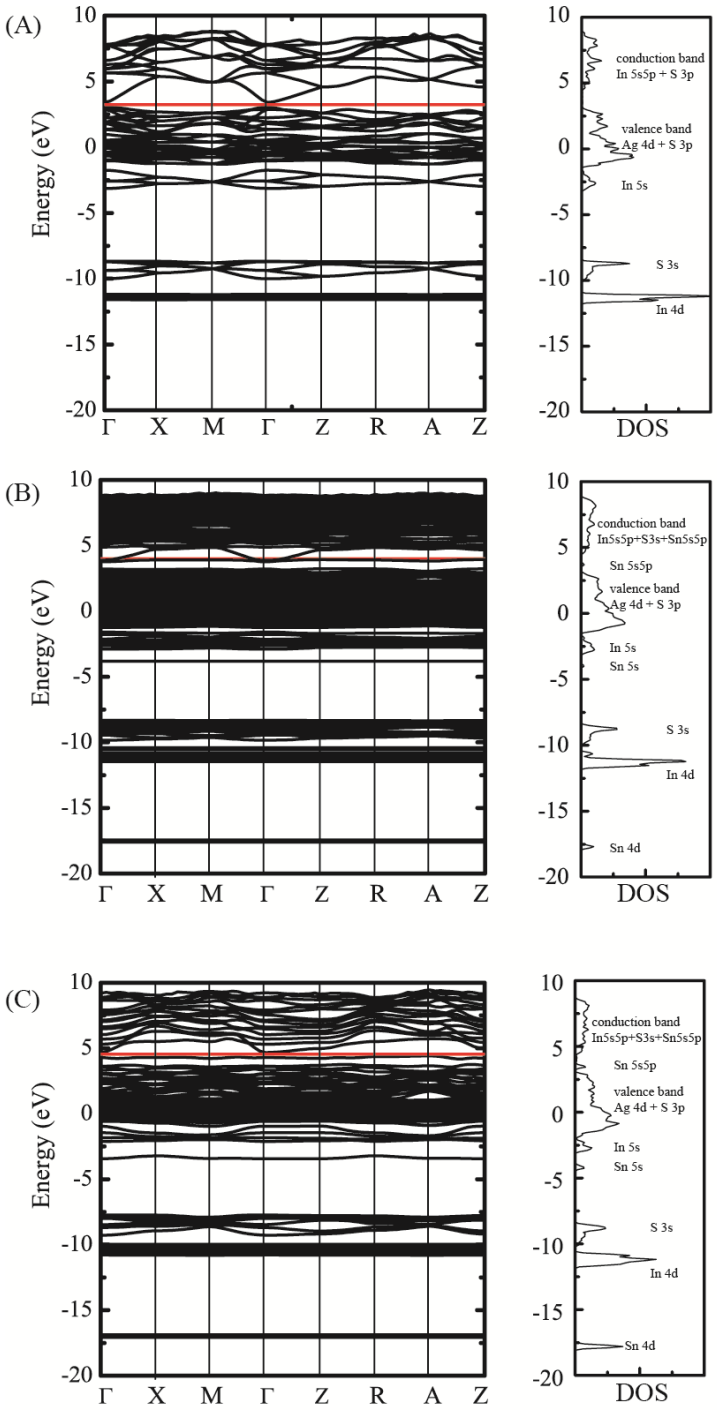

Figure 6.21 Calculated DOS and band structure of AIS with different ratio of Sn-doping where x = (A) 0, (B) 0.031, and (C) 0.125.

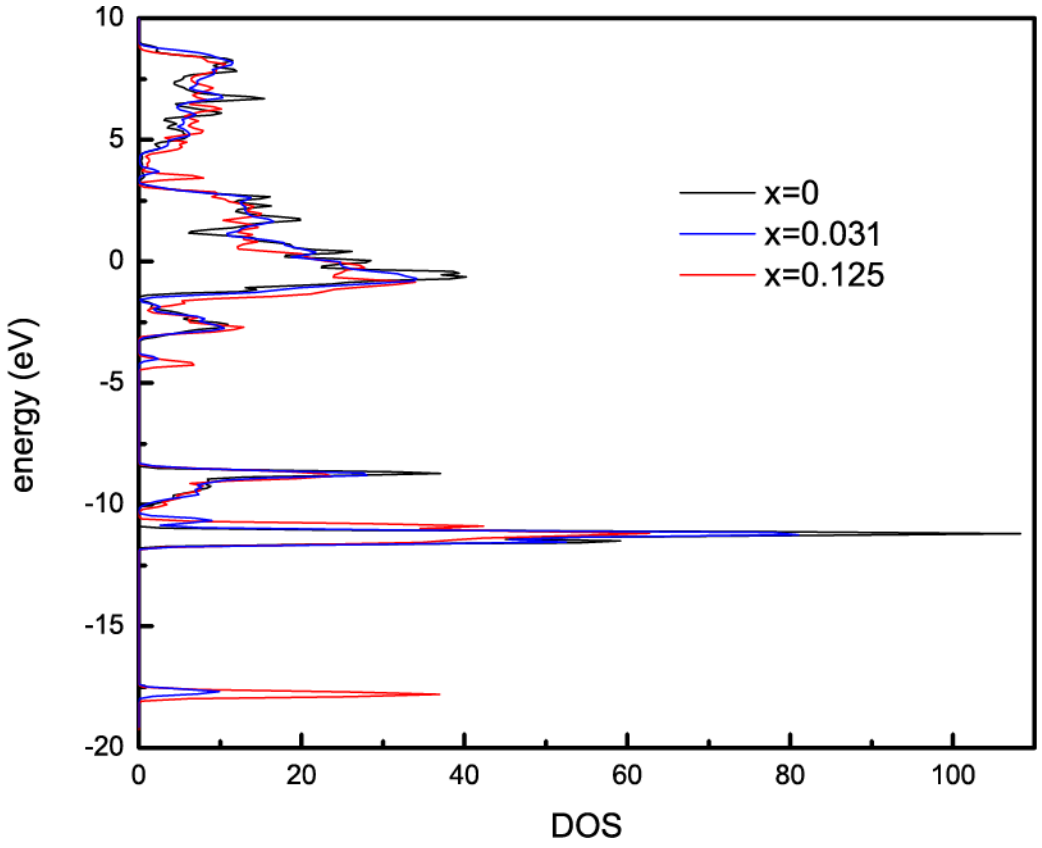

Figure 6.22 Density of States (DOS) for undoped AIS and Sn-doped AIS with Sn occupying an interstitial site. The DOS were aligned using the In 4d bands for comparison purposes.

We believe that the photocurrent data in Figure 6.17 C can be explained as follows. The shallow donor levels introduced by the Sn dopants can result in an increase in the carrier concentration, consistent with the M–S results (Table 6.4), which can lead to higher photocurrents. However, at higher doping levels, the deep acceptor level is closer to the valence band, which increases the likelihood that the concentration of holes can be increased. This will cause the donor and acceptor levels to compensate each other, which

decreases the major carrier concentration, consistent with the M–S analysis and photocurrent data. Such self-compensating effects have been observed in Sb-doped AIS in which the introduction of Sb allowed the preparation of AIS that is p-type but also highly resistive.

Moreover, it is well known that deep levels that are near the center of the bandgap can act as recombination centers and decrease the lifetime of carriers. As the DOS of the deep acceptor level increases with increased Sn doping, increased recombination can occur, which leads to lower photocurrents. This is consistent with our photocurrent data (Figure 6.7C) as well as the carrier concentrations derived from M–S analysis (Table 6.4).

Both the experimental and computational results show that small amounts of Sn doping into AIS can result in a higher photocurrent performance (for which x=0.02 gave the highest value), although increasing the amount of dopant can be detrimental. However, even with the optimized amount of Sn dopant, the observed photocurrents were much lower than the theoretical maximum photocurrent of about 20 mA cm^{-2} based on the 1.8 eV bandgap for AIS.[169] This indicates that there may be other factors involved that can affect the photoelectrochemical performance such as surface states. Surface states have been found to play a large role in surface recombination in Cu-chalcopyrite photocathodes, in which negligible photocurrents are often observed if surface passivation through coating with another semiconductor or cocatalyst decoration is not used to improve charge separation. Similar strategies may also be used for AIS and are currently under investigation.

6.5 Conclusions

Spray pyrolysis was successfully used to synthesize thin films of n-type $AgInS_2$ with a chalcopyrite structure. The properties and PEC performance of AIS were found to depend on both intrinsic defects and extrinsic dopants. Annealing under N_2 resulted in higher photocurrents, likely a result of the formation (or maintenance) of S vacancies that act as donors. Sn doping at a ratio of 0.02 gave the highest photocurrent, but higher amounts of Sn resulted in decreased photocurrents and carrier concentrations. DFT results showed that Sn dopants likely occupy interstitial sites and that Sn introduced shallow donor levels and a deep acceptor level, of which the latter can act as a recombination site at higher Sn doping concentrations.

7 NANOMATERIALS AS PHOTOCATALYST FOR WATER TREATMENT

7.1. Introduction to Cr (VI) Treatment

Chromium is a regulated metal and abundant in ground waters as a naturally occurring metal or contaminant from industrial processes related to mining, electroplating, metal finishing, and pigments, among others [172, 173]. Hexavalent chromium [Cr(VI)] compounds are carcinogenic and have been found to be anywhere from 10-1000 times more toxic than trivalent [Cr(III)] chromium compounds [174]. In aqueous solutions with pH 6 – 8, the most probable Cr(VI) species are chromate, CrO_4^{2-}, and bichromate, $HCrO_4^-$, both of which are very soluble anions that cannot form precipitates [175]. Studies have also shown that Cr(III) can become oxidized to Cr(VI) during chlorination of water [176]. For this reason, many treatment strategies have centered around reduction of Cr(VI) to Cr(III) species, which can form insoluble $Cr(OH)_3$ and be removed with adsorbents. Since Cr(VI) exists as negatively charged anion species, it can also be adsorbed onto surfaces of metal oxide sorbents if the pH of the solution is below the sorbent's point of zero charge (PZC), since the surface will be positively charged and promote electrostatic attraction. A list of PZCs, also known as isoelectric points (IEPs) for many common metal oxides and semiconductors has been compiled by Kosmulski [177].

One treatment method for removing chromium from water is to use photocatalysis. Photocatalytic degradation of harmful contaminants is becoming increasing attractive for wastewater treatment of dilute streams, particularly with ultraviolet (UV) light emitting diodes (LEDs), which are seen as reliable, continuous, and low-cost light sources.[178] When semiconductors are irradiated with light containing photons that are more energic than the bandgap of the semiconductor, electrons are generated that can be used for

reducing species. While photoexcited electrons are commonly exploited for reducing protons in water to generate hydrogen gas [179], these electrons can also be used to remove harmful contaminants for water treatment applications, such as reducing Cr(VI) to Cr(III) (Figure 7.1A). In general, photocatalytic reduction is possible when the standard reduction potential of the reactant is more positive than the conduction band of the photocatalyst (Figure 7.1B), although several hundred millivolts of overpotential are often required due to ohmic, kinetic, and mass transfer losses.[180]

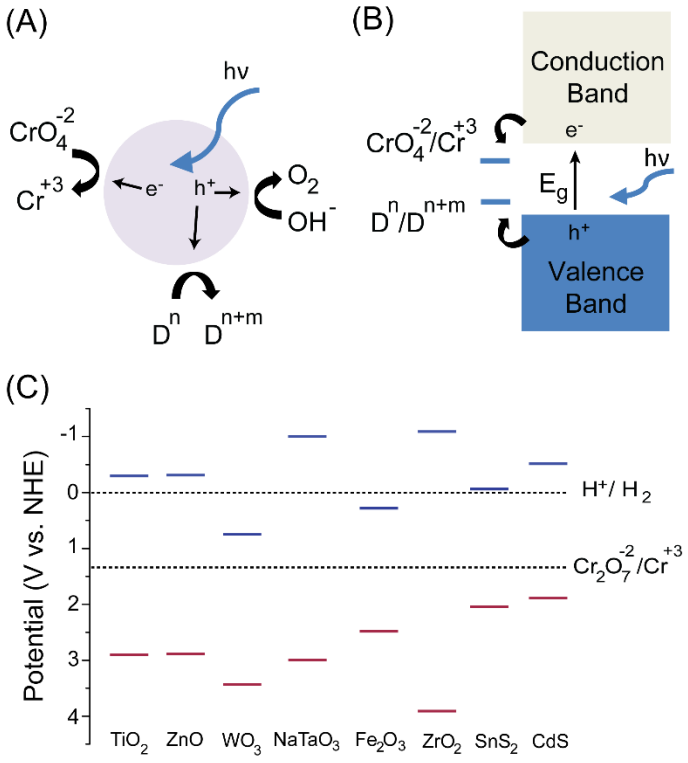

Figure 7.1 (A) Schematic depicting photocatalytic reduction of hexavalent chromium (shown here as chromate) using photogenerated electrons on a semiconductor photocatalyst particle. Photogenerated holes can oxidize water or an electron donor, D^n. (B) Band diagram depiction of Cr(VI) photoreduction. The photocatalyst band edges must straddle the redox potentials for Cr(VI)/Cr^{3+} and the sacrificial reagent. (C) Band

edges for common semiconductor photocatalysts at standard conditions (pH 0) with respect to the redox potentials for H_2 generation and Cr(VI)/Cr^{3+}. Conduction band edges are shown as blue lines and valence band edges in red.

Photocatalytic reduction of Cr(VI) using photogenerated electrons from metal oxide semiconductors is attractive as a chromium treatment method, since the material can double as the photocatalyst and adsorbent. The reduction potential of Cr(VI), which is present as dichromate ($Cr_2O_7^{2-}$) at standard conditions (e.g. pH 0), is E^0 = 1.36 V vs. RHE [181]. Most commonly studied wide bandgap semiconductors have conduction band minima [182] positive enough for the photoreduction of Cr(VI) to occur (Figure 7.1C). During light irradiation, photogenerated holes are also produced, which can be used to oxidize water or a sacrificial agent, D^n (Figure 7.1A). To be able to oxidize water, the valence band edge of the semiconductor must be more positive than the reduction potential for OH^-/O_2. The net reaction for Cr(VI) reduction and concurrent water oxidation in acidic and neutral environments are shown in Equations (7.1) and (7.2), respectively.

$$2Cr_2O_7^{2-} + 16H^+ \longrightarrow 4Cr^{3+} + 8H_2O + 3O_2 \qquad (7.1)$$

$$4CrO_4^{2-} + 20H^+ \longrightarrow 4Cr^{3+} + 10H_2O + 3O_2 \qquad (7.2)$$

From these equations, it is evident that Cr(VI) reduction is a multi-proton reduction process, making this reaction less favorable in alkaline environments. Furthermore, since most metal oxides have low PZCs, $Cr_2O_7^{2-}$ is easier to adsorb onto photocatalyst surfaces at lower pH. However, pH adjustment in real industrial applications, where there are large volumes or flow rates of water, may not be practical.

Even with suitable band edge energy, due to the slow kinetics of water oxidation, most metal oxides require an additional co-catalyst for water oxidation, such as RuO_2 or IrO_2[183]. Due to the high cost of these precious metal co-catalysts, a more feasible approach is to exploit additives that can act as sacrificial electron donors or hole scavengers. In water treatment processes, many chemical additives that are utilized, for example to adjust pH, de-chlorinate, or clean filters, may also serve as hole scavengers to promote the photoreduction of Cr(VI). At the same time, since water matrices in real water applications can be quite complex, it may also be possible for species in the water to obstruct the photocatalytic processes. Hence, it is important to evaluate photocatalysts in industrially relevant water solutions rather than solely in simulated solutions consisting of de-ionized water spiked with Cr(VI).

Here we report the evaluation of UV-absorbing photocatalysts for Cr(VI) reduction and removal in synthetic solutions as well as in water samples obtained from the Salt River Project (SRP) Santan Generating Station. The Santan facility is a natural gas powered plant with approximately 1193 MW capacity in Gilbert, AZ used to supplement base-load plants and meet peak demand. The boiler and cooling water for the Santan Generation Station are sourced from onsite wells or surface waters. Groundwater in the SRP service area contains naturally occurring levels of chromium, which can become concentrated in cooling water blowdown and hence pose challenges for meeting regulatory discharge limits. The Arizona maximum contaminant level (MCL) for Cr(VI) is 27 ppb and the NPDES regulatory discharge limit is 11 ppb [184].

The conditions required for effective Cr(VI) reduction in these waters were investigated in a labscale photocatalytic reactor. The metal oxides studied were titanium

dioxide (TiO_2), zinc oxide (ZnO), tungsten trioxide (WO_3), and sodium tantalate ($NaTaO_3$). These materials were chosen because they have been well studied as photocatalysts for water splitting applications [185], and also have suitable conduction band energies for photocatalytic reduction of Cr(VI) (Figure 7.1C). Of these metal oxides, TiO_2 has been the most commonly investigated photocatalyst for the reduction of Cr(VI), both in powdered slurry configurations [181] and in photoelectrochemical cells [186]. In previous studies, WO_3 displayed the highest activity for photoreduction of Cr(VI) in acidic solutions when compared to TiO_2 (both rutile and anatase crystal phases), hematite (α-Fe_2O_3), and strontium titanate ($SrTiO_3$) photoelectrodes [187]. ZnO has also been used as a photocatalyst for Cr(VI) reduction with high efficiency [188], but may not be stable when the pH is lower than 5 or higher than 10. To our knowledge, $NaTaO_3$ has not been investigated as a photocatalyst for Cr(VI) reduction. Not only does $NaTaO_3$ have a high quantum yield for overall water splitting [189], it can also demonstrate stoichiometric H_2 and O_2 production without requiring a co-catalyst for water oxidation [190]. Hence, $NaTaO_3$ may also demonstrate promising activity for the photocatalytic reduction of Cr(VI) without the use of sacrificial hole scavengers. Table 7.1 summarizes the relevant properties of the photocatalysts used in this study, such as the conduction and valence band edge positions, bandgap (E_g), and PZC [177, 182, 191-194].

7.2. Experimental Section

7.2.1 Materials Characterization

WO_3 and ZnO were obtained from Sigma-Aldrich and used without further treatment. P90-TiO_2 was obtained from Evonik. $NaTaO_3$ was synthesized using a hydrothermal

reaction as described previously [195]. In a typical synthesis, 0.44 g Ta_2O_5 and 1.2 g NaOH were added to a Teflon lined stainless-steel autoclave (Parr, 50 mL capacity) that was filled with its 80% volume by DI water, heated to 140 ºC for 12 hours, then cooled to room temperature naturally and washed with DI water and ethanol for three times. The powder was dried in a vacuum oven for 2 hours at 50 ºC. X-ray diffraction (XRD, Panalytical X'pert Pro) and scanning electron microscopy (SEM, FEI XL30) were performed to determine the crystal structure and observe the morphology of the photocatalysts. The surface area of metal oxides was determined from N_2-adsorption experiments using Brunauer-Emmett-Teller (BET) surface area analysis (Micromeritics, Tristar II).

PZC values for P90 TiO_2, ZnO, and WO_3 were obtained from published reports [177, 191-193]. The PZC for $NaTaO_3$ was not available in the literature so zeta potential (ζ) measurements were performed using an electrophoretic mobility method (ZetaPALS, Brookhaven Instruments Corporation, U.S.). $NaTaO_3$ powder was added to 10 mM potassium nitrate and sonicated to create a 0.6 g/L suspension. The suspension was mixed for 24 hours in the dark to achieve equilibrium with the potassium nitrate ions. Immediately before ζ analysis, the suspension was re-sonicated. A range of pH values were chosen to determine the pH ZPC. The pH was adjusted using sodium hydroxide and nitric acid.

7.2.2 Water Solutions

Simulated Cr(VI) solutions were prepared by dissolving $K_2Cr_2O_7$ in ultrapure DI water (18.3 MΩ-cm) at either 10 or 1 ppm concentrations. The pH of the solution was adjusted

to 7 using NaOH and HCl. Water samples (pH 8.3) were obtained from the cooling tower blowdown at the Salt River Project Santan Generating Station, filtered to remove solids (polycarbonate filter membranes, 0.2 μm pore), and spiked with 1 ppm Cr(VI).

7.2.3 Photocatalytic Removal of Chromium

The photocatalysts were evaluated in a photoreactor composed of two borosilicate bottles (1.8 L, transmittance $\lambda > 280$ nm) submerged in a cooling tank with a medium-pressure mercury vapor lamp (450 W, Ace Glass, 7825-34) placed in a double-walled quartz immersion well (Ace Glass, 7854-25) [196]. The glass reactor (Ace Glass, 7841-05) temperature was maintained at 25 ^{o}C with a chiller. Previously, the light irradiance for the lamp in this photoreactor setup was determined to be 7.66 x 10^{-6} Einsteins/L-s (1.654 x 10^{18} photons/cm^2-min) for all wavelengths 280 – 500 nm using ferrioxalate chemical actinometry [196]. The usable photon flux, Φ, for each photocatalyst was approximated by including only the wavelengths that can be absorbed by the photocatalyst according to its bandgap. Since only photons with energy higher than the semiconductor bandgap can be absorbed and used to excite electrons from the conduction to valence bands, Φ was calculated by integrating the number of photons with energy E_g and higher. The spectrum of the lamp is shown in Figure 7.2F. The bandgaps and corresponding photon flux for each photocatalyst are listed in Table 7.1. The number of photons per cm^2, *N*, was then determined from the product of the irradiation time, *t*, and Φ as shown in Equation 7.3.

$$N = t\Phi \qquad (7.3)$$

To avoid direct photolysis of the organic hole scavengers, a quartz sleeve was placed around the lamp to filter out wavelengths below 285 nm. Due to the large bandgap of

$NaTaO_3$ (i.e., 310 nm), Cr(VI) reduction was not observed when the quartz sleeve was used. Therefore, the quartz sleeve was removed for all $NaTaO_3$ experiments. The photocatalysts were suspended at a concentration of 1 g/L. Prior to transfer into the photoreactor, the suspension was stirred in the dark for 15 minutes at 700 rpm and the mercury lamp was turned on for 30 minutes to stabilize the light. After light irradiation, the photocatalysts were removed from the photoreactor and recovered using vacuum filtration.

7.2.4 Regeneration of Photocatalyst

To study the ability of the photocatalyst to be reused multiple times, TiO_2 or $NaTaO_3$ were first used to reduce 10 ppm Cr(VI). After the reaction, the photocatalyst was recovered using vacuum filtration and washed with DI water for several times. Then the photocatalyst was dried at 60 ^oC for 2 hours, and re-dispersed in 200 mL of either 1 M HNO_3 or 3 M NaOH and sonicated for 3 hours. Finally, the photocatalyst was recovered with vacuum filtration, washed with DI water, then dried again for the next reuse cycle.

7.2.5 Analysis

The concentration of Cr(VI) remaining in the solution, which represents the amount of Cr(VI) that was not reduced or adsorbed onto the surface of the photocatalyst, was determined colorimetrically utilizing the 1,5-diphenylcarbohydrazide method in a DR-5000 UV-vis spectrometer with a TNT 854 reagent kit from Hach. Cr(III) recovered with acid or alkaline treatment of used photocatalyst was oxidized with sodium persulfate at 1

M NaOH solution by heating at 100 ^{o}C for one hour. Once the Cr(III) was oxidized to Cr(VI), it was analyzed colorimetrically as described above.

7.3 Results and Discussion

7.3.1 Materials Characterization

Figure 7.2 shows the SEM images of the photocatalyst particles with the XRD patterns inset. The ZnO particles (Figure 7.2A) were rod-shaped and ranged from 200 – 400 nm in size and adopted the hexagonal crystal structure (PDF 01-079-2205). The TiO_2 particles (Figure 7.2B) had a high surface area and the crystal structure was a mixture of anatase and rutile, consistent with the specifications for P90 [196]. The $NaTaO_3$ (Figure 7.2C) adopted a nanocube morphology and monoclinic crystal structure (PDF 01-074-2477). The WO_3 (Figure 7.2D) was in the form of nanoparticles about 100 nm in size with monoclinic structure (PDF 00-043-1035). The surface area of the photocatalysts were determined by BET and results are listed in Table 7.1 with an order of TiO_2 > WO_3 > ZnO > $NaTaO_3$. This trend is expected based on the particle sizes observed in the SEM. The low surface area of $NaTaO_3$ is caused by its smooth surfaces and cubic morphology. Figure 7.2E shows the ζ analysis for $NaTaO_3$ at various pH. The ZPC was at approximately 3.5.

Table 7.1 Properties of metal oxide photocatalysts for photoreduction of Cr(VI). The conduction band minimum (CBM) and valence band maximum (VBM) are provided at pH 0. The usable photon flux, Φ, represents the number of photons with energies higher than E_g that can be absorbed by each material in the photoreactor.

Photocatalyst	E_g (eV)	CBM	VBM	PZC	Surface Area (m^2/g)	Φ (photons/cm^2-min)
TiO_2	3.2	-0.29 V	2.91 V	5.8-6.7	92.60	7.14×10^{17}
ZnO	3.2	-0.31 V	2.89 V	8.8-9.5	7.71	7.14×10^{17}
WO_3	2.7	0.74 V	3.44 V	0.43-0.5	4.62	9.40×10^{17}
$NaTaO_3$	4.0	-1.00 V	3.00 V	3.5	1.57	1.55×10^{17}

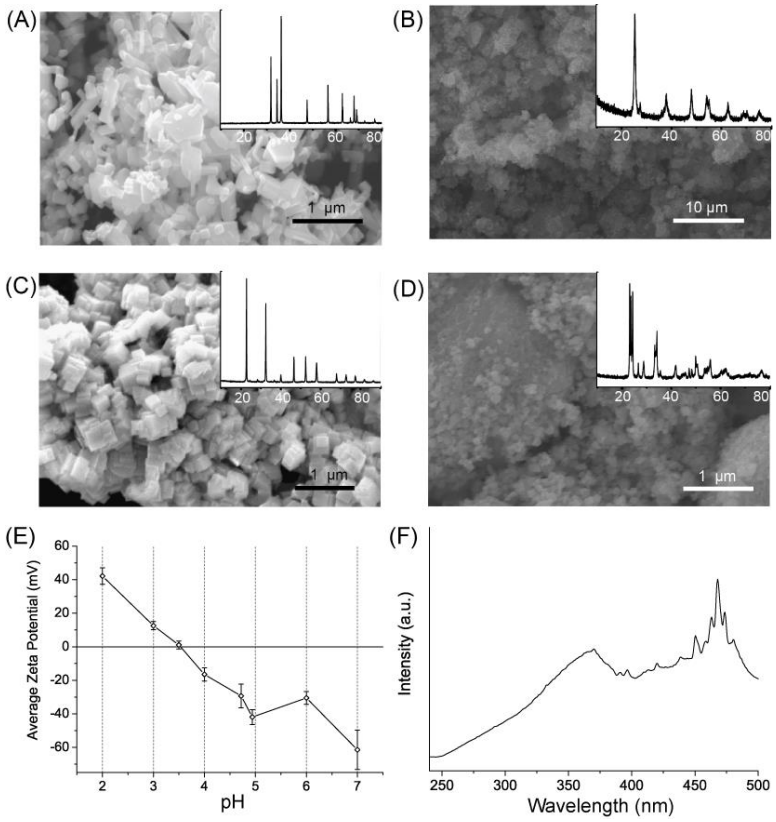

Figure 7.2 SEM images of photocatalysts used. Insets show the corresponding XRD patterns. (A) ZnO, (B) TiO_2, (C) $NaTaO_3$, (D) WO_3. (E) Zeta potential analysis for $NaTaO_3$ at various pH. (F) Emission spectrum of mercury lamp used in the photoreactor.

7.3.2 Cr(VI) Removal in DI Water

The photocatalysts were first evaluated in DI water at pH 7 spiked with 1 ppm Cr(VI). All four photocatalysts studied were found to be effective for Cr(VI) removal. Figure 7.3A shows the % Cr(VI) remaining as a function of irradiation time. TiO_2 and ZnO had similar removal efficiencies and removed Cr(VI) better than WO_3 and $NaTaO_3$ at pH 7. The apparent photocatalytic reduction rate constant, k_{Cr} was achieved by fitting the Cr(VI) reduction rate to a pseudo-first-order rate reaction, as shown in Equation (7.4).

$$\ln (C_t / C_o) = - k_{Cr} t \qquad (7.4)$$

C_t represents the concentration of Cr(VI) at the irradiation time *t* and C_o is the original concentration of Cr(VI). The results, shown in the first column of Table 7.2, show that TiO_2 and ZnO have the highest rate constants, both around 0.16 min^{-1}, followed by WO_3 and then $NaTaO_3$.

Table 7.2 Apparent kinetic constant k_{Cr} (min^{-1}) fitted from Cr(VI) reduction studies using different photocatalysts.

Photocatalyst	k_{Cr}^1	k_{Cr}^2	k_{Cr}^3
TiO_2	0.1590	0.7442	0.1180
ZnO	0.1626	n/a	0.1014
WO_3	0.0824	0.0467	n/a
$NaTaO_3$	0.0068	0.2555	0.0070

[1] C_0 = 1 ppm Cr(VI); DI water, pH 7; corresponds to data in Figure 7.3A

[2] C_0 = 10 ppm Cr(VI); DI water + formic acid, pH 3; corresponds to data in Figure 7.3C

[3] C_0 = 1 ppm Cr(VI); cooling tower blowdown, pH 8.3; corresponds to data in Figure 7.7A

Although the PZC of TiO_2 is lower than 7, it still displayed similar Cr(VI) removal as ZnO, which has a higher PZC. The higher surface area and smaller particle size of TiO_2 can be the reason for its similar activity as ZnO at this pH. While WO_3 and $NaTaO_3$ have low PZC (3.5 for $NaTaO_3$ and 0.41 for WO_3), photoreduction of Cr(VI) was still possible at pH 7, but with lower reduction rates compared to TiO_2 and ZnO.

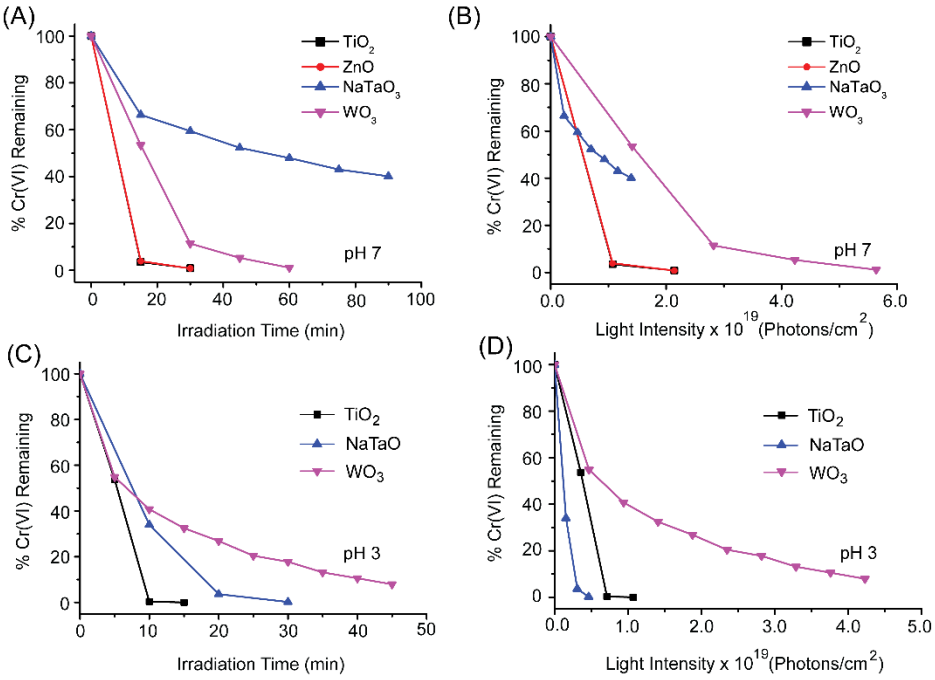

Figure 7.3 Photocatalytic reduction using 1 g/L photocatalysts of (A),(B) 1 ppm Cr(VI) in DI water at pH 7 and (C),(D) 10 ppm Cr(VI) in pH 3 with formic acid. The percentage of Cr(VI) remaining is presented at different irradiation time and usable light intensity.

Figure 7.3B shows the same Cr(VI) removal data, but as a function of light intensity, or photons per irradiation area (*N* from Equation (7.3)). We point out that the light intensity here is showing the number of usable photons based on their energies with respect to the photocatalyst bandgap, without taking into consideration the number of photons that are actually absorbed and not, for instance, scattered outside the reactor without being absorbed. Photon losses due to scattering is an important factor to consider when overall photocatalystic efficiencies are concerned, [197] but is highly dependent on the reactor design. In this study, the photoreactor takes advantage of inner illumination, so that the photocatalyst suspension completely surrounds the light source, and scattering is not considered. Rather, analyzing the removal rate according to the usable photon basis is performed as it is important when comparing photocatalysts with different bandgaps, since lower bandgap materials will absorb a larger portion of the light spectrum. While applications using solar light stress the importance of low bandgap (e.g. 1.1 – 2.0 eV) semiconductors for maximum solar energy conversion efficiency [198-200], water treatment applications using UV photocatalysis are more concerned with the treatment time and removal efficiency. In terms of removal efficiency based on the number of usable photons, TiO_2 ~ ZnO > $NaTaO_3$ > WO_3, as shown in Figure 7.3B. Although WO_3 has a smaller bandgap compared to TiO_2 and ZnO, allowing it to absorb a broader range of photon energies, it still required almost three times as many photons as TiO_2 and ZnO to reach complete removal of the Cr (VI).

The solution pH was then adjusted to 3 using excess formic acid (0.3 g/L), which can also serve as a sacrificial hole scavenger. The solution pH is an important factor in Cr(VI) reduction due to the large number of protons needed (Equations 7.1 – 7.2).[201] ZnO was

not used as the photocatalyst in this case, since it can easily dissolve at this pH. The Cr(VI) removal rate greatly increased using the other three photocatalysts at pH 3 (Table 7.2, middle column), with all of the Cr(VI) (10 ppm initial concentration) reduced in 30 min using $NaTaO_3$ and TiO_2. Despite its higher bandgap, $NaTaO_3$ exhibited more efficient Cr(VI) removal on a photon basis than TiO_2 at pH 3 (Figure 7.3D), which is lower than the PZC for both materials. Additionally, the $NaTaO_3$ particles had a lower surface area than TiO_2. These results suggest a higher intrinsic activity for Cr(VI) reduction on $NaTaO_3$ compared to TiO_2. The origin of this activity is not known, but possibly can be due to the much more negative conduction band edge energy in $NaTaO_3$, resulting in a higher overpotential for Cr(VI) reduction compared to TiO_2 (Figure 7.1C). The Cr(VI) removal rate on WO_3 was also accelerated at pH 3 compared with pH 7, but WO_3 still needed more than eight times the photons compared with $NaTaO_3$ to achieve the same removal percentage. This can similarly be explained by the positive conduction band minimum for WO_3, giving it less overpotential for Cr(VI) reduction. The low performance of WO_3 compared to $NaTaO_3$ and TiO_2 can also be due to its low PZC value of 0.43, resulting in a negative surface charge at pH 3.

From these results, we can see that the Cr(VI) removal rate is highly dependent on different factors of the metal oxide, such as PZC, surface area, bandgap, and conduction band minimum, and cannot easily be predicted from just one of these properties.

7.3.3 Effect of Additives

To better understand the effect of the water matrix on the photocatalytic removal of Cr(VI), several chemicals that are commonly used in the water treatment processes were

added separately into DI water spiked with 10 ppm Cr(VI). Ammonium hydroxide is commonly used in boiler treatment as a corrosion inhibitor. Citric acid is used intermittently to clean the reverse-osmosis filters. Sodium bisulfite ($NaHSO_3$) and sodium metabisulfite ($Na_2S_2O_5$) are used as de-chlorination agents often at 1-1.3 times excess.

The results for the effect of ammonium chloride (1 g/L), citric acid (0.175 g/L), sodium sulfite (0.4 g/L), and sodium formate (0.04 g/L) on Cr(VI) removal using $NaTaO_3$ as photocatalyst are shown in Figure 7.4. The addition of additives slightly changed the solution pH so it was adjusted back to 7 with either NaOH or HCl, the exception being Na_2SO_3. When using Na_2SO_3, the solution pH was maintained at 8.45, in order to better simulate the SRP cooling tower blowdown. Compared to the results where the Cr(VI) was prepared in DI water only, the addition of sodium formate, sodium sulfite, and ammonium chloride improved the rate of Cr(VI) reduction by $NaTaO_3$, whereas introduction of citric acid decreased it. These results can be explained as follows.

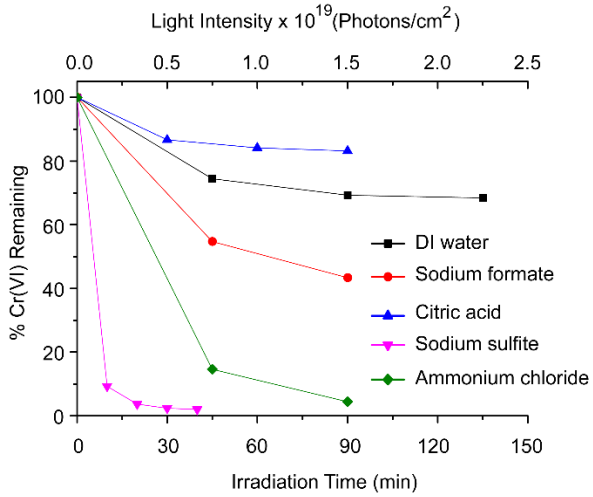

Figure 7.4 Photocatalytic reduction of 10 ppm Cr(VI) using 1 g/L $NaTaO_3$ photocatalyst in DI water with and without additives. All solutions were pH 7, except for that

containing Na_2SO_3, which was pH 8.45. The percentage of Cr(VI) remaining at different irradiation time (bottom axis) and usable light intensity (top axis).

Ammonium can act as a good hole scavenger and enhance the Cr(VI) removal, which was previously observed with TiO_2 photocatalysts [202]. The final oxidized product of ammonium oxidation is likely nitrate, as shown in Equation (7.4). During ammonium oxidation, protons are produced, which would slow down the pH increase that occurs due to proton consumption during Cr(VI) reduction, as shown in Equation (7.1). This pH stabilization can also serve to enhance the Cr(VI) reduction.

$$NH_4^+ + 3H_2O \rightarrow NO_3^- + 8e^- + 10H^+ \qquad (7.4)$$

Similar to formic acid, adding citric acid to the water decreased the pH to 3, which enhanced the photoreduction reaction and decreased the Cr(VI) concentration by > 98% after 90 minutes (not shown). However, when NaOH was added along with the citric acid to maintain a neutral solution pH, the Cr(VI) removal on $NaTaO_3$ was markedly decreased compared to the additive-free DI water solutions (Figure 7.4). These results show that at neutral pH, citric acid does not act as a hole scavenger to enhance Cr(VI) reduction. This can be due to the fact that the tertiary hydroxyl and three carbonyl groups make oxidation of citric acid more difficult compared to other organic acids [203]. Moreover, at pH 7, citric acid is completely deprotonated (pKa_3 = 6.40) with three negatively charged carboxylic acid groups. At this pH, the surface of $NaTaO_3$ is negatively charged, which would make it difficult for citrate ions to adsorb onto the surface.

As shown in Figure 7.4, the presence of sulfite resulted in the fastest Cr(VI) removal on $NaTaO_3$. A series of experiments was conducted to determine the optimum amount needed. These studies were first performed using all the photocatalysts and the results are shown in Figure 7.5. When using 0.4 g/L sodium sulfite with TiO_2, ZnO, and WO_3, all of the Cr(VI) (10 ppm starting concentration) was removed within 15 minutes (Figure 7.5A). The Cr(VI) removal on $NaTaO_3$ was slower on the time scale due to its larger bandgap, but it was the most efficient when considering the photon basis (Figure 7.5B).

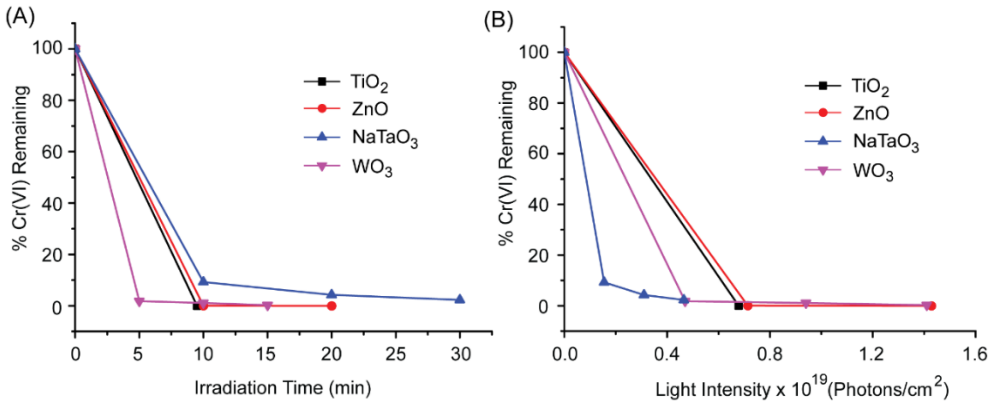

Figure 7.5 Photocatalytic reduction of 10 ppm Cr(VI) using photocatalyst at 1 g/L in DI water with 0.4 g/L Na_2SO_3 at pH 8.45. The percentage of Cr(VI) remaining (A) at different irradiation time and (B) usable light intensity.

Sodium sulfite, bisulfite, and metabisulfate have been shown to act as very effective chemical reductants of Cr(VI), with fast and complete reduction at pH 2 –5 [204]. The reduction reaction with sulfite is shown in Equation (7.5).

$$2\,CrO_4^{2-} + 3\,SO_3^{2-} + 10H^+ \rightarrow 2\,Cr^{3+} + 3\,SO_4^{2-} + 5\,H_2O \qquad (7.5)$$

However, the pH of the SRP waters usually ranges from 7.6 – 8.6 and it is not clear how effective sulfite would be for chemical reduction of Cr(VI) at these pH values.

Therefore, control tests were performed wherein sodium sulfite alone was added to the Cr(VI) solutions to better understand the chemical reduction in the pH range 8.45 – 8.85. At low SO_3^{2-}/Cr(VI), the reduction reaction was fast, but only partial Cr(VI) reduction was observed. Figure 7.6 shows the effect of increasing amounts of sodium sulfite in solutions containing 1 ppm Cr(VI). For each sulfite dose, the reduction was observed to occur within 10 minutes and the Cr(VI) concentration remained relatively constant after that. According to Equation (7.5), 1.5 moles of sulfite are required to completely reduce 1 mol of Cr(VI), which is equivalent to 2.3 ppm sulfite for 1 ppm Cr(VI). However, as shown in Figure 7.7A, 2.3 ppm sulfite was only able to reduce about 10% of the Cr(VI). Even when increasing the sulfite concentration to 9.2 ppm (4X excess), only about 40% of the Cr(VI) can be removed.

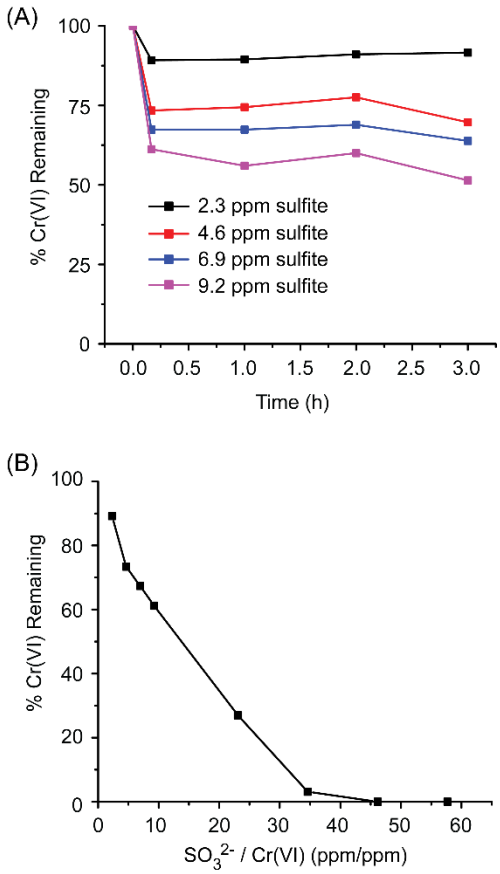

Figure 7.6 (A) Chemical reduction of 1 ppm Cr(VI) using varying amounts of 1 ppm Cr(VI) using varying amounts of Na_2SO_3, (B) Percent of Cr(VI) remaining after chemical reduction by Na_2SO_3 as a function of different sulfite to Cr(VI) ratios.

To better understand the dosage requirements needed for complete sulfite reduction of Cr(VI), a series of different SO_3^{2-}/Cr(VI) ratios (ppm/ppm) were prepared. The percentage of Cr(VI) remaining after 10 minutes was determined. As shown in Figure 7.6B, the Cr(VI) can be completely removed for SO_3^{2-}/Cr(VI) > 35 within 10 minutes. These results highlight the need for excess sulfite in order to have effective and fast chemical reduction of Cr(VI) at pH > 8.

Comparing these results to those in Figure 7.5 where SO_3^{2-}/Cr(VI) = 25, it is apparent that the presence of the photocatalyst improves the rate of Cr(VI) reduction, since this amount of sodium sulfite alone was not sufficient to remove all of the Cr(VI) in 10 minutes. Hence, use of both photocatalyst and sodium sulfite can reduce the Cr(VI) more quickly and with less sulfite required compared to use of sulfite alone as a chemical reductant. In the presence of photocatalyst, the sulfite is oxidized by the photogenerated holes rather than the Cr(VI). The standard reduction potential for the sulfate/sulfite redox reaction is E^0 = -0.936 V vs. NHE, making the potential difference (i.e. thermodynamic driving force) between sulfite and the energy of a hole in the valence band of a metal oxide semiconductor (Figure 7.1C) much larger than the potential difference between sulfite and Cr(VI). The kinetics of the sulfite oxidation with photogenerated holes may also be faster than the sulfite oxidation by Cr(VI). Thus, residual sulfite in the water matrix will be beneficial for Cr(VI) removal via photocatalytic reduction.

7.3.4 Cr(VI) Removal in Cooling Tower Blowdown

Industrial water matrices can be quite complex, making treatment more difficult than in DI water. For example, metal levels in cooling tower blowdown can be increased multiple times that found in the makeup water due to repeated cycles of concentration. Blowdown can also contain high levels of total dissolved solids (TDS) > 2000 ppm and anions such as sulfate and nitrate than can affect sorption-based treatment methods [205], as well as act as electron scavengers[196, 206, 207]. For example, average total chromium levels at the Santan Generating Station measured in Dec. 2012 – Jan. 2013 increased from 5.4 ppb in the influent makeup water to 18 ppb in the cooling tower blowdown, with most of

the total chromium in the hexavalent form due to oxidative conditions in the water treatment process [208].

The TiO_2, ZnO, and $NaTaO_3$ photocatalysts were evaluated in cooling tower blowdown water obtained from the Santan facility. The pH of the water was 8.3 and 1 ppm of Cr(VI) was added due to the low natural concentration of chromium. As shown in Figure 7.7, the Cr(VI) removal in the blowdown was very similar to that observed in DI water (Figure 7.3A,B). The apparent photocatalytic reduction rate constant k_{Cr} is also shown in the right column of Table 7.2. The slightly lower reduction velocity compared to the DI water at pH 7 is likely due to the higher concentration of competing anions and impurities in the blowdown. When using TiO_2 and ZnO, 30 minutes of irradiation was sufficient to completely remove the Cr(VI). Similar as in the pH 7 DI water, the $NaTaO_3$ displayed the slowest Cr(VI) reduction. Because sulfite-based dechlorination agents are used in excess in the facility, there may be sulfite ion residual in the blowdown water. However, the concentration of sulfite did not appear to be high enough to lead to significant improvement of the Cr(VI) removal using $NaTaO_3$ in the blowdown compared to pH 7 DI water.

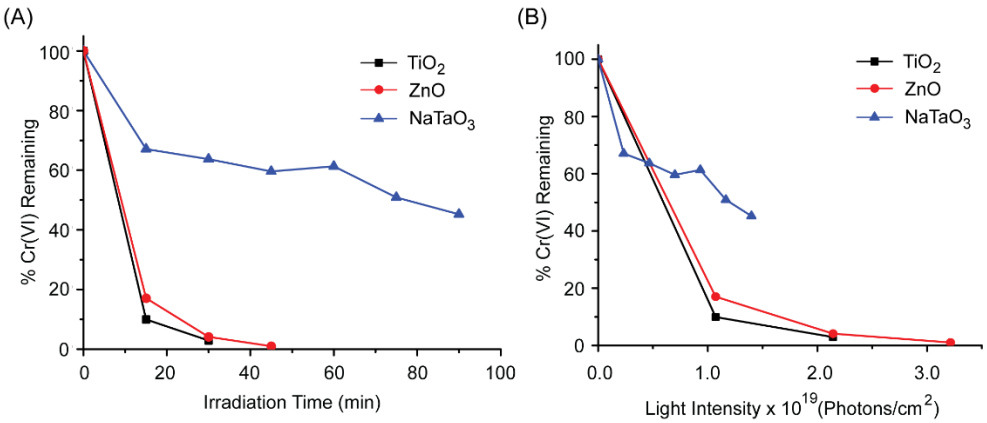

Figure 7.7 Photocatalytic reduction of 1 ppm Cr(VI) using photocatalyst at 1 g/L in cooling tower blowdown water with pH = 8.3. The percentage of Cr(VI) remaining (A) at different irradiation time and (B) usable light intensity.

7.3.5 Regeneration Experiments on Used Photocatalyst

Another important aspect to consider is the ability for the photocatalyst to be regenerated and reused after Cr(VI) removal. Trivalent chromium species can form insoluble $Cr(OH)_3$ and precipitate in solution when the pH is higher than 5.5. [209] When Cr(III) is formed via photoreduction, it can be adsorbed on the surface of the photocatalyst. [210] For an initial Cr(VI) concentration of 5 ppm, the $Cr(OH)_3$ deposited onto TiO_2 photocatalyst was distinguished by its green color.[210] In our experiments using a 10 ppm initial Cr(VI) concentration, the used photocatalysts turned green after filtration and washing, indicating that Cr(VI) was successfully reduced by the photocatalyst and removed from the system in the form of $Cr(OH)_3$.

However, the precipitated Cr(III) may inhibit further Cr(VI) reduction by occupying the reaction sites on photocatalyst and blocking the incident photons.[209] This type of

photocatalyst poisoning has been observed before, especially for large initial concentrations of Cr(VI). [210, 211] Since $Cr(OH)_3$ is an amphoteric hydroxide, it can react with either acids or bases, and thus there are different protocols in the literature for regenerating used photocatalysts[210]. Both nitric acid and sodium hydroxide were investigated as regenerating solutions for TiO_2 after it had been used to reduce 10 ppm Cr(VI). The amount of Cr(VI) removed, assuming that all species removed from solution was adsorbed onto the photocatalyst, is shown in the first column of Table 7.3.

Table 7.3 Regeneration of TiO_2 photocatalyst with acid or alkaline treatment. M_{Cr1} is the mass of Cr(VI) that was removed from the photoreduction and deposited on the surface of TiO_2 (0.2 g) after irradiation for 45 minutes in DI water at pH = 7. M_{Cr2} is the mass of Cr(III) leached in the alkaline or acid treatment.

Regeneration Condition	M_{Cr1} (mg)	M_{Cr2} (mg)
3 M NaOH	2	1.122
1 M HNO_3	2	0.346

Surprisingly the TiO_2 photocatalyst after the treatment still looked light green in color, with the acid treated TiO_2 greener than the alkaline treated one. This suggests that there was a certain amount of Cr(III) left on the surface, and that the acid treatment was less effective than the alkaline one to remove the $Cr(OH)_3$. The leachate consisting of the

regeneration solution was analyzed for Cr(VI) and Cr(III). No Cr(VI) was observed as expected, since there were no oxidizers present. The amount of Cr(III) in the leachate is shown in the second column of Table 7.3. These results show that about 44% of the Cr(III) remained adsorbed on the TiO_2 after the alkaline treatment, whereas almost 83% remained when treated with acid.

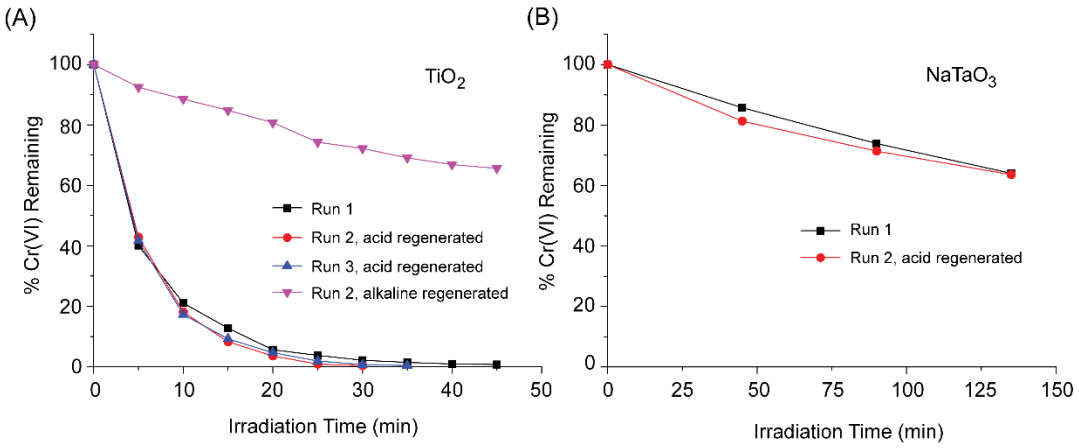

Figure 7.8 Removal of 10 ppm Cr(VI) in DI water at pH = 7 on pristine and regenerated photocatalysts (A) TiO_2, (B) $NaTaO_3$.

To examine the effect of regeneration, the acid or alkaline treated TiO_2 was used to photocatalytically reduce another DI water solution containing 10 ppm Cr(VI). These results are shown in Figure 7.8A (Run 2). Despite the presence of residual Cr(III) on the surface, the removal rate for the acid regenerated TiO_2 was similar as the Run 1 using pristine TiO_2. Since the TiO_2 has a higher surface area (92.6 m^2/g), it is possible that there are still enough reaction sites available for further Cr(VI) reduction. The TiO_2 regenerated in NaOH, however, showed poorer photoreduction rates. This difference can be explained by a change in surface properties as a result of the acid and alkaline

treatments. When TiO_2 is treated with acid, the surface becomes protonated and dichromate can more easily bind the surface, as shown in Equation (7.6): [210]

$$TiOH_2^+ + Cr_2O_7^{2-} \rightarrow TiOH\text{-}Cr_2O_7^{2-} + H^+ \quad (7.6)$$

When treated with NaOH, the surface of TiO_2 is covered with hydroxyl groups and would be neutral or negatively charged, which would prevent the surface from adsorbing chromate ions.

Based on these results, only nitric acid was used to regenerate $NaTaO_3$. The Cr(VI) removal for the first and second (e.g. regenerated) runs are shown Figure 7.8B. All of the apparent rate constants are listed in Table 7.4 for comparison. Similar to the TiO_2 case, the acid regenerated $NaTaO_3$ showed similar Cr(VI) removal properties as the pristine $NaTaO_3$. These results show that both $NaTaO_3$ and TiO_2 can be stable during regeneration and recover its performance by with acid treatment.

Table 7.4 Apparent rate constant fitted from reaction of bare and regenerated photocatalyst based on pseudo-first-order equation.

Photocatalyst	Run	k_{Cr} (min^{-1})
TiO_2	Run 1	0.1102
	Run 2, acid regenerated	0.1886
	Run 3, acid regenerated	0.1585
	Run 2, alkaline regenerated	0.0095
$NaTaO_3$	Run 1	0.0033

	Run 2, acid regenerated	0.0033

7.4 Conclusions

TiO_2, ZnO, WO_3, and $NaTaO_3$ were investigated as photocatalysts for Cr(VI) removal. All four photocatalysts were found to be effective for Cr(VI) photoreduction, but the removal rates are affected by characteristics of the material (surface area, bandgap, PZC, conduction band minimum) as well as properties of the water matrix. In DI water at pH 7, the order of removal efficiency from high to low was: TiO_2 ~ ZnO > $NaTaO_3$ > WO_3. When the pH was adjusted to 3, $NaTaO_3$ exhibited high Cr(VI) removal efficiency, and the order changed to $NaTaO_3$ > TiO_2 > WO_3 with ZnO unstable at this pH. A few common industrial additives were examined and the improvement on Cr(VI) removal using $NaTaO_3$ from high to low was: sodium sulfite > ammonium chloride > sodium formate. At neutral pH, citric acid was found to inhibit Cr(VI) reduction with $NaTaO_3$. Sulfite alone can remove Cr(VI) by chemical reduction, but required large quantities in excess. The combination of sulfite and photocatalyst greatly improved the Cr(VI) removal. Cr(VI) removal using photocatalysts was only slightly affected by other constituents in cooling tower blowdown and had similar removal rates as those observed in pH 7 DI water. Different regeneration protocols were applied to used photocatalysts. The alkaline treatment was more effective for removing adsorbed Cr(III) compared to nitric acid treatment, but acid treated TiO_2 had better subsequent Cr(VI) reduction capabilities due to surface modifications that enhanced Cr(VI) adsorption. Both acid regenerated TiO_2 and $NaTaO_3$ demonstrated comparable Cr(VI) reduction rates with the

pristine forms, indicating that these photocatalysts can be stable during regeneration and recycled for multiple uses. These results show that large scale wastewater treatment using metal oxide photocatalysts to remove Cr(VI) may be possible.

8 CONCLUSIONS OF THE DISSERTATION

In conclusion, this dissertation discusses lithium ion batteries and photocatalysts. Chapter 3 & 4 describe how to exfoliate $LiCoO_2$ and $LiNi_{1/3}Mn_{1/3}Co_{1/3}O_2$ with TEA-OH. We innovatively used electrochemical oxidation to help insert guest ions into the interlayer space of $LiCoO_2$ and $LiNi_{1/3}Mn_{1/3}Co_{1/3}O_2$ without requiring a proton exchange step, and successfully reassembled the nanosheets back into active particles. This method can be applied to other layered materials to make functional nanosheets and novel Li-ion battery materials. Besides the studies of cathode materials, we also worked on the architectures of lithium ion batteries to further improve the energy density. In Chapter 5, we have shown that paper-folding concepts can be used to optimize the structure of lithium ion battery, and compact the power of lithium ion battery. These studies on cathode materials and device architecture will help bring the breakthrough of lithium ion batteries.

Photocatalysts which will have strong oxidizing and reducing powers when shined light. With these strong oxidizing and reducing powers, photocatalysts will have wide application on waste water treatment and water splitting to generate fuels. Chapter 6 studied $AgInS_2$, an excellent light absorber with suitable band edges. Low level of Sn doping will improve the photocurrent of $AgInS_2$, but higher amounts of Sn resulted in decreased photoelectrical chemical performance. Chapter 7 studied common oxide photocatalysts and their effective usage on removal of Cr (VI) in actual industrial waste waters. These two chapters prove that semiconductor photocatalysts are promising environment-friendly materials for the energy conversion and environmental protection.

REFERENCES

1. Bouwman, P. J. in Lithium intercalation in preferentially oriented submicron $LiCoO_2$ films (Universiteit Twente, 2002).

2. Huggins, R. A. Lithium alloy anodes. Handbook of Battery Materials, 359-381 (1999).

3. Wu, Y. Lithium ion battery- Application. Chemical Engineering Press, (2004).

4. Tarascon, J. & Armand, M. Issues and challenges facing rechargeable lithium batteries. Nature 414, 359-367 (2001).

5. Sinha, S. & Murphy, D. Lithium intercalation in cubic TiS_2. Solid State Ion. 20, 81-84 (1986).

6. Reshak, A. H., Kityk, I. V. & Auluck, S. Electronic structure and optical properties of 1T-TiS_2 and lithium intercalated 1T-TiS_2 for lithium batteries. J. Chem. Phys. 129, 074706 (2008).

7. Whittingham, M. S. The role of ternary phases in cathode reactions. J. Electrochem. Soc. 123, 315-320 (1976).

8. Crowther, O. & West, A. C. Effect of electrolyte composition on lithium dendrite growth. J. Electrochem. Soc. 155, A806-A811 (2008).

9. Zhang, D., Yin, Y., Liu, C. & Fan, S. Modified secondary lithium metal batteries with the polyaniline-carbon nanotube composite buffer layer. Chem. Commun. 51, 322-325 (2015).

10. Zheng, H., Jiang, K., Abe, T. & Ogumi, Z. Electrochemical intercalation of lithium into a natural graphite anode in quaternary ammonium-based ionic liquid electrolytes. Carbon 44, 203-210 (2006).

11. Mizushima, K., Jones, P., Wiseman, P. & Goodenough, J. Li_xCoO_2 ($0<x<1$): A new cathode material for batteries of high energy density. Mater. Res. Bull. 15, 783-789 (1980).

12. Peled, E., Menachem, C., Bar-Tow, D. & Melman, A. Improved Graphite Anode for Lithium‐Ion Batteries Chemically Bonded Solid Electrolyte Interface and Nanochannel Formation. J. Electrochem. Soc. 143, L4-L7 (1996).

13. Chan, C. K. *et al*. High-performance lithium battery anodes using silicon nanowires. Nat. Nanotechnol. 3, 31-35 (2008).

14. Derrien, G., Hassoun, J., Panero, S. & Scrosati, B. Nanostructured Sn-C composite as an advanced anode material in high ‐ performance Lithium ‐ ion batteries. Adv Mater 19, 2336-2340 (2007).

15. Zheng, G. *et al*. Interconnected hollow carbon nanospheres for stable lithium metal anodes. Nat. Nanotechnol. 9, 618-623 (2014).

16. Koyama, Y., Makimura, Y., Tanaka, I., Adachi, H. & Ohzuku, T. Systematic Research on Insertion Materials Based on Superlattice Models in a Phase Triangle of $LiCoO_2$ $LiNiO_2$ $LiMnO_2$ I. First-Principles Calculation on Electronic and Crystal Structures, Phase Stability and New $LiNi_{1/2}Mn_{1/2}O_2$ Material. J. Electrochem. Soc. 151, A1499-A1506 (2004).

17. Ohzuku, T. & Ueda, A. Solid ‐ State Redox Reactions of $LiCoO_2$ ($R\bar{3}m$) for 4 Volt Secondary Lithium Cells. J. Electrochem. Soc. 141, 2972-2977 (1994).

18. Armstrong, A. R. & Bruce, P. G. Synthesis of layered $LiMnO_2$ as an electrode for rechargeable lithium batteries. Nature 381, 499-500 (1996).

19. Ohzuku, T., Ueda, A. & Nagayama, M. Electrochemistry and structural chemistry of $LiNiO_2$ ($R\bar{3}m$) for 4 volt secondary lithium cells. J. Electrochem. Soc. 140, 1862-1870 (1993).

20. Choi, J. & Manthiram, A. Role of Chemical and Structural Stabilities on the Electrochemical Properties of Layered $LiNi_{1/3}Mn_{1/3}Co_{1/3}O_2$ Cathodes. J. Electrochem. Soc. 152, A1714-A1718 (2005).

21. Kim, D. K. *et al*. Spinel $LiMn_2O_4$ nanorods as lithium ion battery cathodes. Nano Lett. 8, 3948-3952 (2008).

22. Kim, J., Myung, S., Yoon, C., Kang, S. & Sun, Y. Comparative Study of $LiNi_{0.5}Mn_{1.5}O_{4-\delta}$ and $LiNi_{0.5}Mn_{1.5}O_4$ Cathodes Having Two Crystallographic Structures: Fd3m and P4332. Chem. Mater. 16, 906-914 (2004).

23. Okada, S. *et al*. Cathode properties of phospho-olivine $LiMPO_4$ for lithium secondary batteries. J. Power Sources 97, 430-432 (2001).

24. Devaraju, M. K. & Honma, I. Hydrothermal and Solvothermal Process Towards Development of $LiMPO_4$ (M= Fe, Mn) Nanomaterials for Lithium-Ion Batteries. Adv. Energy Mater. 2, 284-297 (2012).

25. Wang, H., Jang, Y., Huang, B., Sadoway, D. R. & Chiang, Y. TEM Study of Electrochemical Cycling-Induced Damage and Disorder in $LiCoO_2$ Cathodes for Rechargeable Lithium Batteries. J. Electrochem. Soc. 146, 473-480 (1999).

26. Takahashi, Y., Kijima, N., Tokiwa, K., Watanabe, T. & Akimoto, J. Single-crystal synthesis, structure refinement and electrical properties of $Li_{0.5}CoO_2$. J. Phys. Condens. Matter 19, 436202 (2007).

27. Amatucci, G., Tarascon, J. & Klein, L. CoO_2, The End Member of the Li_xCoO_2 Solid Solution. J. Electrochem. Soc. 143, 1114-1123 (1996).

28. Amatucci, G., Tarascon, J. & Klein, L. Cobalt dissolution in $LiCoO_2$-based non-aqueous rechargeable batteries. Solid State Ion. 83, 167-173 (1996).

29. Ohzuku, T. & Ueda, A. Why transition metal (di) oxides are the most attractive materials for batteries. Solid State Ion. 69, 201-211 (1994).

30. Cho, J., Kim, Y. J. & Park, B. Novel $LiCoO_2$ cathode material with Al_2O_3 coating for a Li ion cell. Chem. Mater. 12, 3788-3791 (2000).

31. Cho, J., Kim, C. & Yoo, S. Improvement of Structural Stability of $LiCoO_2$ Cathode during Electrochemical Cycling by Sol‐Gel Coating of SnO_2. Electrochem. Solid State Lett. 3, 362-365 (2000).

32. Kim, Y. J., Cho, J., Kim, T. & Park, B. Suppression of cobalt dissolution from the $LiCoO_2$ cathodes with various metal-oxide coatings. J. Electrochem. Soc. 150, A1723-A1725 (2003).

33. Hirano, A. *et al*. Relationship between non-stoichiometry and physical properties in $LiNiO_2$. Solid State Ion. 78, 123-131 (1995).

34. Park, M. S. First-principles study of native point defects in $LiNi_{1/3}Co_{1/3}Mn_{1/3}O_2$ and Li_2MnO_3. Phys. Chem. Chem. Phys. 16, 16798-16804 (2014).

35. Hwang, B., Tsai, Y., Carlier, D. & Ceder, G. A combined computational / experimental study on $LiNi_{1/3}Co_{1/3}Mn_{1/3}O_2$. Chem. Mater. 15, 3676-3682 (2003).

36. Graetz, J., Ahn, C., Yazami, R. & Fultz, B. An electron energy-loss spectrometry study of charge compensation in $LiNi_{0.8}Co_{0.2}O_2$. J. Phys. Chem. B 107, 2887-2891 (2003).

37. Jung, S. *et al*. Understanding the degradation mechanisms of $LiNi_{0.5}Co_{0.2}Mn_{0.3}O_2$ cathode material in lithium ion batteries. Adv. Energy Mater. 4 (2014).

38. Adpakpang, K., Oh, S. M., Jin, X. & Hwang, S. A Direct Hybridization between Isocharged Nanosheets of Layered Metal Oxide and Graphene through a Surface‐Modification Assembly Process. Chem. Eur. J. 20, 15459-15466 (2014).

39. Li, J. *et al*. TiO_2 coating of $LiNi_{1/3}Co_{1/3}Mn_{1/3}O_2$ cathode materials for Li-ion batteries. Ionics 12, 215-218 (2006).

40. Sinha, N. N. & Munichandraiah, N. Synthesis and characterization of carbon-coated $LiNi_{1/3}Co_{1/3}Mn_{1/3}O_2$ in a single step by an inverse microemulsion route. ACS Appl. Mater. Interfaces 1, 1241-1249 (2009).

41. Sun, Y., Cho, S., Lee, S., Yoon, C. & Amine, K. AlF_3-coating to improve high voltage cycling performance of $LiNi_{1/3}Co_{1/3}Mn_{1/3}O_2$ cathode materials for lithium secondary batteries. J. Electrochem. Soc. 154, A168-A172 (2007).

42. Yu, H. & Zhou, H. High-energy cathode materials (Li_2MnO_3–$LiMO_2$) for lithium-ion batteries. J. Phys. Chem. Lett. 4, 1268-1280 (2013).

43. Jarvis, K. A., Deng, Z., Allard, L. F., Manthiram, A. & Ferreira, P. J. Atomic structure of a lithium-rich layered oxide material for lithium-ion batteries: evidence of a solid solution. Chem. Mater. 23, 3614-3621 (2011).

44. Strobel, P. & Lambert-Andron, B. Crystallographic and magnetic structure of Li_2MnO_3. J. Solid State Chem. 75, 90-98 (1988).

45. Armstrong, A. R. *et al.* Demonstrating oxygen loss and associated structural reorganization in the lithium battery cathode $LiNi_{0.2}Li_{0.2}Mn_{0.6}O_2$. J. Am. Chem. Soc. 128, 8694-8698 (2006).

46. Johnson, C. S., Li, N., Lefief, C., Vaughey, J. T. & Thackeray, M. M. Synthesis, Characterization and Electrochemistry of Lithium Battery Electrodes: $xLi_2MnO_3 \cdot (1\text{-}x)\ LiMn_{0.333}Ni_{0.333}Co_{0.333}O_2$ ($0 \leq x \leq 0.7$). Chem. Mater. 20, 6095-6106 (2008).

47. Zhang, X. *et al.* Structural and electrochemical study of Al_2O_3 and TiO_2 coated $Li_{1.2}Ni_{0.13}Mn_{0.54}Co_{0.13}O_2$ cathode material using ALD. Adv. Energy Mater. 3, 1299-1307 (2013).

48. Li, G., Feng, X., Ding, Y., Ye, S. & Gao, X. AlF_3-coated $Li(Li_{0.17}Ni_{0.25}Mn_{0.58})O_2$ as cathode material for Li-ion batteries. Electrochim. Acta 78, 308-315 (2012).

49. Kang, S., Johnson, C., Vaughey, J., Amine, K. & Thackeray, M. The Effects of Acid Treatment on the Electrochemical Properties of $0.5Li_2MnO_3 \cdot 0.5LiNi_{0.44}Co_{0.25}Mn_{0.31}O_2$ Electrodes in Lithium Cells. J. Electrochem. Soc. 153, A1186-A1192 (2006).

50. Abe, M. *et al.* Activation of a Li-rich Solid-Solution Layered $Li[Ni_{0.18}Li_{0.20}Co_{0.03}Mn_{0.58}]O_2$ Cathode and Retention of High Capacities via an Electrochemical Pretreatment with a Low Discharge Voltage Limit. Chem. Lett. 41, 418-419 (2012).

51. Kim, S. *et al.* Synthesis of layered–layered $0.5Li_2MnO_3 \cdot 0.5LiCoO_2$ nanocomposite electrode materials by the mechanochemical process and first principles study. J. Mater. Chem. 22, 25418-25426 (2012).

52. Mashtalir, O., Lukatskaya, M. R., Zhao, M., Barsoum, M. W. & Gogotsi, Y. Amine‐Assisted Delamination of Nb_2C MXene for Li‐Ion Energy Storage Devices. Adv. Mater. (2015).

53. Luo, J., Gao, J., Wang, A. & Huang, J. Bulk Nanostructured Materials Based on Two-Dimensional Building Blocks: A Roadmap. ACS Nano (2015).

54. Kim, T. W. *et al.* Soft‐Chemical Exfoliation Route to Layered Cobalt Oxide Monolayers and Its Application for Film Deposition and Nanoparticle Synthesis. Chem. Eur. J. 15, 10752-10761 (2009).

55. Compton, O. C. *et al.* Exfoliation and Reassembly of Cobalt Oxide Nanosheets into a Reversible Lithium‐Ion Battery Cathode. Small 8, 1110-1116 (2012).

56. Wang, L. *et al.* Fabrication and characterization of multilayer ultrathin films of exfoliated MnO_2 nanosheets and polycations. Chem. Mater. 15, 2873-2878 (2003).

57. Oh, E. *et al.* Unilamellar nanosheet of layered manganese cobalt nickel oxide and its heterolayered film with polycations. ACS Nano 4, 4437-4444 (2010).

58. Kim, J., Kim, J. & Seo, W. Exfoliation route to nanostructured cobalt oxide with enhanced thermoelectric performance. Appl. Phys. Express 4, 065201 (2011).

59. Kim, J. *et al.* Nanostructured thermoelectric cobalt oxide by exfoliation/restacking route. J. Appl. Phys. 112, 113705 (2012).

60. Song, B., Liu, Z., Lai, M. O. & Lu, L. Structural evolution and the capacity fade mechanism upon long-term cycling in Li-rich cathode material. Phys. Chem. Chem. Phys. 14, 12875-12883 (2012).

61. Nicolosi, V., Chhowalla, M., Kanatzidis, M. G., Strano, M. S. & Coleman, J. N. Liquid exfoliation of layered materials. Science 340, 1226419 (2013).

62. Zeng, Z. *et al.* Single‐Layer Semiconducting Nanosheets: High‐Yield Preparation and Device Fabrication. Angew. Chem. Int. Ed. 50, 11093-11097 (2011).

63. Sasaki, T. & Watanabe, M. Osmotic swelling to exfoliation. Exceptionally high degrees of hydration of a layered titanate. J. Am. Chem. Soc. 120, 4682-4689 (1998).

64. Sasaki, T., Watanabe, M., Hashizume, H., Yamada, H. & Nakazawa, H. Macromolecule-like aspects for a colloidal suspension of an exfoliated titanate. Pairwise association of nanosheets and dynamic reassembling process initiated from it. J. Am. Chem. Soc. 118, 8329-8335 (1996).

65. Osada, M. & Sasaki, T. Two ‐ Dimensional Dielectric Nanosheets: Novel Nanoelectronics From Nanocrystal Building Blocks. Adv. Mater. 24, 210-228 (2012).

66. Ruffo, R., Wessells, C., Huggins, R. A. & Cui, Y. Electrochemical behavior of $LiCoO_2$ as aqueous lithium-ion battery electrodes. Electrochem. Commun. 11, 247-249 (2009).

67. Amatucci, G., Tarascon, J. & Klein, L. CoO_2, the end member of the Li_xCoO_2 solid solution. J. Electrochem. Soc. 143, 1114-1123 (1996).

68. Takahashi, Y. *et al.* Structure and electron density analysis of electrochemically and chemically delithiated $LiCoO_2$ single crystals. J. Solid State Chem. 180, 313-321 (2007).

69. Lee, S. W. *et al.* The nature of lithium battery materials under oxygen evolution reaction conditions. J. Am. Chem. Soc. 134, 16959-16962 (2012).

70. Bourgeat-Lami, E., Di Renzo, F., Fajula, F., Mutin, P. H. & Des Courieres, T. Mechanism of the thermal decomposition of tetraethylammonium in zeolite. beta. J. Phys. Chem. 96, 3807-3811 (1992).

71. Choi, S. & Manthiram, A. Factors influencing the layered to spinel-like phase transition in layered oxide cathodes. J. Electrochem. Soc. 149, A1157-A1163 (2002).

72. Wang, H., Jang, Y., Huang, B., Sadoway, D. R. & Chiang, Y. TEM Study of Electrochemical Cycling ‐ Induced Damage and Disorder in $LiCoO_2$ Cathodes for Rechargeable Lithium Batteries. J. Electrochem. Soc. 146, 473-480 (1999).

73. Zou, M., Yoshio, M., Gopukumar, S. & Yamaki, J. Synthesis of high-voltage (4.5 V) cycling doped $LiCoO_2$ for use in lithium rechargeable cells. Chem. Mater. 15, 4699-4702 (2003).

74. Inaba, M., Iriyama, Y., Ogumi, Z., Todzuka, Y. & Tasaka, A. Raman study of layered rock ‐ salt $LiCoO_2$ and its electrochemical lithium deintercalation. J. Raman Spectrosc. 28, 613-617 (1997).

75. Tintignac, S., Baddour-Hadjean, R., Pereira-Ramos, J. & Salot, R. High performance sputtered $LiCoO_2$ thin films obtained at a moderate annealing treatment combined to a bias effect. Electrochim. Acta 60, 121-129 (2012).

76. Okubo, M. *et al*. Nanosize effect on high-rate Li-ion intercalation in $LiCoO_2$ electrode. J. Am. Chem. Soc. 129, 7444-7452 (2007).

77. Larcher, D., Palacin, M., Amatucci, G. & Tarascon, J. Electrochemically active $LiCoO_2$ and $LiNiO_2$ made by cationic exchange under hydrothermal conditions. J. Electrochem. Soc. 144, 408-417 (1997).

78. Akatsuka, K., Takanashi, G., Ebina, Y., Haga, M. & Sasaki, T. Electronic band structure of exfoliated titanium-and/or niobium-based oxide nanosheets probed by electrochemical and photoelectrochemical measurements. J. Phys. Chem. C 116, 12426-12433 (2012).

79. Sugimoto, W., Terabayashi, O., Murakami, Y. & Takasu, Y. Electrophoretic deposition of negatively charged tetratitanate nanosheets and transformation into preferentially oriented TiO_2 (B) film. J. Mater. Chem. 12, 3814-3818 (2002).

80. Sugimoto, W., Yokoshima, K., Ohuchi, K., Murakami, Y. & Takasu, Y. Fabrication of thin-film, flexible, and transparent electrodes composed of ruthenic acid nanosheets by electrophoretic deposition and application to electrochemical capacitors. J. Electrochem. Soc. 153, A255-A260 (2006).

81. Paulsen, J., Mueller‐Neuhaus, J. & Dahn, J. Layered $LiCoO_2$ with a different oxygen stacking (O2 structure) as a cathode material for rechargeable lithium batteries. J. Electrochem. Soc. 147, 508-516 (2000).

82. Delmas, C., Braconnier, J. & Hagenmuller, P. A new variety of $LiCoO_2$ with an unusual oxygen packing obtained by exchange reaction. Mater. Res. Bull. 17, 117-123 (1982).

83. Carlier, D. *et al*. Structural Study of the $T^{\#2}$-Li_xCoO_2 ($0.52< x\leq 0.72$) Phase. Inorg. Chem. 43, 914-922 (2004).

84. Patridge, C. J., Love, C. T., Swider-Lyons, K. E., Twigg, M. E. & Ramaker, D. E. In-situ X-ray absorption spectroscopy analysis of capacity fade in nanoscale-$LiCoO_2$. J. Solid State Chem. 203, 134-144 (2013).

85. Jung, Y. S. *et al*. Enhanced stability of LiCoO2 cathodes in lithium-ion batteries using surface modification by atomic layer deposition. J. Electrochem. Soc. 157, A75-A81 (2010).

86. Kim, T. W., Jung, T. S., Hyun, S. & Hwang, S. Mesoporous assembly of 2D manganate nanosheets intercalated with cobalt ions. Mater. Lett. 64, 565-568 (2010).

87. Zheng, H., Li, J., Song, X., Liu, G. & Battaglia, V. S. A comprehensive understanding of electrode thickness effects on the electrochemical performances of Li-ion battery cathodes. Electrochim. Acta 71, 258-265 (2012).

88. Hu, L. & Cui, Y. Energy and environmental nanotechnology in conductive paper and textiles. Energy Environ. Sci. 5, 6423-6435 (2012).

89. Huang, J. *et al.* Highly transparent and flexible nanopaper transistors. Acs Nano 7, 2106-2113 (2013).

90. Dragoman, M., Flahaut, E., Dragoman, D., Al Ahmad, M. & Plana, R. Writing simple RF electronic devices on paper with carbon nanotube ink. Nanotechnol. 20, 375203 (2009).

91. Liu, H. & Crooks, R. M. Paper-based electrochemical sensing platform with integral battery and electrochromic read-out. Anal. Chem. 84, 2528-2532 (2012).

92. Lankelma, J., Nie, Z., Carrilho, E. & Whitesides, G. M. Paper-based analytical device for electrochemical flow-injection analysis of glucose in urine. Anal. Chem. 84, 4147-4152 (2012).

93. Liu, H. & Crooks, R. M. Three-dimensional paper microfluidic devices assembled using the principles of origami. J. Am. Chem. Soc. 133, 17564-17566 (2011).

94. Dungchai, W., Chailapakul, O. & Henry, C. S. Electrochemical detection for paper-based microfluidics. Anal. Chem. 81, 5821-5826 (2009).

95. Martinez, A. W., Phillips, S. T., Whitesides, G. M. & Carrilho, E. Diagnostics for the developing world: microfluidic paper-based analytical devices. Anal. Chem. 82, 3-10 (2009).

96. Siegel, A. C., Phillips, S. T., Wiley, B. J. & Whitesides, G. M. Thin, lightweight, foldable thermochromic displays on paper. Lab Chip 9, 2775-2781 (2009).

97. Hu, L. *et al.* Transparent and conductive paper from nanocellulose fibers. Energy Environ. Sci. 6, 513-518 (2013).

98. Russo, A. *et al.* Pen‐on‐Paper Flexible Electronics. Adv. Mater. 23, 3426-3430 (2011).

99. Yuan, L. *et al.* Polypyrrole-coated paper for flexible solid-state energy storage. Energy Environ. Sci. 6, 470-476 (2013).

100. Olsson, H. *et al.* Influence of the cellulose substrate on the electrochemical properties of paper-based polypyrrole electrode materials. J. Mater. Sci. 47, 5317-5325 (2012).

101. Gui, Z. *et al.* Natural cellulose fiber as substrate for supercapacitor. ACS Nano 7, 6037-6046 (2013).

102. Kang, Y. J. *et al.* All-solid-state flexible supercapacitors fabricated with bacterial nanocellulose papers, carbon nanotubes, and triblock-copolymer ion gels. ACS Nano 6, 6400-6406 (2012).

103. Zhong, Q. *et al.* A paper-based nanogenerator as a power source and active sensor. Energy Environ. Sci. 6, 1779-1784 (2013).

104. Fan, K., Peng, T., Chen, J., Zhang, X. & Li, R. Low-cost, quasi-solid-state and TCO-free highly bendable dye-sensitized cells on paper substrate. J. Mater. Chem. 22, 16121-16126 (2012).

105. Zhang, L. *et al*. Small-size biofuel cell on paper. Biosensors and Bioelectronics 35, 155-159 (2012).

106. Xie, X. *et al.* Nano-structured textiles as high-performance aqueous cathodes for microbial fuel cells. Energy Environ. Sci. 4, 1293-1297 (2011).

107. Gardner, J. P. *et al.* The james webb space telescope. Space Sci. Rev. 123, 485-606 (2006).

108. Liu, H., Xiang, Y., Lu, Y. & Crooks, R. M. Aptamer‐based origami paper analytical device for electrochemical detection of adenosine. Angew. Chem. Int. Ed. 124, 7031-7034 (2012).

109. Ahn, B. Y. *et al.* Printed origami structures. Adv. Mater. 22, 2251-2254 (2010).

110. Wei, Z. Y., Guo, Z. V., Dudte, L., Liang, H. Y. & Mahadevan, L. Geometric mechanics of periodic pleated origami. Phys. Rev. Lett. 110, 215501 (2013).

111. An, B., Benbernou, N., Demaine, E. D. & Rus, D. Planning to fold multiple objects from a single self-folding sheet. Robotica 29, 87-102 (2011).

112. Wang, C. *et al.* Printed Carbon Nanotubes on Polymer Films for Active Origami. Mater. Res. Lett. 1, 13-18 (2013).

113. Miura, K. Map fold a la miura style, its physical characteristics and application to the space science. Research of Pattern Formation, 77-90 (1994).

114. Nishiyama, Y. Miura folding: Applying origami to space exploration. Int. J. Pure Appl. Math. 79, 269-279 (2012).

115. Hu, L. *et al.* Highly conductive paper for energy-storage devices. Proc. Natl. Acad. Sci. 106, 21490-21494 (2009).

116. John, J., Li, Y., Zhang, J., Loeb, J. A. & Xu, Y. Microfabrication of 3D neural probes with combined electrical and chemical interfaces. J. Micromech. Microengineering 21, 105011 (2011).

117. Kim, E. *et al.* A robust polymer microcable structure for flexible devices. Appl. Phys. Lett. 102, 033506 (2013).

118. Katragadda, R. B. & Xu, Y. A novel intelligent textile technology based on silicon flexible skins. Sensor. Actuators A-Phys. 143, 169-174 (2008).

119. Demaine, E. D. & O'Rourke, J. A survey of folding and unfolding in computational geometry. Combinatorial and computational geometry 52, 167-211 (2005).

120. Balkcom, D. J. & Mason, M. T. Robotic origami folding. Int. J. Robot. Res. 27, 613-627 (2008).

121. Fujishima, A. Electrochemical photolysis of water at a semiconductor electrode. Nature 238, 37-38 (1972).

122. Chen, D. & Ye, J. Hierarchical WO_3 hollow shells: dendrite, sphere, dumbbell, and their photocatalytic properties. Adv. Funct. Mater. 18, 1922-1928 (2008).

123. Georgekutty, R., Seery, M. K. & Pillai, S. C. A highly efficient Ag-ZnO photocatalyst: synthesis, properties, and mechanism. J. Phys. Chem. C 112, 13563-13570 (2008).

124. Kleiman-Shwarsctein, A., Hu, Y., Forman, A. J., Stucky, G. D. & McFarland, E. W. Electrodeposition of α-Fe_2O_3 doped with Mo or Cr as photoanodes for photocatalytic water splitting. J. Phys. Chem. C 112, 15900-15907 (2008).

125. Kato, H., Asakura, K. & Kudo, A. Highly efficient water splitting into H_2 and O_2 over lanthanum-doped $NaTaO_3$ photocatalysts with high crystallinity and surface nanostructure. J. Am. Chem. Soc. 125, 3082-3089 (2003).

126. Maeda, K. *et al.* GaN: ZnO solid solution as a photocatalyst for visible-light-driven overall water splitting. J. Am. Chem. Soc. 127, 8286-8287 (2005).

127. Walter, M. G. *et al.* Solar water splitting cells. Chem. Rev. 110, 6446-6473 (2010).

128. Maeda, K. & Domen, K. Surface nanostructures in photocatalysts for visible-light-driven water splitting. Photocatalysis, 95-119 (2011).

129. Grätzel, M. Photoelectrochemical cells. Nature 414, 338-344 (2001).

130. Kudo, A. Photocatalysis and solar hydrogen production. Pure Appl. Chem. 79, 1917-1927 (2007).

131. Kudo, A. Development of photocatalyst materials for water splitting. Int. J. Hydrogen Energy 31, 197-202 (2006).

132. Minggu, L. J., Daud, W. R. W. & Kassim, M. B. An overview of photocells and photoreactors for photoelectrochemical water splitting. Int. J. Hydrogen Energy 35, 5233-5244 (2010).

133. Maruthamuthu, P. & Ashokkumar, M. Hydrogen generation using Cu (II)/WO3 and oxalic acid by visible light. Int. J. Hydrogen Energy 13, 677-680 (1988).

134. Asahi, R., Morikawa, T., Ohwaki, T., Aoki, K. & Taga, Y. Visible-light photocatalysis in nitrogen-doped titanium oxides. Science 293, 269-271 (2001).

135. Cesar, I., Kay, A., Martinez, J. A. G. & Grätzel, M. Translucent thin film Fe_2O_3 photoanodes for efficient water splitting by sunlight: nanostructure-directing effect of Si-doping. J. Am. Chem. Soc. 128, 4582-4583 (2006).

136. Chen, X., Liu, L., Yu, P. Y. & Mao, S. S. Increasing solar absorption for photocatalysis with black hydrogenated titanium dioxide nanocrystals. Science 331, 746 (2011).

137. Repins, I. *et al.* 19.9% ‐ efficient ZnO/CdS/$CuInGaSe_2$ solar cell with 81.2% fill factor. Prog. Photovoltaics Res. Appl. 16, 235-239 (2008).

138. Jackson, P. *et al.* New world record efficiency for Cu(In, Ga)Se_2 thin ‐ film solar cells beyond 20%. Prog. Photovoltaics Res. Appl. 19, 894-897 (2011).

139. Siebentritt, S. Shallow Defects in the Wide Gap Chalcopyrite $CuGaSe_2$. Wide-gap chalcopyrites, 113-156 (2006).

140. Tsuji, I., Kato, H. & Kudo, A. Photocatalytic hydrogen evolution on ZnS-$CuInS_2$-$AgInS_2$ solid solution photocatalysts with wide visible light absorption bands. Chemistry of materials 18, 1969-1975 (2006).

141. Tsuji, I., Kato, H., Kobayashi, H. & Kudo, A. Photocatalytic H_2 Evolution Reaction from Aqueous Solutions over Band Structure-Controlled $(AgIn)_xZn_{2(1-x)}S_2$ Solid Solution

Photocatalysts with Visible-Light Response and Their Surface Nanostructures. J. Am. Chem. Soc. 126, 13406-13413 (2004).

142. Tsuji, I., Kato, H., Kobayashi, H. & Kudo, A. Photocatalytic H2 Evolution under Visible-Light Irradiation over Band-Structure-Controlled $(CuIn)_xZn_{2(1-x)}S_2$ Solid Solutions. J. Phys. Chem. B 109, 7323-7329 (2005).

143. Jang, J. J. S. Indium induced band gap tailoring in $AgGa_{1-x}In_xS_2$ chalcopyrite structure for visible light photocatalysis. J. Chem. Phys. 128, 154717 (2008).

144. Djellal, L., Bouguelia, A., Kadi Hanifi, M. & Trari, M. Bulk p-$CuInSe_2$ photo-electrochemical solar cells. Solar Energy Mater. Solar Cells 92, 594-600 (2008).

145. Ye, H. *et al.* Photoelectrochemical Characterization of $CuInSe_2$ and $Cu(In_{1-x}Ga_x)Se_2$ Thin Films for Solar Cells. J. Phys. Chem. C (2011).

146. Kaneshiro, J., Gaillard, N., Rocheleau, R. & Miller, E. Advances in copper-chalcopyrite thin films for solar energy conversion. Solar Energy Mater. Solar Cells 94, 12-16 (2010).

147. Riha, S. C. *et al.* Photoelectrochemical Characterization of Nanocrystalline Thin-Film Cu_2ZnSnS_4 Photocathodes. ACS Appl. Mater. Interface (2011).

148. Ma, G., Minegishi, T., Yokoyama, D., Kubota, J. & Domen, K. Photoelectrochemical hydrogen production on Cu_2ZnSnS_4/Mo-mesh thin-film electrodes prepared by electroplating. Chem. Phys. Lett. 501, 619-622 (2011).

149. Marsen, B., Cole, B. & Miller, E. L. Photoelectrolysis of water using thin copper gallium diselenide electrodes. Solar Energy Mater. Solar Cells 92, 1054-1058 (2008).

150. Bolton, J. R., Strickler, S. J. & Connolly, J. S. Limiting and realizable efficiencies of solar photolysis of water. Nature 316, 495-500 (1985).

151. Tell, B. B. Room-Temperature Electrical Properties of Ten I-III-VI_2 Semiconductors. J. Appl. Phys. 43, 2469 (1972).

152. Masse, G. & Redjai, E. S ‑ vacancy energy levels in $AgInS_2$. J. Appl. Phys. 59, 1544-1547 (1986).

153. Akaki, Y. *et al.* Structural, electrical and optical properties of $AgInS_2$ thin films grown by thermal evaporation method. J. Phys. Chem. Solids 66, 1858-1861 (2005).

154. Walter, M. G. *et al.* Solar water splitting cells. Chem. Rev. 110, 6446 (2010).

155. Bard, A. A. J. Thermodynamic Potential for the Anodic Dissolution of n-Type Semiconductors. J. Electrochem. Soc. 124, 1706 (1977).

156. Gerischer, H. On the stability of semiconductor electrodes against photodecomposition. J Electroanalytical Chem. Interfacial Electrochem. 82, 133-143 (1977).

157. Chen, Y. W. *et al.* Atomic layer-deposited tunnel oxide stabilizes silicon photoanodes for water oxidation. Nature Mater. 10, 539-544 (2011).

158. Hwang, Y. J., Boukai, A. & Yang, P. High density n-Si/n-TiO_2 core/shell nanowire arrays with enhanced photoactivity. Nano Lett. 9, 410-415 (2008).

159. Wang, C. H., Cheng, K. W. & Tseng, C. J. Photoelectrochemical properties of $AgInS_2$ thin films prepared using electrodeposition. Solar Energy Mater. Solar Cells 95, 453-461 (2011).

160. Cheng, K. W. & Liu, P. H. Photoelectrochemical performances of $AgInS_2$ film electrodes fabricated using the sulfurization of Ag-In metal precursors. Solar Energy Mater. Solar Cells (2011).

161. Hong, K. *et al.* Photocurrent study of the valence band splitting of $AgInS_2$ epilayers on GaAs. J. Phys. Chem. Solids 64, 1119-1124 (2003).

162. Ortega-López, M., Morales-Acevedo, A. & Solorza-Feria, O. Physical properties of $AgInS_2$ films prepared by chemical spray pyrolysis. Thin Solid Films 385, 120-125 (2001).

163. Arredondo, C., Clavijo, J., Aristizabal, A. & Gordillo, G. Investigation of $AgInSe_2$ thin films grown by co-evaporation (Photovoltaic Specialists Conference (PVSC), 2009 34th IEEE, IEEE, 2009).

164. Scheer, R. *et al.* Incorporation of the doping elements Sn, N, and P in $CuInS_2$ thin films prepared by co-evaporation. Thin Solid Films 392, 1-10 (2001).

165. Ben Rabeh, M., Zribi, M., Kanzari, M. & Rezig, B. Structural and optical characterization of Sn incorporation in $CuInS_2$ thin films grown by vacuum evaporation method. Mater. Lett. 59, 3164-3168 (2005).

166. Albor-Aguilera, M., Ramírez-Rosales, D. & González-Trujillo, M. Change from n-type to p-type conductivity on $AgInS_2$ and $AgInS_2$: Sn polycrystalline thin films prepared by spray pyrolysis technique. Thin Solid Films 517, 2535-2537 (2009).

167. Tseng, C. J., Wang, C. H. & Cheng, K. W. Photoelectrochemical performance of gallium-doped $AgInS_2$ photoelectrodes prepared by electrodeposition process. Solar Energy Mater. Solar Cells 96, 33-42 (2012).

168. Shay, J., Tell, B., Schiavone, L., Kasper, H. & Thiel, F. Energy bands of $AgInS_2$ in the chalcopyrite and orthorhombic structures. Phys. Rev. B 9, 1719 (1974).

169. Chen, Z. *et al*. Accelerating materials development for photoelectrochemical hydrogen production: Standards for methods, definitions, and reporting protocols. J. Mater. Res. 25, 3-16 (2010).

170. Hattori, K., Akamatsu, K. & Kamegashira, N. Electrical properties of polycrystalline chalcopyrite $AgInS_2$ films. J. Appl. Phys. 71, 3414-3418 (1992).

171. Albor-Aguilera, M., Cayente-Romero, J., Peza-Tapia, J., De León-Gutiérrez, L. & Ortega-López, M. Optical and electrical properties of p-type $AgInSn_xS_{2-x}$(x=0-0.04) thin films prepared by spray pyrolysis. Thin Solid Films 490, 168-172 (2005).

172. Mohan, D. & Pittman Jr, C. U. Activated carbons and low cost adsorbents for remediation of tri-and hexavalent chromium from water. J. Hazard. Mater. 137, 762-811 (2006).

173. Testa, J. J., Grela, M. A. & Litter, M. I. Heterogeneous photocatalytic reduction of chromium (VI) over TiO_2 particles in the presence of oxalate: involvement of Cr(V) species. Environ. Sci. Technol. 38, 1589-1594 (2004).

174. Katz, S. A. & Salem, H. The toxicology of chromium with respect to its chemical speciation: a review. J. Appl. Toxicol. 13, 217-224 (1993).

175. Barrera-Díaz, C. E., Lugo-Lugo, V. & Bilyeu, B. A review of chemical, electrochemical and biological methods for aqueous Cr (VI) reduction. J. Hazard. Mater. 223, 1-12 (2012).

176. Lindsay, D. R., Farley, K. J. & Carbonaro, R. F. Oxidation of Cr III to Cr VI during chlorination of drinking water. J. Environ. Monitor. 14, 1789-1797 (2012).

177. Kosmulski, M. The pH-dependent surface charging and the points of zero charge. J. Colloid Interface Sci. 253, 77-87 (2002).

178. Izadifard, M., Achari, G. & Langford, C. H. Application of photocatalysts and LED light sources in drinking water treatment. Catalysts 3, 726-743 (2013).

179. Kudo, A. & Miseki, Y. Heterogeneous photocatalyst materials for water splitting. Chem. Soc. Rev. 38, 253-278 (2009).

180. Weber, M. F. & Dignam, M. J. Efficiency of splitting water with semiconducting photoelectrodes. J. Electrochem. Soc. 131, 1258-1265 (1984).

181. Lin, W., Wei, C. & Rajeshwar, K. Photocatalytic reduction and immobilization of hexavalent chromium at titanium dioxide in aqueous basic media. J. Electrochem. Soc. 140, 2477-2482 (1993).

182. Xu, Y. & Schoonen, M. A. The absolute energy positions of conduction and valence bands of selected semiconducting minerals. Am. Mineral. 85, 543-556 (2000).

183. Litter, M. I. Treatment of chromium, mercury, lead, uranium, and arsenic in water by heterogeneous photocatalysis. Adv. Chem. Eng. 36, 37-67 (2009).

184. Farmer, J. C. *et al.* Electrosorption of chromium ions on carbon aerogel electrodes as a means of remediating ground water. Energy Fuels, 337-347 (1997).

185. Fujishima, A. & Honda, K. Photolysis-decomposition of water at the surface of an irradiated semiconductor. Nature 238, 37-38 (1972).

186. Wang, Q., Shang, J., Zhu, T. & Zhao, F. Efficient photoelectrocatalytic reduction of Cr (VI) using TiO_2 nanotube arrays as the photoanode and a large-area titanium mesh as the photocathode. J. Mol. Catal. A: Chem. 335, 242-247 (2011).

187. Yoneyama, H., Yamashita, Y. & Tamura, H. Heterogeneous photocatalytic reduction of dichromate on n-type semiconductor catalysts. Nature 282, 817-818 (1979).

188. Doménech, J. & Muñoz, J. Photocatalytical reduction of Cr (VI) over ZnO powder. Electrochim. Acta 32, 1383-1386 (1987).

189. Kato, H., Asakura, K. & Kudo, A. Highly efficient water splitting into H_2 and O_2 over lanthanum-doped $NaTaO_3$ photocatalysts with high crystallinity and surface nanostructure. J. Am. Chem. Soc. 125, 3082-3089 (2003).

190. Tüysüz, H. & Chan, C. K. Preparation of amorphous and nanocrystalline sodium tantalum oxide photocatalysts with porous matrix structure for overall water splitting. Nano Energy 2, 116-123 (2013).

191. Kosmulski, M. pH-dependent surface charging and points of zero charge: III. Update. J. Colloid Interface Sci. 298, 730-741 (2006).

192. Parks, G. A. & Bruyn, P. D. The Zero Point of Charge of Oxides1. J. Phys. Chem. 66, 967-973 (1962).

193. Yoon, R. H., Salman, T. & Donnay, G. Predicting points of zero charge of oxides and hydroxides. J. Colloid Interface Sci. 70, 483-493 (1979).

194. Deng, Y., Chen, Y., Chen, B. & Ma, J. Preparation, characterization and photocatalytic activity of $CuBi_2O_4/NaTaO_3$ coupled photocatalysts. J. Alloys Compounds 559, 116-122 (2013).

195. Li, X. & Zang, J. Facile hydrothermal synthesis of sodium tantalate ($NaTaO_3$) nanocubes and high photocatalytic properties. J. Phys. Chem. C 113, 19411-19418 (2009).

196. Doudrick, K., Monzón, O., Mangonon, A., Hristovski, K. & Westerhoff, P. Nitrate reduction in water using commercial titanium dioxide photocatalysts (P25, P90, and Hombikat UV100). J. Environ. Eng. 138, 852-861 (2011).

197. Manassero, A., Satuf, M. L. & Alfano, O. M. Evaluation of UV and visible light activity of TiO_2 catalysts for water remediation. Chem. Eng. J. 225, 378-386 (2013).

198. Seitz, L. C. *et al.* Modeling Practical Performance Limits of Photoelectrochemical Water Splitting Based on the Current State of Materials Research. ChemSusChem 7, 1372-1385 (2014).

199. Rocheleau, R. E. & Miller, E. L. Photoelectrochemical production of hydrogen: Engineering loss analysis. Int. J. Hydrogen Energy 22, 771-782 (1997).

200. Shockley, W. & Queisser, H. J. Detailed balance limit of efficiency of p-n junction solar cells. J. Appl. Phys. 32, 510-519 (1961).

201. Daneshvar, N., Salari, D. & Aber, S. Chromium adsorption and Cr (VI) reduction to trivalent chromium in aqueous solutions by soya cake. J. Hazard. Mater. 94, 49-61 (2002).

202. Chenthamarakshan, C., Rajeshwar, K. & Wolfrum, E. J. Heterogeneous photocatalytic reduction of Cr (VI) in UV-irradiated titania suspensions: effect of protons, ammonium ions, and other interfacial aspects. Langmuir 16, 2715-2721 (2000).

203. Hartani, K. & Khan, Z. Unusual rate inhibition of manganese (II) assisted oxidation of citric acid by chromium (VI) in the presence of ionic micelles. Trans. Metal Chem. 25, 478-484 (2000).

204. Beukes, J., Pienaar, J., Lachmann, G. & Giesekke, E. The reduction of hexavalent chromium by sulphite in wastewater. Water S. A. 25, 363-370 (1999).

205. Kaliappan, S., Sathish, C. & Nirmalkumar, T. Recovery and reuse of water from effluents of cooling tower. J. Indian Institute Sci. 85, 215 (2013).

206. Yang, T., Doudrick, K. & Westerhoff, P. Photocatalytic reduction of nitrate using titanium dioxide for regeneration of ion exchange brine. Water Res. 47, 1299-1307 (2013).

207. Doudrick, K., Yang, T., Hristovski, K. & Westerhoff, P. Photocatalytic nitrate reduction in water: Managing the hole scavenger and reaction by-product selectivity. Appl. Catal. B: Environ. 136, 40-47 (2013).

208. Bowen, A. Occurrence and Treatment of Hexavalent Chromium and Arsenic in Arizona Municipal and Industrial Waters (2014).

209. Navío, J. A. *et al.* Heterogeneous photocatalytic reactions of nitrite oxidation and Cr (VI) reduction on iron-doped titania prepared by the wet impregnation method. Appl. Catal. B. 16, 187-196 (1998).

210. Tuprakay, S. & Liengcharernsit, W. Lifetime and regeneration of immobilized titania for photocatalytic removal of aqueous hexavalent chromium. J. Hazard. Mater. 124, 53-58 (2005).

211. Liu, W., Ni, J. & Yin, X. Synergy of photocatalysis and adsorption for simultaneous removal of Cr (VI) and Cr (III) with TiO_2 and titanate nanotubes. Water Res. 53, 12-25 (2014).

APPENDIX-A

STATEMENT OF COAUTHORS' PERMISSIONS

I, Qian Cheng, committed that all co-authors have granted their permissions for the usage of following publications in this dissertation:

(1) Cheng, Q., Yang, T., Li, Y., Li, M., Chan, C. K. Oxidation–reduction assisted exfoliation of $LiCoO_2$ into nanosheets and reassembly into functional Li-ion battery cathodes, J. Mater. Chem. A 4, 6902-6910 (2016).

(2) Cheng. Q, Song, Z., Ma, T., *et al.* Folding paper-based lithium-ion batteries for higher areal energy densities, Nano Letters. 13, 4969-4974 (2013).

(3) Cheng, Q., Peng, X., Chan, C. K. Structural and photoelectrochemical evaluation of nanotextured Sn-Doped $AgInS_2$ films prepared by spray pyrolysis, ChemSusChem. 6 102-109 (2013).

(4) Cheng, Q., Wang, C., Doudrick, K., Chan, C. K. Hexavalent chromium removal using metal oxide photocatalysts, Appl. Catal., B 176, 740-748 (2015).